

©Copyright 2022
Erica E. Eggleton

Multiscale Data, Analytics, and Tools for Transportation Electrification

Erica E. Eggleton

A dissertation
submitted in partial fulfillment of the
requirements for the degree of

Doctor of Philosophy

University of Washington

2022

Reading Committee:

Daniel T. Schwartz, Chair

David A. C. Beck

Stuart B. Adler

Jessica Kaminsky

Program Authorized to Offer Degree:

Chemical Engineering

University of Washington

Abstract

Multiscale Data, Analytics, and Tools for Transportation Electrification

Erica E. Eggleton

Chair of the Supervisory Committee:

Daniel T. Schwartz

Department of Chemical Engineering

The demand for electrified transportation, including battery-electric buses, is increasing as fleets aim to meet lower carbon emissions goals. However, there exist knowledge gaps, which include but are not limited to charging infrastructure placement and demand, battery sizing for optimal vehicle range, and the effect of load demands on battery lifetime and performance, that impede the adoption of these technologies at the desired rate. Solving these problems requires information and models across scales, from the vehicle systems to the battery packs, cells, and materials. This work creates tools, data analysis, and datasets across these scales.

First, a vehicle dynamics model is used to estimate the power and energy required to transport a battery-electric bus across a given route, using King County Metro bus routes as a case-study. The load demand for the Battery Energy Storage System (BESS) on-board is estimated, and routes are compared based on load profiles and distributions. The effect of route characteristics such as elevation, frequency of stops, and ridership mass on the battery load are also analyzed. Select load profiles are then translated to the cell-level and used as charging protocols for commercial Li-ion cells. The resulting voltage and current profiles allow us to calibrate a simple battery model that can estimate these profiles for other routes.

Lastly, we emphasize the importance of data sharing to improve battery models. We introduce the framework for a standardized data-sharing protocol with suggested metadata. An example dataset utilizes the proposed format and demonstrates the importance of replicates in open dataset.

Table of Contents

List of Figures	iii
List of Tables.....	vii
Acknowledgements.....	viii
Dedication.....	x
<i>Chapter 1 - Introduction</i>	<i>1</i>
1.1 Motivation	1
1.2 Energy Storage	2
1.3 Multiscale Models	3
1.3.1 Vehicle Dynamics Models	3
1.3.2 Battery Models.....	3
1.3.3 Degradation Models.....	4
1.4 Open-Source Software and Data	4
1.5 Dissertation Roadmap	5
<i>Chapter 2 - Route_Dynamics: an Open-Source Python Package for Determining Energy Requirements and Battery Fatigue for Electric Bus Fleets</i>	<i>7</i>
2.1 Introduction	8
2.2 Methodology	9
2.2.1 Vehicle Dynamics Model.....	9
2.2.2 Software.....	14
2.3 Results and Discussion	18
2.4 Conclusions and Proposed Future Work	24
2.5 Appendix – Full Results	25
<i>Chapter 3 - Multi-scale Integration of Computed Battery Electric Bus Fleet Drive Cycles with Cell Testing and State Estimation from Simple Battery Management Models</i>	<i>30</i>
3.1 Introduction	30
3.2 Methodology	31
3.2.1 Cell-Level Drive Cycles	32
3.2.2 Cycling and EIS Measurement Protocols	33
3.2.3 Cell-Level Model	34
3.3 Results and Discussion	36
Checking Resistance Estimation with EIS	43
3.4 Conclusions	44
3.5 Appendix	45

Chapter 4 - Establishing a Framework for an Open-Source Battery Database.....	49
4.2 Example Dataset	51
4.2.1 Methods	51
4.2.2 Cycling Test Results.....	53
4.3 Metadata.....	63
4.4 Schema.....	66
4.5 Conclusions	67
Chapter 5 - Additional Projects	68
5.1 Motivation	68
5.2 User-Friendly Jupyter Notebooks for Process Design and Modeling	69
5.2.1 Methodology.....	69
5.2.2 Notebook Format.....	70
5.3 Solid Oxide Fuel Cell Modeling and Parameter Estimations.....	72
Chapter 6 - Conclusions and Future Work.....	73
6.1 Summary	73
6.2 Future Work	73
6.2.1 Systems-Level and Vehicle Dynamics	73
6.2.2 Module-Level	74
6.2.3 Cell-Level Modeling	74
Bibliography.....	75
Curriculum Vitae	81

List of Figures

Figure 1.1: Relating vehicle and cell experiences to degradative results.	4
Figure 2.1 Forces acting on vehicle and included in the longitudinal vehicle dynamics model	9
Figure 2.2: Drivetrain layout assumed for this case study	11
Figure 2.3: Logic flow of the route_dynamics package. Green boxes are data inputs, and yellow boxes are package modules.....	14
Figure 2.4: a) Zoomed in view of Route 22. Route events such as bus stops and traffic lights have been overlaid. b) Route ridership for Route 22 inbound. c) The shapefile for Route 22 overlaid on the DSM layer for King County	15
Figure 2.5: The conversion of the time-series acceleration data to spatial. (a) The given start-from-stop acceleration profile. (b) The resulting speed vs. distance profile. (c) The resulting load profile for the start-from-stop profile, assuming 0% road grade.	17
Figure 2.6: An example drive cycle for a section of a route with two bus stops and a speed limit of 25 miles per hour.	17
Figure 2.7: (a) Load profile with elevation for route 186. 9b0 Load distribution for route 186. (c) Load profile with elevation for route 22. (d) Load distribution for route 22.....	19
Figure 2.8: (top) Force break-down profile for route 186. (bottom) Force break-down profile for route 22.	20
Figure 3.1: Example of a voltage histogram from a New-Flyer hybrid-electric bus battery management system	31
Figure 3.2: (top) Cell-level drive-cycle for route 22. (bottom) Cell-level drive cycle for route 186.....	33
Figure 3.3: Diagram for equivalent-circuit representation for the simplified battery model, where a resistor is in series with a SOC-dependent voltage source.	34
Figure 3.4: The measured current profile (a), measured voltage profile with open-circuit voltage estimates, and (c) resistance estimates for Cell 13, a fresh, high-SOC cell on a high extreme route	37
Figure 3.5: Parity plot for Cell 13, comparing the measured and modeled voltage values.	37
Figure 3.6: The measured current profile (a), measured voltage profile with open-circuit voltage estimates, and (c) resistance estimates for Cell 20, an aged, low-SOC cell on a high extreme route	38

Figure 3.7: Parity plot for Cell 20, comparing the measured and modeled voltage values.	39
Figure 3.8: The measured current profile (a), measured voltage profile with open-circuit voltage estimates, and (c) resistance estimates for Cell 16, a fresh, low-SOC cell on a high extreme route	39
Figure 3.9: Parity plot for Cell 16, comparing the measured and modeled voltage values.	40
Figure 3.10: Comparison of current profile for a six minute segment of first and second trip for Cell 16.	40
Figure 3.11: Voltage and current profile estimated for route 101, using the values for open-circuit voltage and resistance calibrated from Cell 13.	42
Figure 3.12: Voltage distribution for route 101, using the conditions from Cell 13.	42
Figure 3.13: Nyquist plot for Cell 15 with a fit found using impedance.py.	43
Figure 3.14: Measured voltage a current profiles for Cell 15, a fresh, low-SOC cell on a high-extreme route.	45
Figure 3.15: Parity plot for Cell 15, comparing measured and modeled voltage value	45
Figure 3.16: Experimentally measured voltage and current profiles for Cell 17, an aged, high-SOC cell on an high-extreme route.....	46
Figure 3.17: Parity plot for Cell 17, comparing measured and modeled voltage values.....	46
Figure 3.18: Experimentally measured voltage and current profiles for Cell 18, an aged, high-SOC cell on a low-extreme route.....	47
Figure 3.19: Parity plot for Cell 18, comparing modeled and measured voltage values.....	47
Figure 3.20: Experimentally measured voltage and current profiles for Cell 19, an aged, low-SOC cell with a high-extreme route.....	48
Figure 3.21: Parity plot for cell 19, comparing modeled and measured voltage values.....	48
Figure 4.1: Capacity with cycles plot for all cycled cells under the four different experimental conditions Case 1: 2.67C, 25oC, Case 2: 2C, 25oC, Case 3: 2.67C, 5oC, and Case 4: 2C, 5oC. Shaded areas represent two standard deviations. For each condition, cells were cycled to either 300, 600, 900, or 1500 cycles, as noted by the dashed lines	54
Figure 4.2: Mean values of (a) charge and (b) discharge voltage with SOC at cycle 500 for a replicate group of cells cycled under the 2.67C, 25oC condition. This replicate group consists of 8 cells and the shaded area represents two standard deviations.....	55

Figure 4.3: Mean values of end-of-testing C/20 constant current (a) charge and (b) discharge voltage curves with capacity for a replicate group of cells cycled under the 2C, 25oC condition. This group consists of cells 21, 22, and 23, which were all cycled for 1500 cycles. The corresponding mean values of dQ/dV for (c) charge and (d) discharge are calculated from data shown in (a) and (b). All four plots include shaded grey areas that represent two standard deviations. The standard deviations are not noticeable in the voltage curves ((a), (b)); but in the dQ/dV plots ((c),(d)), the standard deviations are large around the peaks, which are highlighted by the vertical bands 56

Figure 4.4: For each of the 10 replicate groups, the standard deviation of voltage for the end-of-testing C/20 (a) charge and (b) discharge, and the relative standard deviation for the corresponding dQ/dV during (c) charge and (d) discharge. Replicate groups with any value above a 10% relative standard deviation in (c) and (d) are labeled in the legend and represented by a different set of markers. All other replicate groups with smaller relative standard deviations are represented as grey circles. Vertical bands represent the voltage bands of peaks found in the dQ/dV plots in Figure 3(c),(d), where standard deviation is generally larger. 57

Figure 4.5: End-of-testing C/20 (a) charge and (b) discharge voltage curves for each of the three cells found in the replicate group cycled under the 2C, 25oC condition, and cycled for 1500 cycles. The inset of (b) shows a zoomed in plot of the voltage, where voltage measurements for cell 22 have an oscillating behavior. This can explain the oscillatory behavior of cell 22's dQ/dV plot for (c) charge and (d) discharge. 59

Figure 4.6: Nyquist plot of the mean value of EIS measurements at SOC=30% of cells 1,2,3,4. These cells have undergone cycling for 300 cycles, under 2.67C and 25degC conditions. The shaded grey area represents two standard deviations. 59

Figure 4.7: The relative standard deviation of the (a) real and (b) imaginary impedance as a function of frequency for each of the 12 replicate groups, for SOC=30%. The blue square markers represent a replicate group that has high relative standard deviation (2C, , 25degC, 300 cycles). All other replicate groups with smaller relative standard deviation are plotted as grey circles. 60

Figure 4.8: Nyquist plot of EIS measurements at SOC=30% for cells 13,14,15,16. This replicate group set (2C, 25degC, 300 cycles) is represented as having high relative standard deviation in Figure 4.7 as blue square markers..... 61

Figure 4.9: (a) Maximum residual percentage errors for real and imaginary values for all 141 collected EIS spectra is shown as a histogram. Nyquist plots of EIS spectra for (bi) cell 33 at SOC=10% and (ci) cell 10 and SOC=30%. Data is shown as blue square markers while the orange line is the fitted result from the Lin-KK model. The corresponding percentage residual error from the fit of real and imaginary data to the Link-KK model at all frequencies is plotted in (bii) and (cii). The highest real residual error shown in (bii) is 4.63%, and in (cii) is 5.02%, which are plotted and indicated by the arrows in (a). 62

Figure 4.10: Organizing principles for primary, secondary, and tertiary metadata 63

Figure 4.11: Proposed schema from the Battery Genome Group. This includes primary, secondary, and tertiary metadata..... 66

Figure 5.1: Parameter optimization results for first dataset. 72

Figure 5.2: Optimization results from second dataset. 72

List of Tables

Table 2.1: Constant Parameters	13
Table 2.2: Results for twenty-four King County Metro routes.....	21
Table 2.3: Comparison of Route Dynamics results with values found in literature	23
Table 3.1: Experimental matrix for cell-level drive-cycle testing	32
Table 4.1: Experimental matrix for JCDREAM dataset.....	52
Table 4.2: Metadata checklist, following Battery Genome primary metadata suggestions.....	64

Acknowledgements

This dissertation would not have been possible without the endless support that I received from friends, family, mentors, professors, and colleagues over the past five years. I am incredibly grateful for my time at UW and everyone I had the opportunity to work and interact with. I will never be able to thank everyone enough, but I would like to acknowledge the impact that many have had.

First, I would like to give sincere thanks to my advisor and PhD committee chair, Professor Dan Schwartz. I am thankful for your holistic mentoring approach, for challenging me as a researcher, while also encouraging me to grow professionally as a science communicator and entrepreneur. Thank you to Professor Dave Beck, for not only being a member on my committee, but also teaching me most of the data science tools and software development skills I know. Your class was essential for my research success. Thank you to Professor Stu Adler for bringing thoughtful questions and feedback to my committee meetings. Many thanks to Professor Jessica Kaminsky for representing the graduate school on my committee. I really appreciated your questions regarding equity and climate justice in my transit research. Lastly from my committee, I would like to thank Danny Ilioiu from King County Metro. Thank you for showing Dan I around the south base a few years ago, always being willing to share information and answer questions, and for offering your perspective.

Furthermore, I am so grateful for my EMI Lab family. I want to especially thank Dr. Victor Hu, who has been an amazing desk neighbor, teacher, editor, debugger, Zoom yoga buddy and most importantly a close friend. Also, I am thankful for Dr. Linnette Teo, for being a great friend, for being homework partners our first year, and for teaching me how to play ultimate frisbee. Victor and Linnette, I am so glad we had the opportunity to work on a couple projects together, and I will greatly miss our lunch dates! Lots of thanks to Dr. Matthew Murbach, Dr. Karl Oleson, Dr. Yanbo Qi, Dr. Caitlin Parke, Dr. Akshay Subramanian, Maitri Uppaluri, Mihyun Kim, and Baochen Li for all your feedback and help in the office, and for the great conversations and memories out of the office as well. I would also like to thank Yuefan Ji and Rose Lee for joining our group this year. I am so glad I got to meet you and wish you all the best!

As mentioned above, the DIRECT data science classes were paramount to progressing my research. I am grateful for the teams I was able to work with on the capstone project that would become Route_Dynamics. Thank you to Dr. Harrison Goldwyn, Ryan Carlin, Dr. Atinuke Ademola-Idowu, Yohan Min, and Kaiming Tao for all of your software contributions. The Chemical Engineering Department has been an important source of community during my PhD and consequently a source of valuable friendships. I would like to thank Dr. Luke Gibson, Dr. Jon Witt, and Dr. Brian Gerwe for being active members of our student ECS chapter, and therefore great partners to learn electrochemistry with, sometimes over a beer. Thank you to Dr. Brittany Bishop for being my science policy mentor and introducing me to the Graduate and Professional Student Senate, another source of community on campus. Thank you also to Dr. Caitlyn Wolf, Dr. Elena Pandres, Hawley Helmbrecht, and Sage Scheiwiller for making me feel welcome in the department, being great listeners, and for convincing me to get a cat. Thank you to undergraduate researchers, Lynna Truong, Sebastian Peck, and Manoli Tramountanas, for your contributions and perspectives. I am also grateful for the network of friends I have across the globe, who have been cheering me on along the way. Thank you to Emily Hultin, Sonja Jacobson, Jenna Kuipers, Caitlin Burgess, Helaina Hurwitz, and Connor Schleicher for checking on me often and reminding me there is a world outside of grad school.

Lastly, tremendous thanks to my family for their love and support. Thank you to my parents, Matt and Tammy Eggleton, who have always told me I can do anything I put my mind to. Thank you for instilling in me the love of learning and the value of personal growth. Thank you to my grandparents, Harold & Gail White and Margie & Jim Ogden. Your warm phone calls, letters, and care packages always brighten my day. To my new second family, Mark, Nancy, Amelia, and Anders Bergson, thank you for all your encouragement. Finally, thank you to my husband Olaf Bergeson, who has been my rock. Olaf, I do not know how I would have gotten to this point without you.

Dedication

To my parents,
Thank you for always believing in me

Chapter 1 - Introduction

1.1 Motivation

Climate scientists have shown that the planet is undergoing significant warming. As populations grow, consumption of goods and electricity increases, and transportation becomes global, carbon emissions consequently rise at a rate that exceeds the earth's natural carbon capturing processes¹. These excess emissions are trapped in the atmosphere, and due to the greenhouse gas effect, global temperatures rise. The Intergovernmental Panel on Climate Change (IPCC) predicts that if global temperatures rise by 1.5°C, there will be catastrophic results². However, there are steps that society can take to slow the temperature rise. A follow-up report by the IPCC in 2022 stated that global CO₂ emissions must reach net-zero by 2050. It is estimated that around 15% of emissions globally can be reduced by creating transportation alternatives.³ Moreover, according to the most recent Inventory of United States Greenhouse Gas Emissions performed by the EPA, transportation is the greatest producer of emissions for the US, making up 27% of total emissions in 2020⁴. Therefore, electrifying personal vehicles, transit, and freight would significantly improve emissions.

Many countries and regions have enacted policies to invest and support transportation electrification. Currently, China and Europe dominate the personal electric vehicle (EV) market.⁵ For example, EVs currently make-up 25% of total vehicle sales in China. With respect to transit, their fleet of battery-electric busses make up 98% of the global fleet. The US is lagging as a market player, but recent federal legislation will make historical investments. The Bipartisan Infrastructure Investment and Jobs Act will allocate billions of dollars to EV charging infrastructure and growing battery-electric bus fleets for transit and schools.⁶ The International Energy Agency (IEA) conducted an analysis of all emissions sectors to estimate changes need to reach net-zero. They showed in their 2021 Transport Report, that in order to reach net-zero emissions by 2050, 20-50% of personal vehicle trips will shift to public transit, depending on the city.⁷ This could motivate more emphasis on electrifying transit, especially buses, instead of focusing solely on personal vehicles.

King County and King County Metro have been leaders in reducing green-house gas emissions and electrifying transit within the US. Not only did Metro have the fastest growth rate in transit riders in 2017 in the country, but has committed to a 100% zero-emissions bus fleet by 2035.⁸ In a feasibility report by King County Metro, the main risks and unknowns related to building the zero-emissions fleet was deciding between low and high capacity batteries and their corresponding fast-charge or slow-charge charging infrastructure, and predicting if these options would meet their needs.

This work will show the value of using multiscale models from the energy systems level to the molecular level to design and minimize risk of the transition to electrified transportation.

1.2 Energy Storage

Energy storage systems allow energy to be mobile or allow it to be used later, rather than immediately after generation. Lithium-ion (Li-ion) batteries are a common form of energy storage. These batteries consist of a negative electrode or anode (typically graphite), a positive electrode or cathode (typically a lithium metal oxide), a separator, and an electrolyte. Lithium ions intercalate between electrodes of different chemical potentials, while the respective electrons travel through an external circuit. When discharging, the electrons and lithium ions move toward the positive electrode, and as the electrons pass through the circuit, they apply electrical energy to the connected load. When charging, electrical energy is applied and the lithium ions sandwich themselves between layers of graphite in the anode, which is a less favorable state. Li-ion batteries were invented in the 1960s with the creation of insertion electrodes⁹. They were essential for consumer electronics, where research and development focused on making the batteries as small and energy dense as possible. In the past decade, another use-case for lithium-ion batteries is becoming more significant, as energy storage for electric vehicles. With climate concerns increasing and fluctuating gas prices, electric vehicles are becoming more popular. At the same time, Li-ion pack prices are decreasing, at a rate of around 15% a year over the past five years¹⁰.

This work will focus on Li-ion batteries for electric vehicles with emphasis on packs for mass transit applications. Batteries for these use cases experience abuse from high charge and discharge rates, operating in unideal voltage windows, and sometimes extreme temperatures.

For large electrified vehicles, the two main obstacles to implementation are related to vehicle range, or battery energy capacity, and cost¹¹. The battery research field has completed numerous studies to find ideal battery chemistries that balance capacity, cost, and safety. Chemistries with Lithium-Iron-Phosphate (LFP) or Nickel-Manganese-Cobalt (NMC) as the cathode material are often in the lead for electric buses.^{12–15} To maintain safe conditions for batteries in-use, and to increase battery lifetime, consequently reducing costs and limiting environmental impacts, battery monitoring and management are also essential to transportation electrification.¹⁶

1.3 Multiscale Models

Managing the energy storage system (ESS) on-board a battery-electric bus is a multiscale problem and requires insights from multiscale models. This holistic approach has been utilized for electric vehicles in multiple cases, such as EV-grid integration¹⁷ and powertrain optimization¹⁸.

1.3.1 Vehicle Dynamics Models

On the systems-level, a vehicle dynamics model, a model common in the field of vehicle design and testing can be used to understand power and energy requirements.^{19–22} The vehicle dynamics models calculate loads by balancing the traction and resistive forces the vehicle experiences. Input parameters such as route topography, ridership, and the vehicle's drive cycle can also be considered. The model is expanded to estimate the load experienced by the energy storage system by including drivetrain and battery management system specifications. This model has been used to estimate remaining range for EVs²³, for building fleets and charging strategies for heavy duty trucks^{24,25}.

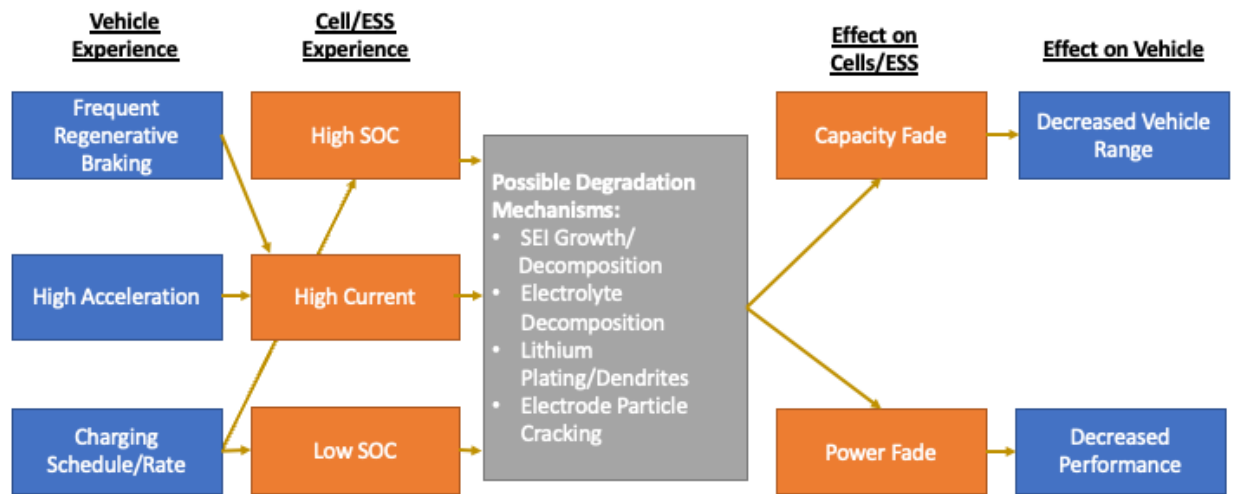
1.3.2 Battery Models

Equivalent circuit models are a common starting point for modeling Li-ion batteries. This method combines circuit elements that represent conditions experienced by the battery. To start, the battery is first assigned an open-circuit voltage (V_{oc}). This is the condition in which the cell is at equilibrium and acting as a voltage source. The open-circuit voltage varies, depending on how charged the cell is and the cell's temperature.²⁶ The level of charge is called state-of-charge (SOC), where 100% is fully charged and 0% is completely discharged. SOC describes the amount of

usable capacity between a lower and upper voltage cutoff, which are set for safety and longevity. The voltage range varies depending on cell chemistry. Next, a circuit element must account for the fact that the terminal voltage, or voltage output, is lower than V_{OC} when discharging and higher than V_{OC} when charging. This can be represented by a resistor. The resistance is also a function of state of charge. This simple model allows us to create a relationship between terminal voltage, current, resistance, and V_{OC} , which will be used later in Chapter 3.

1.3.3 Degradation Models

As batteries age, they degrade, leading to capacity fade and power loss. Studies in the literature have identified various degradation mechanisms, what cell experiences cause them, and how we can monitor cell health with these conditions in mind. ^{27–32} Figure 1.1 relates the cell experiences and effects to those experienced by a vehicle. Vehicle experiences of interest include: regenerative braking frequency, high accelerations, and charging schedules and rate as they lead to decreased vehicle range and performance.



Adapted and Expanded from: Birkl, Howey et al., Journal of Power Sources 341 (2017)

Figure 1.1: Relating vehicle and cell experiences to degradative results.

1.4 Open-Source Software and Data

There has been a push in the discipline of chemical engineering, to include data science techniques, large datasets, and open-source tools as teaching materials and valuable research

products³³. Open-source software tools for batteries are also becoming more common in the battery field. These tools are used for battery cell and pack modeling^{34,35}, EIS fitting³⁶, and initializing database structures for data storage³⁷. Impedance.py was a product of a Hackweek at an Electrochemical Society meeting, an event meant to introduce the impact software tools can make for furthering electrochemistry and battery science, while also teaching basic data science and software development skills³⁸. Collectively, these tools have hundreds of stars and forks on GitHub, which is a decent metric for estimating their use and value to the community.

There are also numerous groups who are sharing open battery data³⁹, and work is being done to create a standard for battery data sharing⁴⁰. Having these datasets and tools openly available, allows other scientists and engineers to build-upon them. There are also machine learning models that could be applied to batteries, but limitations in large enough datasets have delayed their use. This work will show an example of how to share battery data effectively, while also including an open-source systems-level tool that can be integrated into other software tools.

1.5 Dissertation Roadmap

This work uses multiscale modeling and open-source software to improve the process of transportation electrification, especially for battery-electric buses. Chapter 2 starts at the systems-level to model the load and energy requirements for a bus energy storage system along a given route. The 1D longitudinal dynamics model is used to estimate the forces applied on the vehicle. Route elevation, bus stop locations, traffic signal locations, ridership, and speed limits are inputs to the model.

In Chapter 3, the load profiles for a given route are translated into cell-level loads. We conducted cycling experiments for two routes, at two starting SOCs and with fresh and aged cells. The resulting voltage and current data allowed us to calibrate for cell resistance and open circuit voltage. A simplified battery model allows us to bin voltages, similar to a typical battery management system (BMS).

Chapter 4 introduces the issues that occur when sharing and utilizing open-source battery data. We created a cycling dataset for commercial Samsung Li-ion cells, focusing on replicate

data. The results are labeled and organized using metadata and structures supported by the Battery Data Genome project.

Chapter 5 gives examples of projects that have also been worked on during this PhD. While they do not directly contribute to the transportation electrification theme of this dissertation, they support the call for more open-source software and contribute to a diverse portfolio of low-emissions solutions for the industrial sector. First, a set of Jupyter Notebooks user guides are created for a software that uses machine learning to create process system design flowsheets. The notebooks guide the user through the process. Second, a model for Solid-Oxide Fuel Cells were optimized, so the model could be used as a unit for the process flowsheet software. We fit experimental data to the model using `scipy`'s optimization function, allowing us to define parameters for the fuel cell model.

Finally, Chapter 6 summarizes main lessons learned through these projects and proposes future areas of study.

Chapter 2 - Route_Dynamics: an Open-Source Python Package for Determining Energy Requirements and Battery Fatigue for Electric Bus Fleets

Note – this chapter is in preparation to be published as a journal article

Abstract

As bus fleets transition to battery-electric buses, there exist knowledge gaps, which include but are not limited to charging infrastructure placement and demand, battery sizing for optimal vehicle range, and the effect of load demands on battery lifetime and performance. We use a longitudinal vehicle-dynamics model to estimate the power and energy required to transport a battery-electric bus across a given route, using King County Metro bus routes as a case-study. Data inputs for the model include route GIS data for route elevation and locations of route events (bus stops and traffic signals), ridership data to estimate vehicle mass, and specifications for the vehicle and on-board energy storage system (ESS). Routes are compared based on load profiles and distributions for the ESS. We see that route elevation and accelerations have a significant effect on load demands.

2.1 Introduction

Many transit agencies are committed to mitigating their environmental impact and are transitioning to electrified bus fleets ^{41,42}. For battery electric bus fleets, the two main obstacles to implementation are related to vehicle range, or battery capacity, and cost ⁴³⁻⁴⁵. The battery research field has completed numerous studies to find ideal battery chemistries that balance capacity, cost, and safety. Chemistries with Lithium-Iron-Phosphate (LFP) or Nickel-Manganese-Cobalt (NMC) as the cathode material are often in the lead for electric buses ⁴⁶⁻⁵⁰. Each battery manufacturer provides a typical vehicle range, but the true range can vary greatly, depending on vehicle and route conditions.

With a transition to battery electric buses comes a complex set of novel maintenance and scheduling challenges for fleet managers. Battery energy storage systems (ESS) degrade based on how they are used, how they are managed and charged, and the specific chemistry (or even the specific generation of a given materials chemistry), making prediction of remaining usable lifetime and new strategies to extend cell lifetimes key areas of research ⁵¹. A lack of operational experience means that maintenance is not yet optimized, creating a risk of excessive maintenance or reactive maintenance, either of which reduces the economic value and environmental benefits of battery electric fleets. The location of chargers and charging time will also need to be considered in fleet logistics. Demand charges during peak demand times can significantly increase the cost of an electric fleet ⁵².

Recent research in transit modeling has linked vehicle dynamics models with battery models and operating conditions ^{19,20,53-57}. Others have created optimization models to determine the most efficient route based on charging events and route efficiency ⁵⁸⁻⁶². We aim to combine some of these methods, while also allowing for user inputs of multiple data types. Uncertainty of operating conditions and route characteristics greatly influences load and energy estimates, so accurate input data is essential for effective route planning ⁶³⁻⁶⁵.

Motivated by the obstacles mentioned above and the recent literature, we created a model and a complementing open-source Python package that uses a vehicle dynamics framework and route characteristics to estimate the load on the battery and net energy, as the basis for predicting

route features that will impact battery replacement. Load profiles can be related to known degradation mechanisms for many lithium-ion battery chemistries. For example, high C-rates for charging and discharging are known to cause significant degradation⁶⁶. Route_Dynamics aims to characterize the actual drive cycles for different routes in the King County Metro system, identifying the potential high degradative events, and using this data to rank routes by wear-and-tear on the ESS. King County Metro, the transit agency for the Seattle metropolitan area plans to have a fully electric fleet by 2034⁶⁷. Metro has completed a pilot program and begun fleet acquisition, allowing some basic checks between the results presented here and performance in the field.

2.2 Methodology

2.2.1 Vehicle Dynamics Model

Our software was designed based on the longitudinal vehicle dynamics model found in the literature^{20,68-70}. The forces applied on the bus, including gravitational, rotational, aerodynamics drag, and acceleration forces are calculated to determine the net force needed to accomplish a certain velocity and acceleration profile. The required inputs include road grade, vehicle mass (including cargo/passengers), velocity, acceleration, and vehicle parameters (surface area, drag coefficients, etc.), as seen in Figure 2.1.

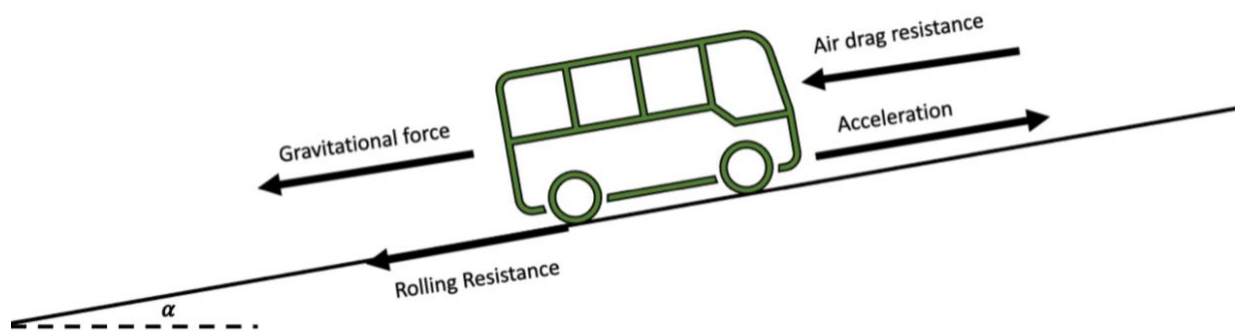


Figure 2.1 Forces acting on vehicle and included in the longitudinal vehicle dynamics model

The forces are calculated as follows:

$$F_{total} = F_{acceleration} + F_{grade} + F_{rolling} + F_{air} \quad (1)$$

Where the individual forces are given as

$$F_{acceleration} = \frac{dv}{dt} \cdot f \cdot m, \quad (2)$$

$$F_{grade} = m \cdot g \cdot \sin \alpha, \quad (3)$$

$$F_{rolling} = m \cdot g \cdot \cos \alpha \cdot c_{rr}, \quad (4)$$

and

$$F_{air} = \frac{1}{2} \rho \cdot A \cdot C_d \cdot v^2. \quad (5)$$

Here, the variable v is the velocity, $\frac{dv}{dt}$ is the acceleration, f is the mass or inertia factor due to rotating parts, m is mass, g is the gravitational constant, α is road angle, c_{rr} is the rolling friction coefficient, ρ is air density, A is the vehicle's front surface area, and C_d is the air drag coefficient. The traction power requirements for driving the vehicle is the force times velocity:

$$P_{traction} = F_{total} \cdot v \quad (6)$$

This is the power required to move the vehicle at the desired acceleration with the given resistances. To relate this to the power requirements for the battery, drivetrain performance must be considered. The drivetrain layout assumed for this study, is shown in Figure 2.2.

The power drawn from the battery includes the traction power required to propel the vehicle, the power required for auxiliaries, and the conversion efficiencies in each train:

$$P_{ESS,discharge} = \frac{P_{traction}}{\eta_m} + \frac{P_0}{\eta_{aux}} \quad (7)$$

where η_m is the overall propulsive efficiency of the drive train motor and inverter, whereas η_{aux} is the overall efficiency of the auxiliary demand, P_0 , which can include a wide range of load traits from heating and cooling, to lighting and instrumentation. In this study, auxiliary power is constant.

Key:

— Mechanical Link

↔ Electrical Link

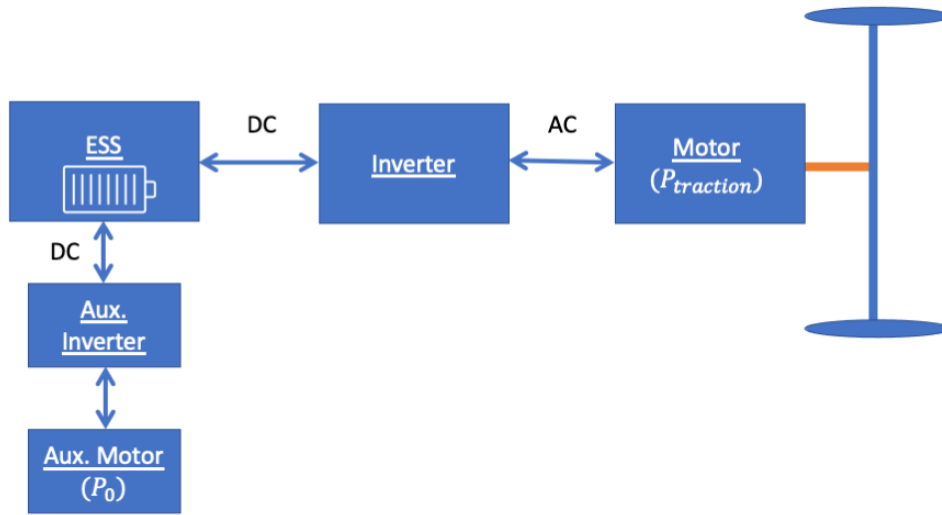


Figure 2.2: Drivetrain layout assumed for this case study

Regenerative braking occurs when there is a negative traction power. Because there is a limit to how much power can be regenerated, a regeneration factor (r_{gen}) is added, so equation (7) is modified to:

$$P_{ESS,charge} = r_{gen} \eta_m P_{traction} + \frac{P_0}{\eta_{aux}} \quad (8)$$

in which r_{gen} is the fraction of the load that can be regenerated from braking.

The simplest implementation of the power control system for propulsion and regeneration applies constraints on the ESS system, such that:

$$P_{ESS} = \begin{cases} \text{Eq (7)} & \text{if } F_{tot} \geq 0 \text{ and } P_{traction} < P_{out_max} \\ \frac{P_{out_max}}{\eta_{drive}} + \frac{P_0}{\eta_{aux}} & \text{if } F_{tot} \geq 0 \text{ and } P_{traction} \geq P_{out_max} \\ \text{Eq (8)} & \text{if } F_{tot} < 0 \text{ and } P_{traction} > P_{in_max} \\ r_{gen} \eta_{drive} P_{in_max} + \frac{P_0}{\eta_{aux}} & \text{if } F_{tot} < 0 \text{ and } P_{traction} \leq P_{in_max} \end{cases}$$

where P_{out_max} is set by the maximum power the drive system can deliver for propulsion, and P_{in_max} is the maximum recuperation power.

The total energy demand is:

$$E_{ESS} = \int_0^T P_{ESS} dt \quad (9)$$

Finally, the constant parameters assumed in this study are listed in Table 1, as found in the literature. For this study, we are assuming the vehicle is a 40' New Flyer Xcelsior Charge. This model has the most parameters available, because it underwent a comprehensive performance test at Penn State University⁷¹. It is also made by the same manufacturer of the fleet being acquired by King County Metro.

Table 2.1: Constant Parameters

Parameter	Value [units]	Citation
Drag Coefficient (C_d)	0.6	Abdelaty & Mohamed ⁷²
Mass factor/Inertia factor (f)	1.1	Gallet et al. & Asamer et al. ^{19,20}
Rolling Friction Coefficient (c_{rr})	0.01	Abdelaty & Mohamed ⁷²
Drivetrain Efficiency (η_{drive})	0.89	Abdelaty & Mohamed ⁷²
Regeneration Factor (r_{gen})	0.6	Gallet et al ¹⁹
Auxiliary Efficiency (η_{aux})	0.89	-
P_{out_max}	160 [kW]	New Flyer Xcelsior Charge ⁴⁷
P_{in_max}	-160 [kW]	New Flyer Xcelsior Charge ⁴⁷
Auxiliary Load (P_0)	7 [kW]	Abdelaty & Mohamed; Vepsäläinen et al. ^{63,72}
Air Density (ρ)	1.2 [kg/m ³]	-
Mass per Passenger (m_{pass})	75 [kg]	Gallet et al. ¹⁹
Vehicle Mass	13,041 [kg]	New Flyer Xcelsior Charge ⁴⁷
Front Surface Area (A)	8.58 [m ²]	New Flyer Xcelsior Charge ⁴⁷

2.2.2 Software

The package was designed in a modular format, so that the user can investigate various levels of detail, depending on what data is available. Figure 2.3 shows the logic flow of the `route_dynamics` package. First, route shapefiles and elevation data are combined to create a geodataframe in the `route_elevation` module. This dataframe is passed to the `route_accel` module where an artificial drive cycle is created using known route events, such as bus stops and traffic signals. This module also imports vehicle specifications, such as regenerative braking limits, that will be used later to estimate battery charging during use. The `route_riders` module creates a dataframe that includes the total mass from passengers at every bus stop along the route. The road grade, drive cycle, and total mass are then combined in the `route_energy` module, where the vehicle dynamics model equations are solved to give the load estimate. The results can be viewed using simplified functions established in the `route_visualizer` module.

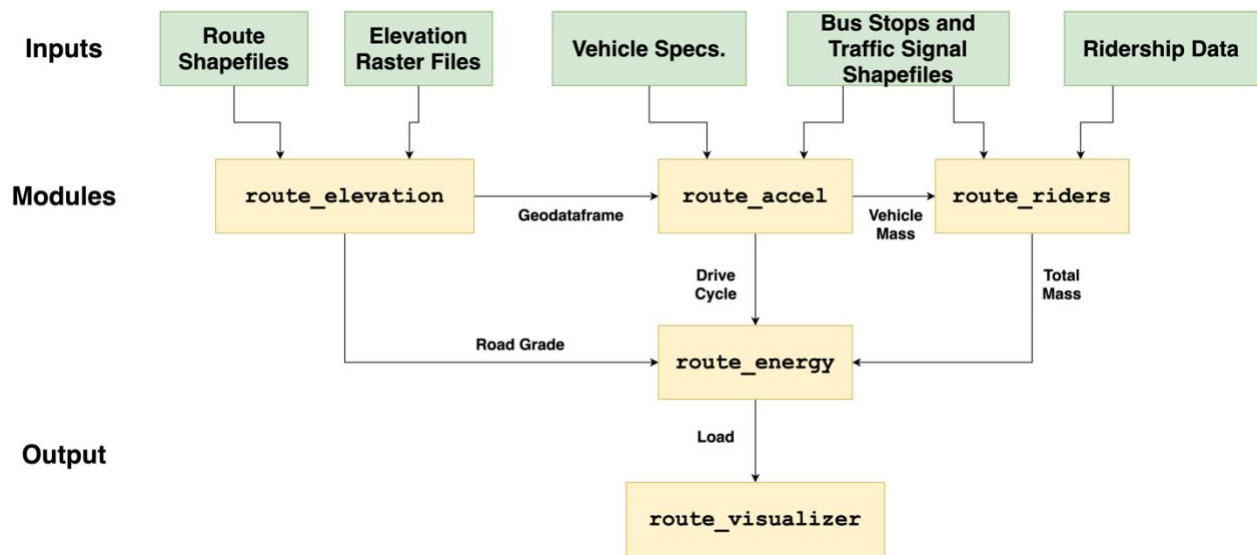


Figure 2.3: Logic flow of the `route_dynamics` package. Green boxes are data inputs, and yellow boxes are package modules.

For King County, the data inputs include: 3 ft resolution LiDAR elevation data from the Department of Natural Resources ⁷³, route, bus stop, and traffic signal shapefiles from the King County GIS portal ⁷⁴, and ridership from King County Metro records. Figure 2.4 shows the input data types and how they relate.

The LiDAR elevation data gives the “data surface model” (DSM), or the highest-hit elevation value. This file was chosen over the digital terrain model (DTM) or digital elevation model (DEM), which give the elevation values of the natural terrain or bare earth respectively, because there are surface level information, such as bridges, high-way ramps, and elevated roadways that would not be included. In order to extract accurate road grades, which is the parameter that is used in the vehicle dynamics model, the surface layer was a better option. However, when using the highest-hit points, there are instances where the elevation point may not be the road, but rather a vehicle, pedestrian bridge, powerlines, etc. Therefore, the elevation needed to be filtered before entered into the model. The scipy savitzky-golay (S-G) filter was used, which fits the data using a user-defined polynomial over a selected window ⁷⁵. For this study, elevation was tagged onto points along the routes every 36 feet. The points were fit using a 3rd order polynomial over a 43 point window. This window is equal to about a quarter mile. It was compelling to make sure this data input was accurate, as empirical models in the literature show that road grade has a significant effect on vehicle specific power (VSP). ⁷⁶ A cap is placed on 12% grade, to be in compliance with the King County road design regulations.⁷⁷ The corresponding speed limit is also appended to each point along the route. This protocol is executed in the module, route_elevation.

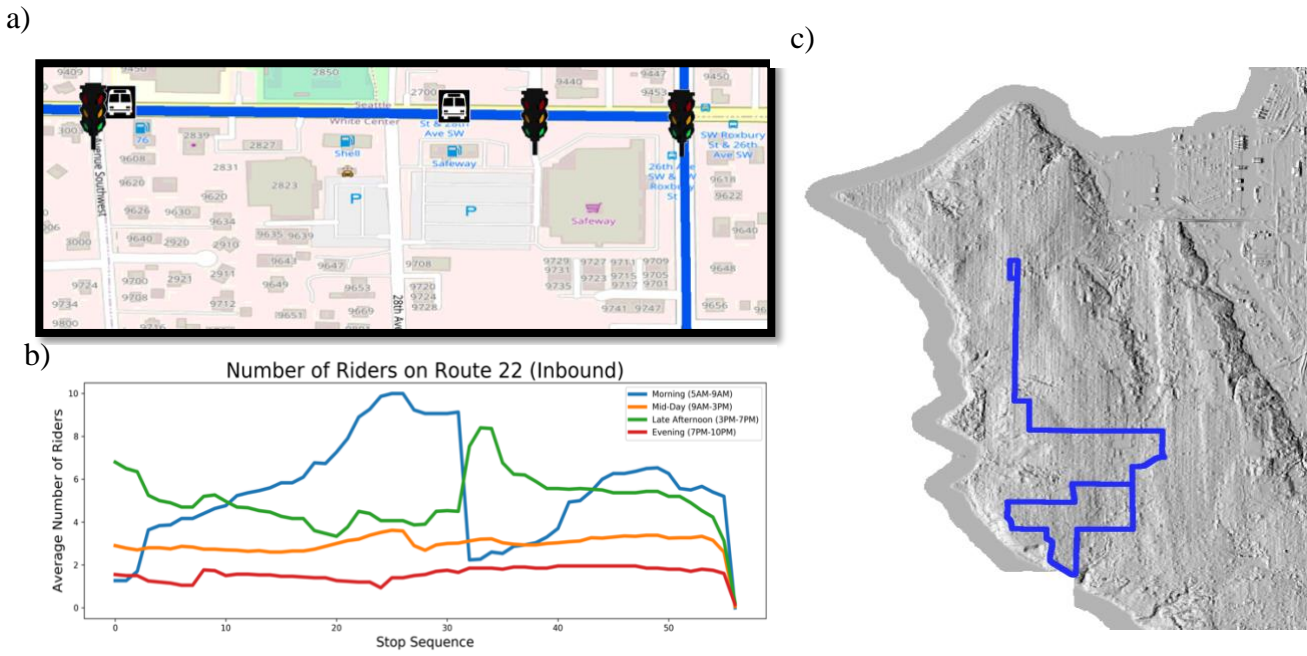


Figure 2.4: a) Zoomed in view of Route 22. Route events such as bus stops and traffic lights have been overlaid. b) Route ridership for Route 22 inbound. c) The shapefile for Route 22 overlaid on the DSM layer for King County

Within the package module, `route_accel`, an artificial drive cycle is created based on the location of bus stops and traffic signals along the route and a preferred start-from-stop acceleration profile provided by King County Metro. This input is also more accurate when considering real-world conditions⁷⁸. To create the drive cycle, the program first determines the distance to the next bus stop for each point along the route. This information is then added to the geodataframe. Then, based on the bus location relative to the stops and signals, the bus either follows the start-from-stop acceleration profile, accelerates at a constant value until the speed limit is reached, maintains a constant speed at the speed limit, decelerates at a constant value, or is stopped. The constant acceleration value used was 0.4 m/s^2 , as this was the value that the start-from-stop profile reached. The negative deceleration value used was -1.5 m/s^2 , as this value has been seen in the literature¹⁹. At each bus stop and traffic signal, it is assumed that the bus waits or is idling for 30 seconds.

The start-from-stop acceleration profile given is a 30 second profile, with data given every second. Before it could be used with the package, it needed to be converted to a spatial profile, rather than time-series. To do this, the profile was integrated twice, once to estimate the velocity at each point, and the second to estimate the distance. A new dataframe was created where distance was the independent variable, and points were given every 36 ft to match the elevation data resolution. For each point, the closest value from the time-series data was found, and then linear interpolation was used to find the corresponding velocity and acceleration values. Figure 2.5 shows the process of converting the time-series data into a spatial format with the resulting acceleration and speed profiles for the start-from-stop sequence. Figure 2.5 then shows the resulting traction power calculation for a flat route with no passengers on-board. It is worth noting that there is a slight wobble in the power calculation. This is due to errors in the acceleration profile due to plot digitizing. This effect will be smoothed out in future versions of this software.

Figure 2.6 gives a half-kilometer example of how an artificial drive cycle could look, given two route events (bus stop or signal) and a speed limit of 40 km per hour (~25 mph). As seen in this example, there are many instances where the vehicle would not complete the entire start-from-stop protocol.

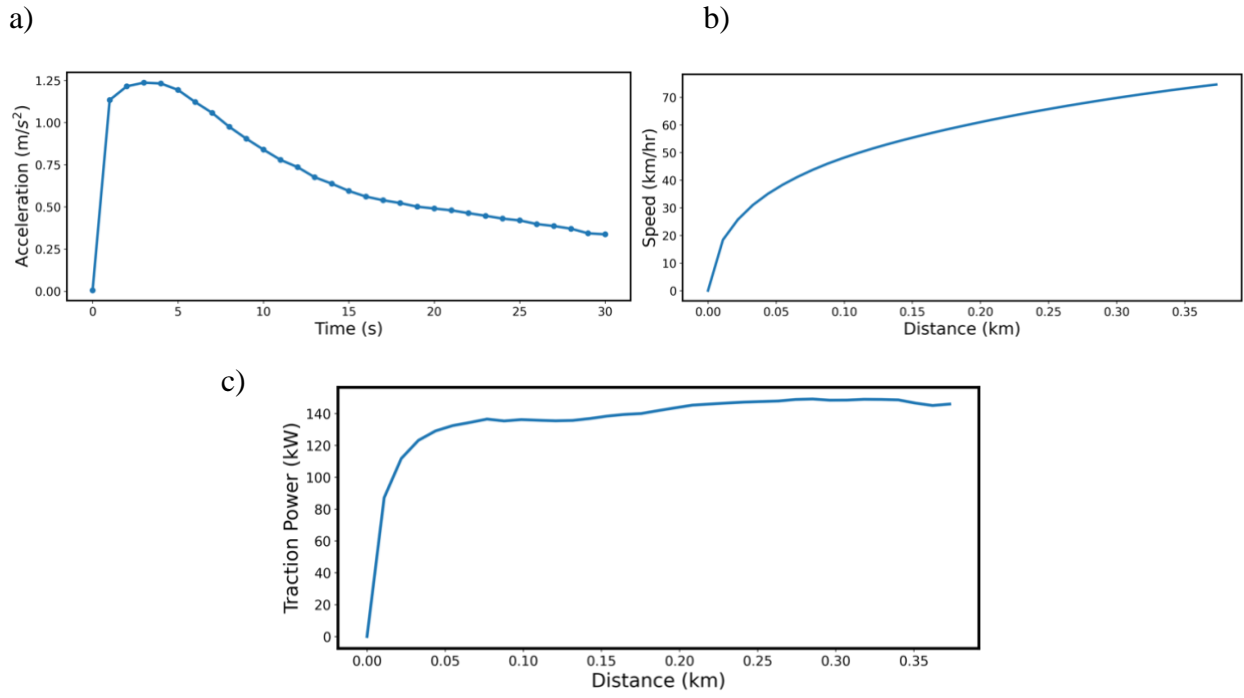


Figure 2.5: The conversion of the time-series acceleration data to spatial. (a) The given start-from-stop acceleration profile. (b) The resulting speed vs. distance profile. (c) The resulting load profile for the start-from-stop profile, assuming 0% road grade.

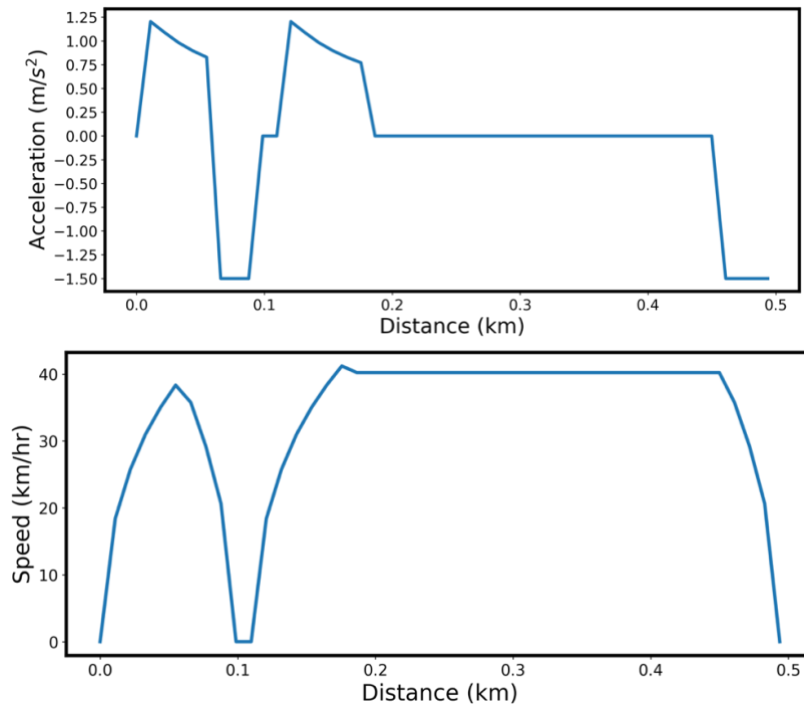


Figure 2.6: An example drive cycle for a section of a route with two bus stops and a speed limit of 25 miles per hour.

2.3 Results and Discussion

There are 24 routes that King County Metro is considering for implementation of electric buses into the fleet, out of roughly 130 total routes. For each route, the round-trip energy and time spent at load extremes were calculated for three scenarios: typical, lightest, and busiest. Table 2.2 shows the results from this study, along with route attributes. The typical case uses ridership data from the time of day which has the median number of riders. For this case, it is assumed that the bus stops at every other bus stop and traffic signal. The results of this case are given as the typical value. For the lightest case, ridership data is used from the time of day with the least number of riders. It is also assumed that the bus stops at every third bus stop and traffic signal. These values are given as the first number in the range. Lastly, for the busiest case, ridership data is used from the time of day with the most riders. It is also assumed that the bus stops at every bus stop and traffic signal. These values are given as the last number in the range.

Load profiles and histograms are also produced. Examples are shown in Figure 2.7, where the load profiles and load distributions for two routes are compared. Route 186 represents the low extreme of load demand, because it spends only 2.5% of the route time in the high and low voltage extremes. On the other hand, Route 22 represents high extreme of load demands, because it spends 7.6% of the route time in the high and low voltage extremes.

Load extremes, especially during heavy regenerative braking, are linked to battery degradation⁷⁹. Thus, evaluating load distributions is one way to evaluate the relative ESS wear-and-tear expected for different routes. Thus, Route 186 would be expected to be less degradative on the ESS than Route 22.

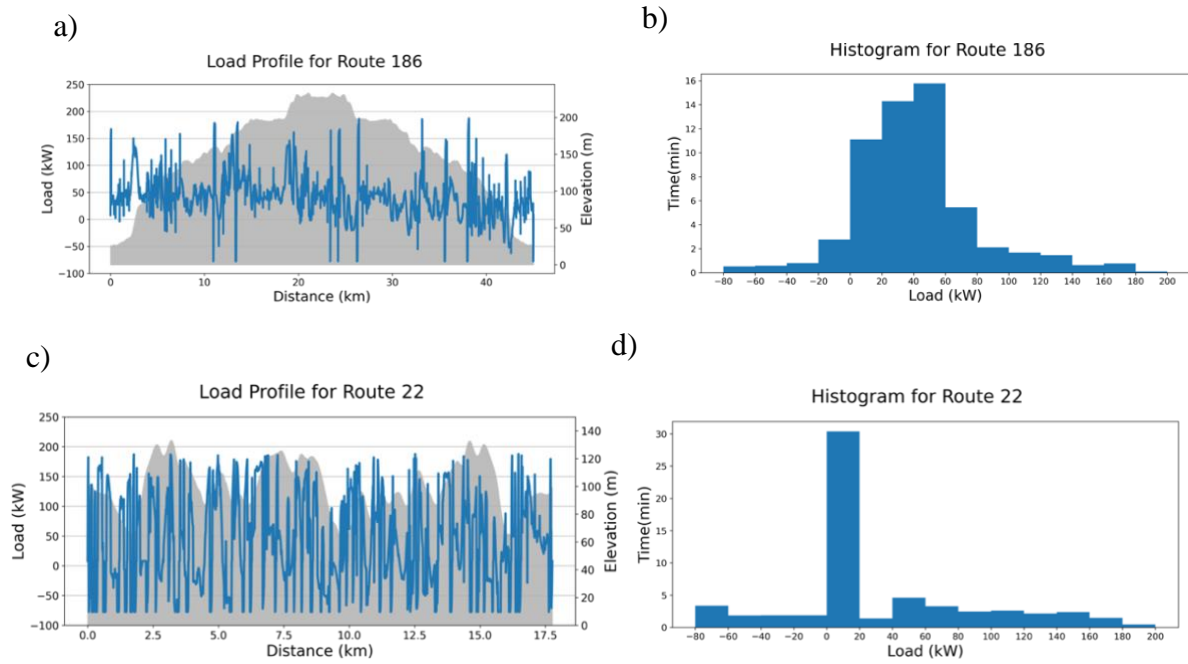


Figure 2.7: (a) Load profile with elevation for route 186. (b) Load distribution for route 186. (c) Load profile with elevation for route 22. (d) Load distribution for route 22.

To understand what causes the differences in load distribution, we break down the forces in Figure 2.8. For Route 22, the shape of the force profile is strongly affected by the variation in gravitational force and acceleration forces. Extreme load events happen during recuperative braking on downhill grades, and accelerating uphill from a stop. In contrast, route 186, which has a more steady elevation change, and it does not make frequent stops, shows many fewer extreme load events.

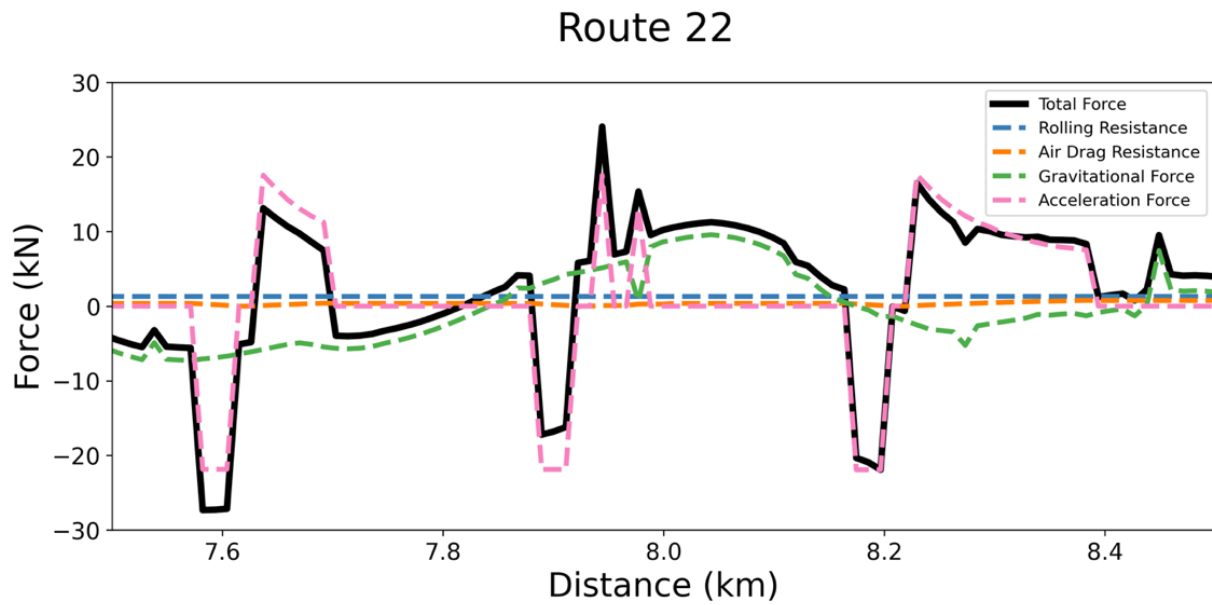
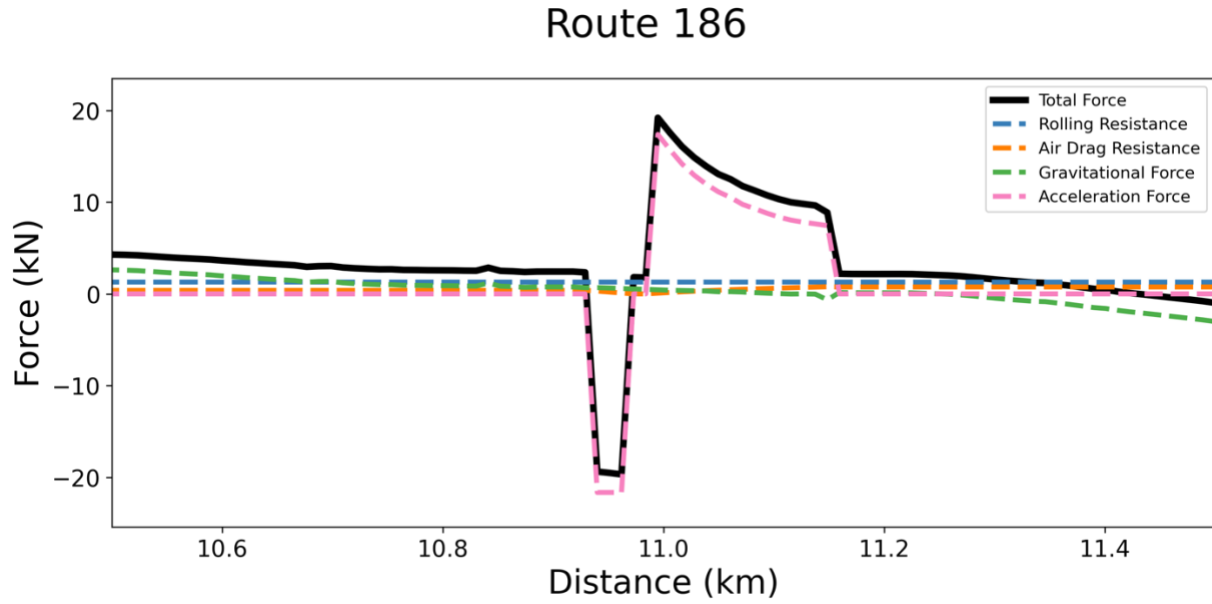


Figure 2.8: (top) Force break-down profile for route 186. (bottom) Force break-down profile for route 22.

Table 2.2: Results for twenty-four King County Metro routes

Route	Round-Trip Distance (km)	Total Number of Bus Stops	Total Number of Traffic Signals	Average Absolute Grade (%)	Average Route Speed Limit (km/hr)	Typical Number of Passengers Onboard [Range]	Typical Energy per Round-Trip (kWh) [Range]	Typical Energy per km (kWh/km) [Range]	Typical Time at Min Load Bin [Range]	Typical Time at Max Load Bin [Range]
22	18	88	16	4.0	51	3 [1 - 8]	30 [28 - 35]	1.7 [1.6 - 1.9]	3.6 [2.2 - 6.7]	1.1 [0.9 - 1.2]
101	36	42	38	2.8	64	21 [14 - 24]	39 [41 - 41]	1.1 [1.1 - 1.1]	2.8 [2.8 - 7.2]	1.7 [1.7 - 1.9]
102	63	60	44	3.1	58	15 [1 - 19]	75 [64 - 78]	1.2 [1.0 - 1.2]	5.4 [3.9 - 11.2]	2.0 [1.9 - 2.7]
In143	83	55	31	2.0	71	11 [1 - 16]	90 [79 - 84]	1.1 [1.0 - 1.0]	5.9 [2.1 - 10.0]	2.9 [1.6 - 5.3]
150	54	77	38	1.7	66	18 [14 - 23]	66 [58 - 61]	1.2 [1.1 - 1.1]	5.8 [3.7 - 11.0]	5.8 [2.9 - 4.8]
153	20	65	65	0.5	53	6 [4 - 9]	23 [24 - 32]	1.2 [1.2 - 1.6]	1.7 [1.5 - 4.4]	1.3 [1.7 - 3.6]
154	24	30	7	0.9	54	8 [1 - 12]	27 [22 - 30]	1.1 [0.9 - 1.3]	1.6 [0.5 - 2.9]	1.3 [0.8 - 2.1]
156	35	93	12	3.8	52	4 [3-7]	51 [44 - 57]	1.5 [1.3 - 1.6]	4.6 [3.7 - 7.9]	2.2 [2.0 - 2.6]
157	68	45	31	2.6	70	16 [13-16]	75 [72 - 79]	1.1 [1.1 - 1.2]	4.7 [3.6 - 7.9]	4.3 [1.7 - 4.7]
158	73	59	31	2.6	72	12 [1 - 15]	81 [71 - 82]	1.1 [0.9 - 1.1]	5.3 [0.3 - 8.7]	3.4 [8.5 - 2.9]
159	79	61	32	2.4	70	5 [1 - 13]	84 [74 - 89]	1.1 [0.9 - 1.1]	4.6 [2.3 - 8.6]	2.5 [1.3 - 3.1]
168	40	103	2	2.3	56	7 [6 - 12]	53 [48 - 63]	1.3 [1.2 - 1.6]	5.3 [4.1 - 9.5]	3.0 [1.7 - 3.9]

169	30	90	90	3.0	54	9 [7 - 15]	46 [39 - 57]	1.5 [1.3 - 1.9]	4.0 [3.0 - 7.9]	1.8 [1.3 - 2.9]
177	56	8	50	2.5	82	12 [8 - 23]	55 [55 - 51]	1.0 [1.0 - 0.9]	3.0 [2.5 - 5.4]	0.6 [0.6 - 0.5]
178	64	19	53	2.5	80	12 [1 - 13]	63 [62 - 61]	1.0 [1.0 - 1.0]	3.5 [2.4 - 5.7]	0.7 [0.8 - 0.9]
179	67	28	43	2.4	81	14 [6 - 16]	69 [64 - 73]	1.0 [1.0 - 1.1]	3.2 [1.4 - 6.2]	1.0 [0.4 - 3.0]
180	60	147	18	1.4	52	13 [8 - 16]	74 [66 - 86]	1.2 [1.1 - 1.4]	6.5 [4.3 - 13.3]	4.4 [2.8 - 6.1]
181	42	101	19	2.3	54	5 [4 - 14]	57 [51 - 65]	1.4 [1.2 - 1.5]	5.0 [3.6 - 9.7]	2.6 [2.3 - 3.4]
182	21	61	13	2.6	46	7 [4 - 8]	28 [24 - 32]	1.3 [1.1 - 1.5]	2.2 [1.3 - 3.9]	0.9 [0.7 - 1.2]
183	29	94	10	2.8	50	8 [3 - 11]	44 [35 - 54]	1.5 [1.2 - 1.9]	4.4 [2.1 - 8.0]	2.1 [1.2 - 3.1]
186	45	72	72	1.3	55	4 [3 - 9]	49 [40 - 59]	1.1 [0.9 - 1.3]	3.0 [0.6 - 5.8]	2.0 [0.5 - 3.9]
187	17	58	12	2.4	53	9 [2 - 11]	26 [19 - 30]	1.5 [1.1 - 1.8]	2.8 [0.8 - 5.2]	1.1 [0.7 - 1.5]
190	51	15	47	2.7	81	14 [14 - 14]	54 [54 - 50]	1.1 [1.1 - 1.0]	3.4 [2.7 - 6.2]	1.0 [0.7 - 0.9]
192	50	22	32	2.8	81	5 [5 - 8]	49 [51 - 52]	1.0 [1.0 - 1.0]	2.9 [2.1 - 5.0]	1.3 [1.4 - 1.3]

These results can be compared to real-world performance and simulations from other studies, as shown in Table 3. Likewise, New Flyer advertises that the range for the 40’ bus is around 260 km or 160 miles for for a 320 kWh BESS capacity⁴⁷. Our range of 0.9 – 1.9 kWh/km would equate to 355 km to 168 km respectively for different routes. King County Metro staff have independently confirmed the reasonableness of these computations (unpublished).

In aggregate, the results presented in Table 2 illustrate some of the planning and operational considerations required for fleet building. In particular, energy demand per km can be quite variable within a given route, and across routes. With the modest energy density and energy storage capacity of an BESS, managing the variability driven by terrain, stops, and passenger load requires careful management. Likewise, the potential value of bus rotations on routes with different load distributions is likely important for degradation and lifetime of the BESS. Having a full set of simulated route cycles for a transit agency considering battery electrification is a low-cost first step for a comprehensive planning process, allowing *in silico* evaluation of different BESS configurations, and a window into routes and their impact on ESS durability.

Table 2.3: Comparison of Route Dynamics results with values found in literature

<u>Study</u>	<u>Vehicle</u>	<u>kWh/km Range</u>
King County Metro (see Table 2.3)	New Flyer 40’ Xcelsior Charge	0.9 – 1.9
Ohio State University ⁵⁴	Not specified	1.26 - 1.34
Aachen, Germany ⁵⁶	18m articulated bus	2.1 – 3.4
Knoxville Area Transit ⁷⁰	Optima LF-34	1.24 – 2.48
Macao, China ⁸⁰	Ankai and BYD 12m	1.38 – 1.75

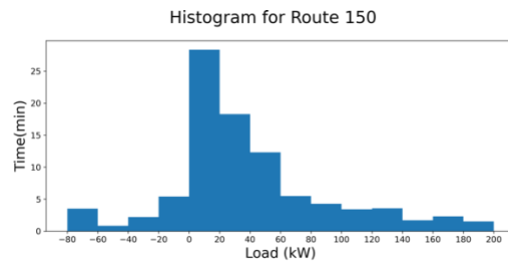
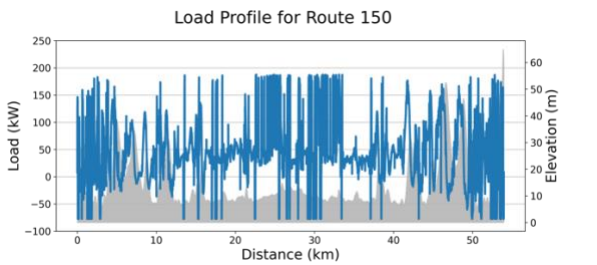
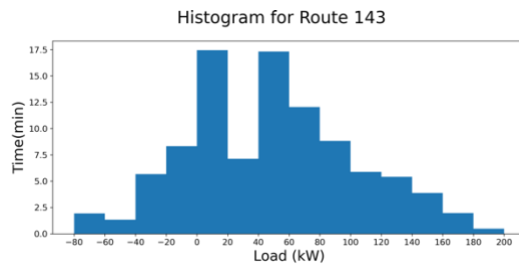
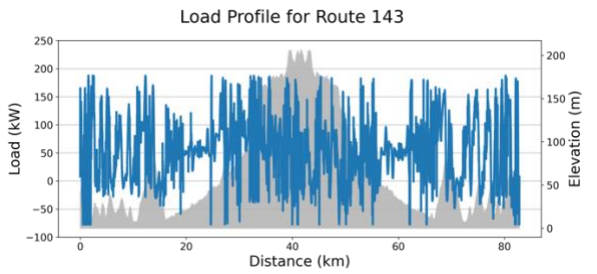
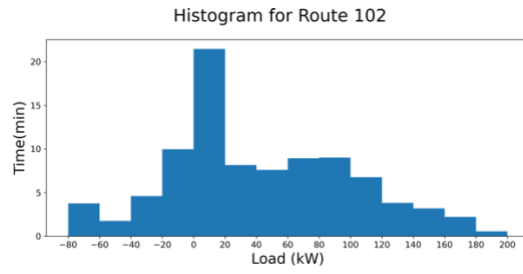
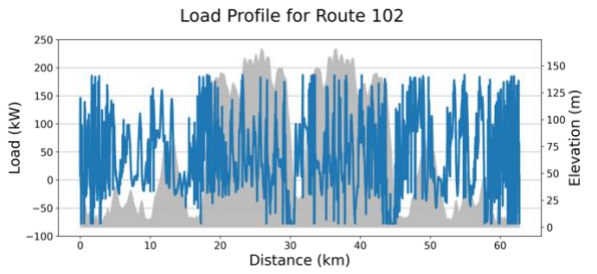
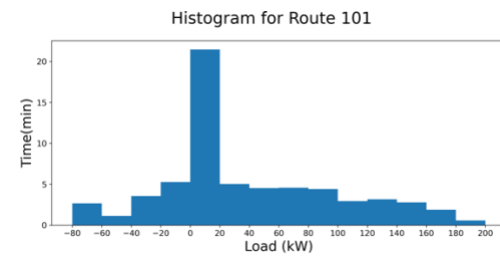
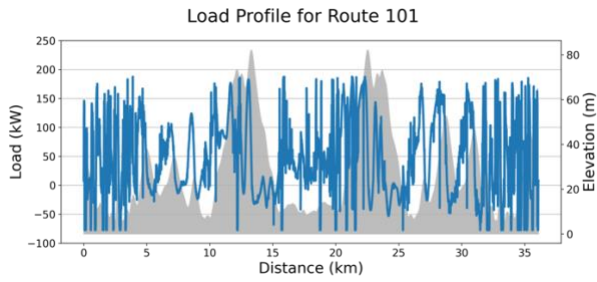
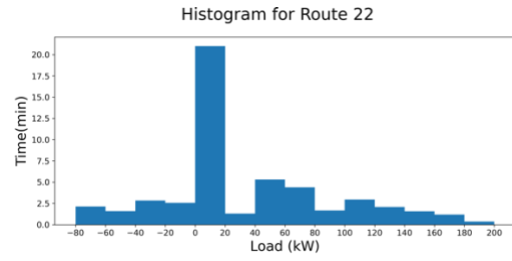
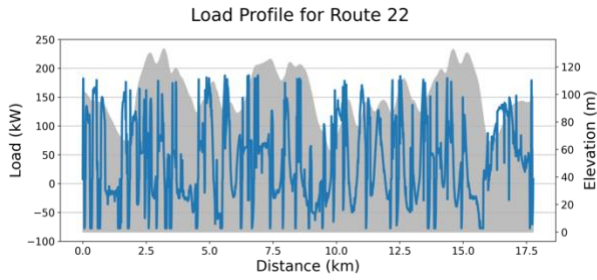
2.4 Conclusions and Proposed Future Work

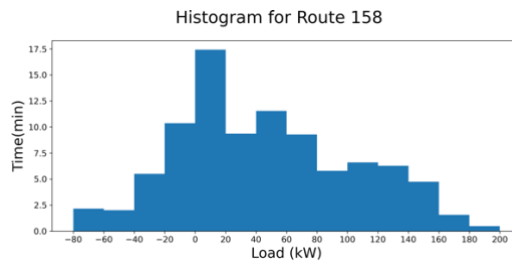
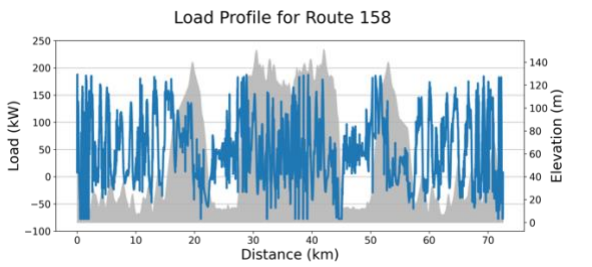
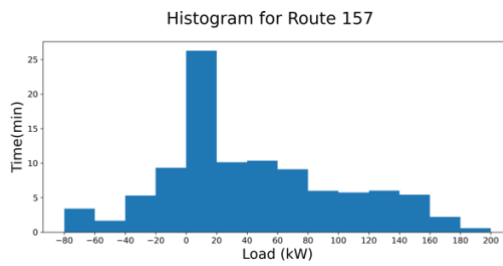
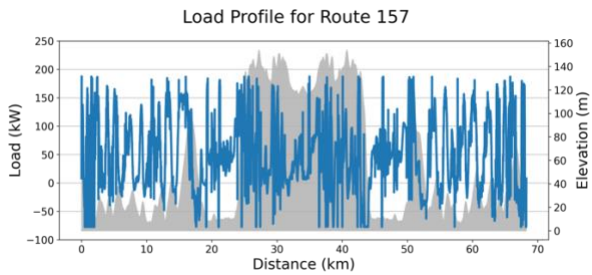
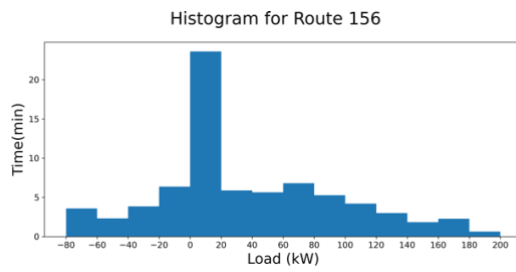
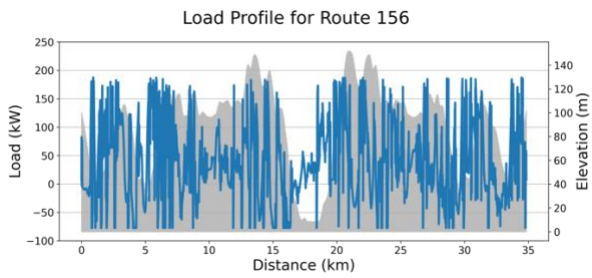
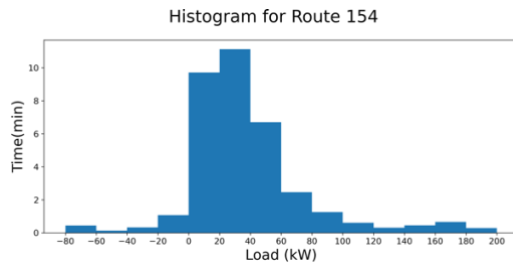
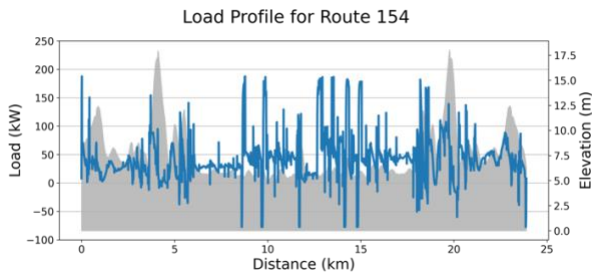
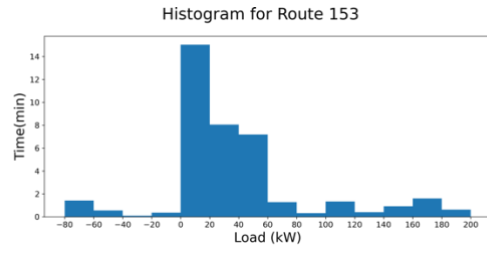
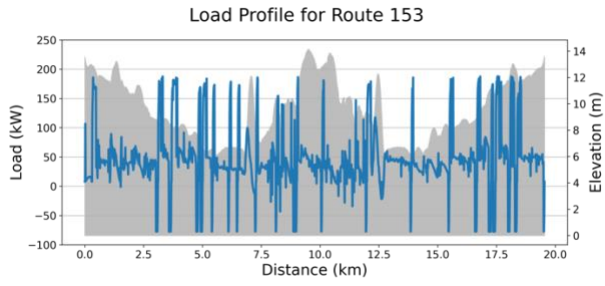
Our hypothesis was that by using spatial route data, vehicle parameters, and ridership data, we would gain insight into route difficulty. With this tool, we were able to compare routes based on energy and load requirements. This information will be able to help create guidelines and best practices for transit operators to minimize degradative events for the lithium-ion battery modules. The open-software framework also allows for the integration of more specific battery models.

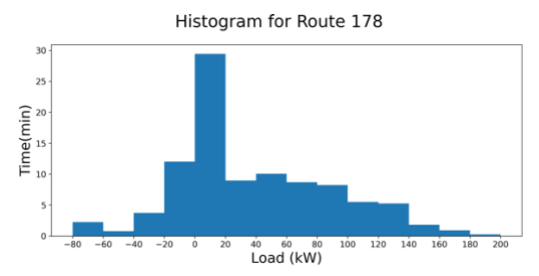
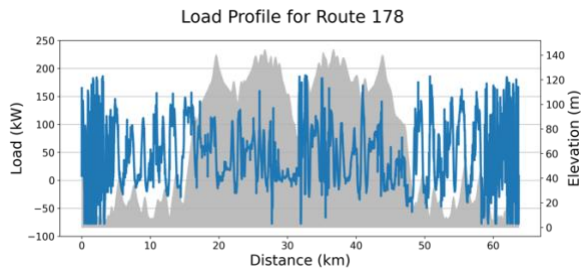
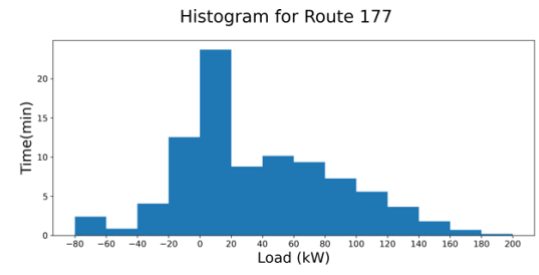
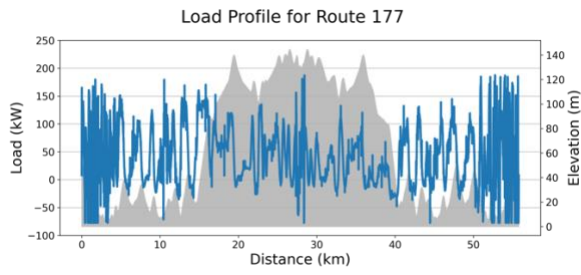
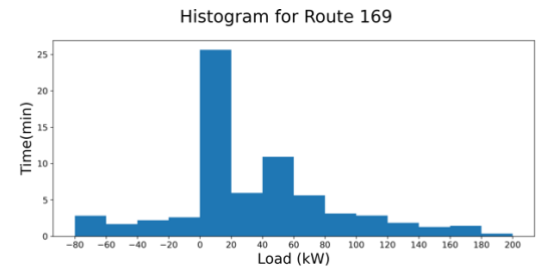
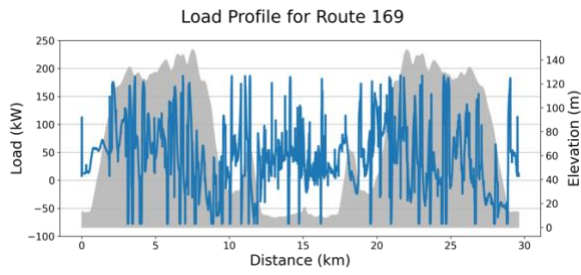
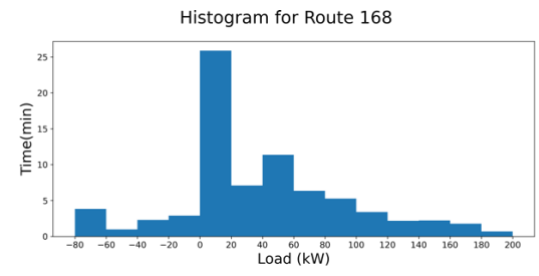
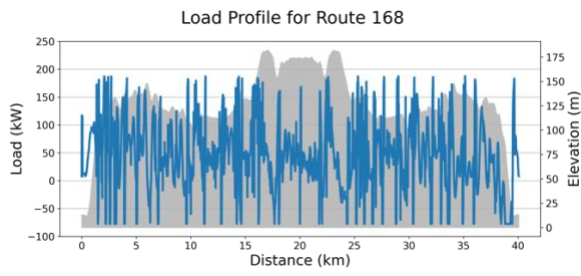
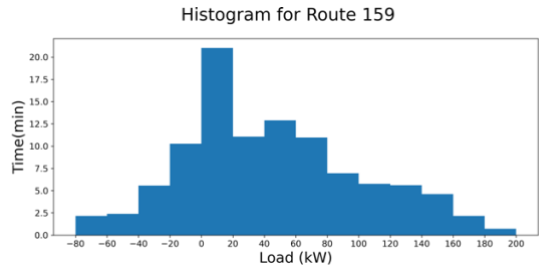
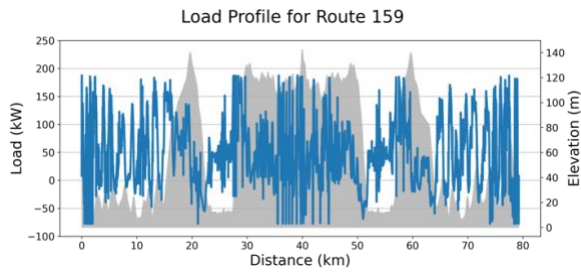
To improve the accuracy of this calculation, more real-world data could be used. For example, studies have shown that the auxiliary demand has a significant effect on load and energy demands, so more accurate auxiliary load profiles should be studied ⁶². One possible proxy is to include temperature data. Temperature can help estimate when the HVAC system is in use. In the future, temperature is another valuable input for estimating battery degradation.

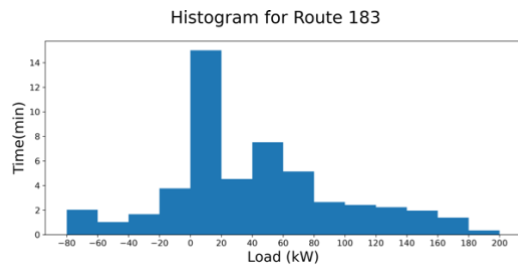
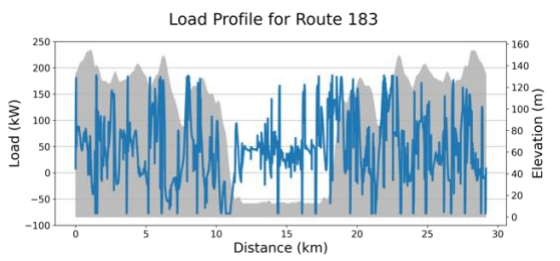
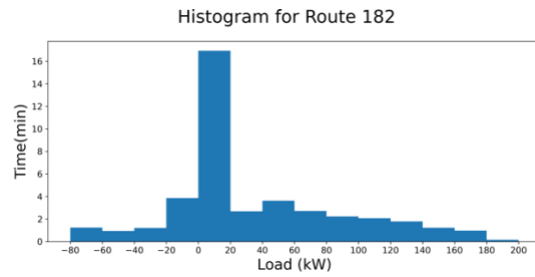
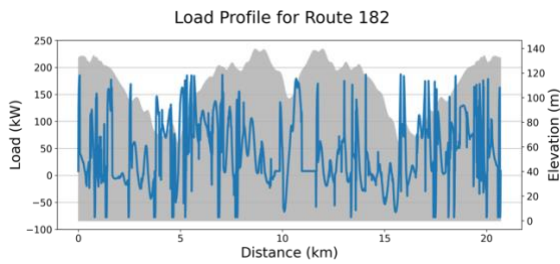
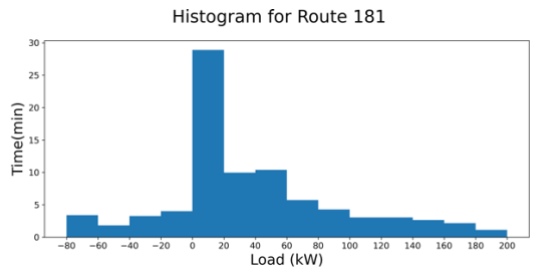
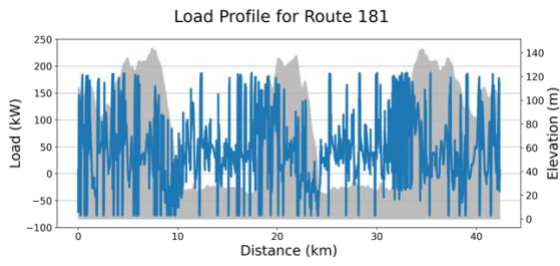
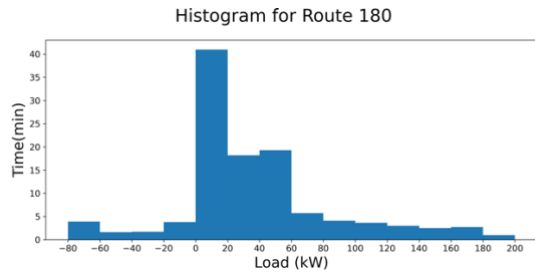
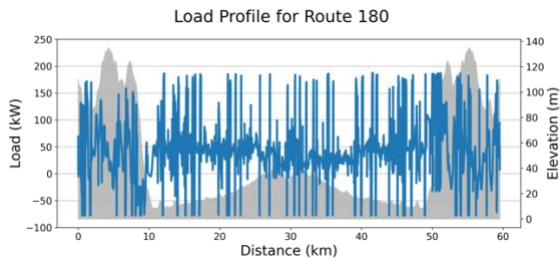
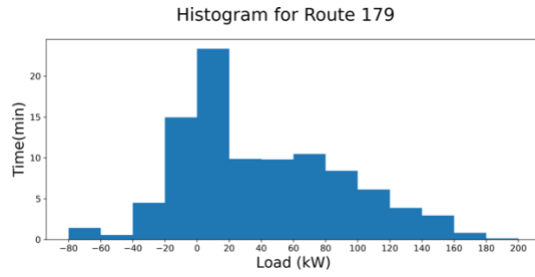
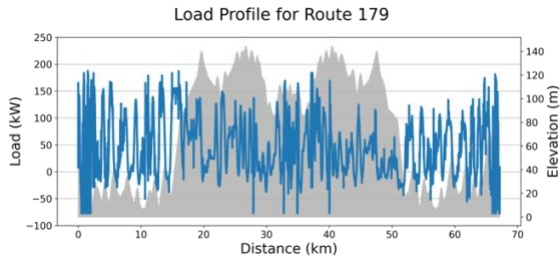
A future goal of the route_dynamics software is to model battery degradation using the load and energy profiles. First, the time-series power result will be transformed into time-series voltage data. This information will be used to estimate the current/C-rate and SOC, both of which are significant parameters in degradation models.

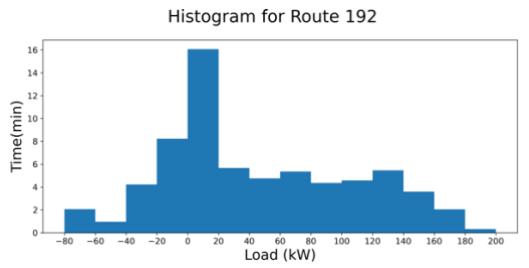
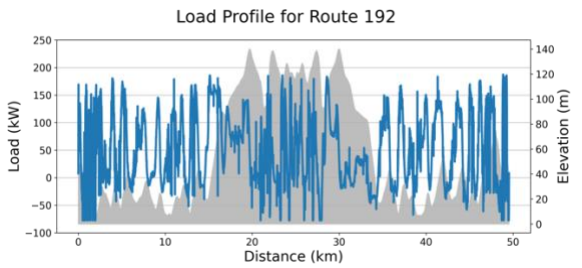
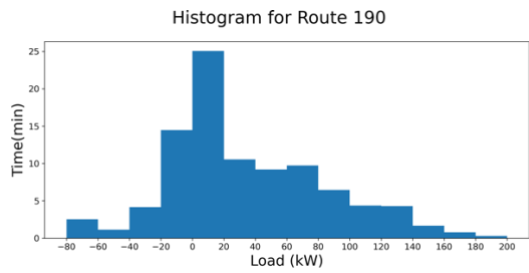
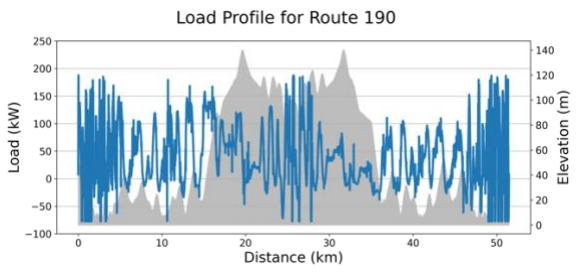
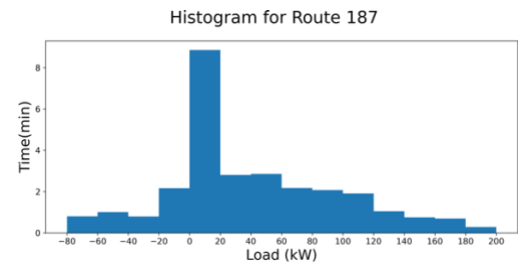
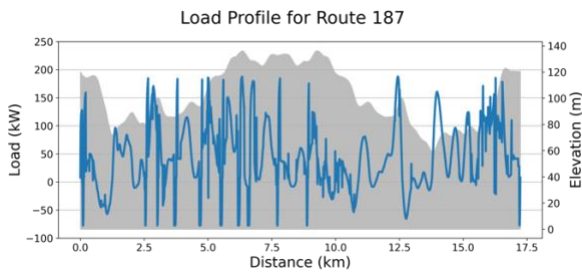
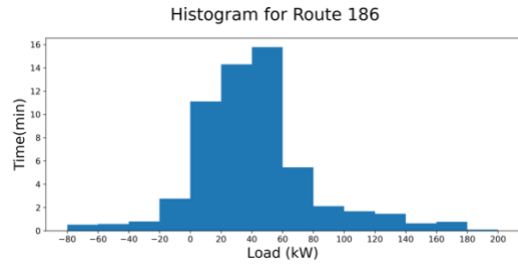
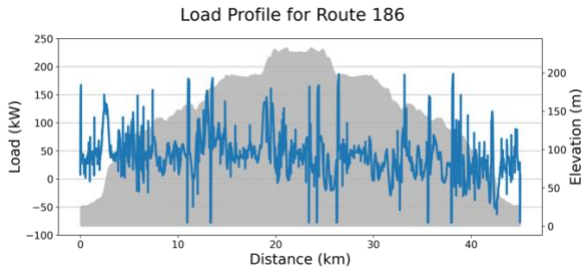
2.5 Appendix – Full Results











Chapter 3 - Multi-scale Integration of Computed Battery Electric Bus Fleet Drive Cycles with Cell Testing and State Estimation from Simple Battery Management Models

Note – this chapter is in preparation to be published as a journal article

3.1 Introduction

In the first research objective, we were able to estimate loads expected for electric busses in the King County Metro fleet. While this is useful for more qualitative route analysis, this objective strives to relate the outputs of vehicle-dynamics models cell-level voltage and current profiles. Once the voltage and current are known, they can be used for physics-based battery models, such as those used for PyBamm^{34,35} or thermodynamics models⁸¹. Models at this level can help identify unknown degradation mechanisms, improve battery life by adjusting operating conditions, and improving life by adjusting materials as needed ⁸²

In this work, we demonstrate a multiscale strategy for integrating longitudinal drive cycle loads for a BEB operating on King County Metro routes with a simple reduction of order from pack-to-cell that permits drive cycle testing and state estimation for fresh and aged cells via simple equivalent circuit models to emulate BMS outputs.⁸³ For example, BMS data from the New Flyer Hybrid-Electric buses would collect voltage data every second for each sub-module within a pack and store the values into bins of 0.2 V ranges, such as in Figure 3.1. After the sub-module had spent too much time in the high or low voltage bins, the maintenance crew would be notified that the module should be replaced.

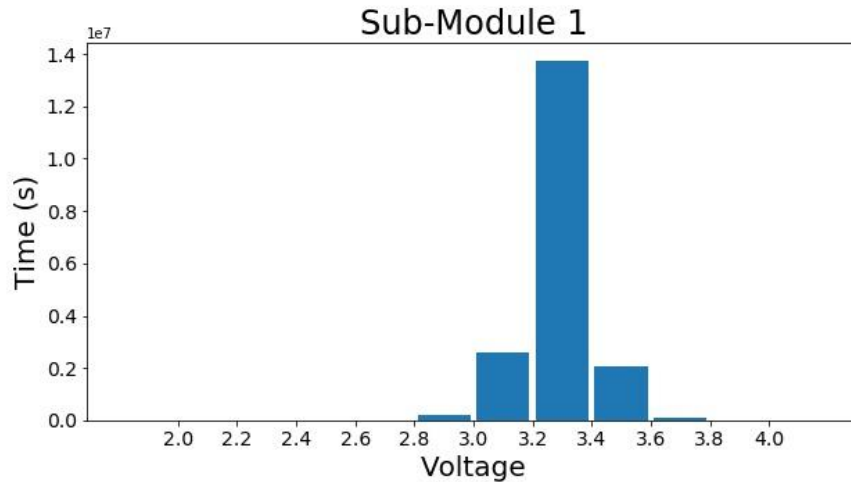


Figure 3.1: Example of a voltage histogram from a New-Flyer hybrid-electric bus battery management system

3.2 Methodology

The cells used were from a comprehensive cell cycling study, funded by the Joint Center for Deployment and Research of Earth Abundant Materials (JCDREAM). Details of that dataset and cycling conditions can be found in Chapter 4. Two-factor tests were evaluated for three variables: fresh vs. cycle-aged cells, high vs. low state-of-charge (SOC), and route difficulty as measured by high load variance vs. low load variance. Fresh cells had been cycled 300 times prior to this experiment. The aged cells had been cycled 900 times aggressively. Half of the cells were cycled starting at a SOC of 100%, while others started at 30% SOC. Lastly, half of the cells were cycled using the load profile of a high power or a “high extreme” route, whereas the other half experienced a “low extreme” route. Routes were selected using the Load Distribution histograms, like those shown in Chapter 2. High extreme routes spent more time in the tails of the load distribution, i.e. maximum motor power for acceleration and maximum regenerative braking power associated with a hilly urban drive cycle in Seattle. In contrast, low extreme routes spend most of their time at modest power draws, associated with low grade rural routes with few stops. A summary of conditions is given in the experimental matrix shown below:

Table 3.1: Experimental matrix for cell-level drive-cycle testing

	High SOC		Low SOC	
<i>Fresh</i>	Profile: High Extreme (Route 22) Cell 13	Profile: Low Extreme (Route 186) Cell 14	Profile: High Extreme (Route 22) Cell 15	Profile: Low Extreme (Route 186) Cell 16
<i>Aged</i>	Profile: High Extreme (Route 22) Cell 17	Profile: Low Extreme (Route 186) Cell 18	Profile: High Extreme (Route 22) Cell 19	Profile: Low Extreme (Route 186) Cell 20

3.2.1 Cell-Level Drive Cycles

The pack-level loads determined from drive cycles from Chapter 2 were transformed into cell-level dynamic loads, as described here. Based on BEB manufacturer information, we assumed that the batteries on-board were NMC in a New Flyer 40' bus with standard BESS energy options of 160 kWh, 213 kWh, 267 kWh or 320 kWh. Because many of the routes studied in Chapter 2 are longer range, we assume that our bus of interest has a 320 kWh BESS. The putative 40' New Flyer bus is likely to be supplied with a NMC pack using XALT Energy modules with large format cells⁴⁸, but here we are using the same commercial Samsung INR1850-15 M cells used in Chapter 4. The Samsung cells have an energy capacity of 5.4 Wh, so 59,260 cells would be needed to meet the energy specification.

For the load profiles of interest, the total profile load is divided by 59,260 cells, with no overhead for pack balancing to accommodate cell-module-to-pack variation. Load profiles for individual cells for Route 22 and Route 186 are shown below in Figure 3.2, where positive current denotes cell discharge and negative current represents charging from regenerative braking.

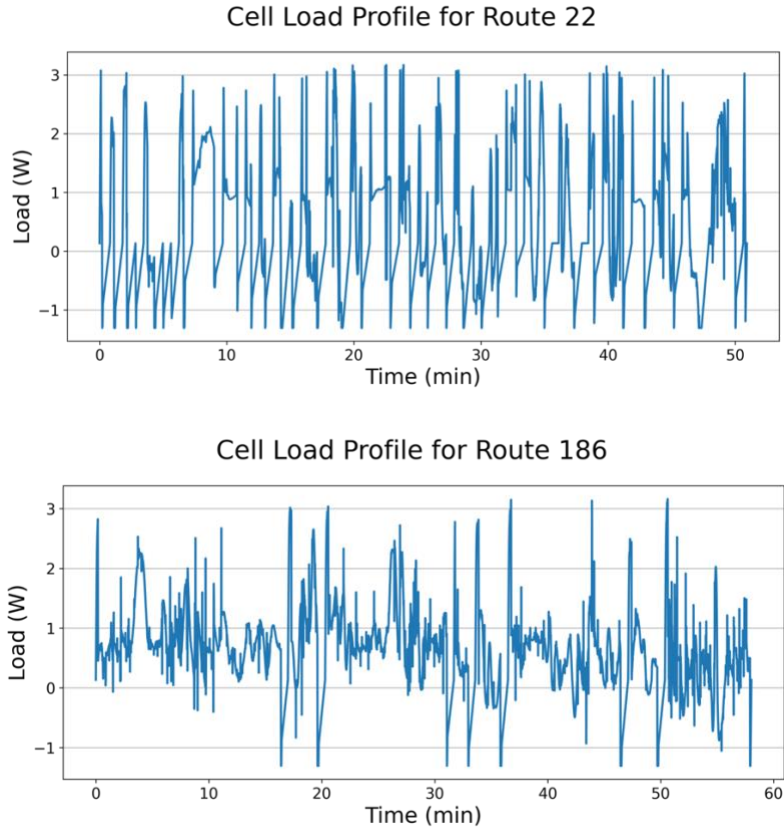


Figure 3.2: (top) Cell-level drive-cycle for route 22. (bottom) Cell-level drive cycle for route 186.

3.2.2 Cycling and EIS Measurement Protocols

The cells were cycled using a Maccor 4000M 96-channel cycler in a Maccor MTC-020 environment chamber set to 25°C. For each experimental condition, the cells were charged to the desired SOC (100% or 30%), then a Fastwave waveform was applied that charged/discharged the cells using the load profiles determined above. The waveform was applied twice, so each cell completed the desired round-trip two times. Cells were monitored to make sure that they were staying within the safety voltage limits provided by the supplier, or between 2.5 – 4.2 volts. If the cells went beyond that range, the tests were stopped.

Electrochemical impedance spectroscopy (EIS) measurements were taken for each cell after cycling, so that they could be compared with measurements taken previously. EIS measurements were taken using the Ametek VersaSTAT 4 potentiostat. The cells were charged to 3.5 V or 10% SOC. A 1 mV AC modulation was applied with a frequency sweep from 10 kHz to 10 mHz.

3.2.3 Cell-Level Model

We used a simple cell-level battery model with internal resistance and the open-circuit voltage to represent dynamic voltage changes during charge and discharge loads. This is a simple but reasonable first approximation for small deviations from equilibrium, where individual route charge/discharge events lead to a relatively small change in state of charge. The model is represented by the equivalent circuit model shown below, where a resistor is in series with a controlled voltage source, and both component values are a function of state of charge.

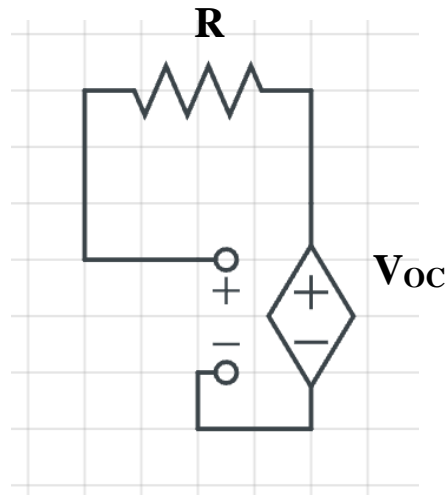


Figure 3.3: Diagram for equivalent-circuit representation for the simplified battery model, where a resistor is in series with a SOC-dependent voltage source.

A constant resistance cell voltage can be represented as:

$$(1) \quad V = V_{oc} - R * I .$$

However, a cell's apparent resistance, R , is a state of charge dependent parameter that, along with the SOC-dependent open circuit voltage can be used to match experimentally-measured battery test data. Therefore, we calibrate R and V_{oc} as “effective” fitting parameters while the cell is being tested under the dynamic load for a route from Route Dynamics results, where we experimentally measure voltages and currents for each time point, i , along the route. Experimental data for load, cell current, and cell voltage at point i is modelled through the simple algebraic equation:

$$(2) \quad L_{cell,i} = V_{oc,eff} * I_i - R_{eff} I_i^2$$

Where L_{cell} is the load that was estimated by Route_Dynamics and input into the Maccor cycling protocol as a waveform. Because the cell has a SOC-dependent open circuit voltage and resistance. This equation can be solved to find the calculated current at route location, i :

$$(3) \quad I_i = \frac{V_{oc,eff} - V_{oc,eff} \left(1 - \frac{4R_{eff}L_{cell,i}}{V_{oc,eff}^2} \right)^{1/2}}{2R_i}$$

And the calculated voltage at route time i :

$$(4) \quad V_i = \frac{V_{oc,eff}}{2} \left(1 + \left(1 - \frac{4R_iL_{cell,i}}{V_{oc,eff}^2} \right)^{1/2} \right)$$

To calibrate the equations and estimate the values for $V_{oc,eff}$ and R_{eff} during operation, we fit the dynamic experiment data every 2-4 min or 120-240 seconds using the `scipy.optimize.fmin_slsqp` function, where the sum-squared error for current and voltage calculations compared to experimental values was minimized. The SLSQP solver uses Sequential Least Squares Programming, or a nonlinear least-squares solver to minimize the objective function. Bounds were set to keep the parameter results within the voltage safety limit (2.5 – 4.2 V)

This off-line state estimation is effectively a calibration method that permits us to evaluate the values for $V_{oc,eff}$ and R_{eff} in fresh and aged cells, at different SOC, and then use average values for the estimated parameters to predict voltage and current for any route, using the load profiles from Route_Dynamics.

Because we had EIS data for these cells from previous experiments, and because EIS data was taken as part of this protocol, the R_{eff} values calculated here were compared to the impedance magnitude of a similar cell.

3.3 Results and Discussion

Here we discuss some of the features of the simple cell-level model results when Samsung 18650 NMC|C cells are subjected to a vehicle drive cycle from Route Dynamics. First of note, cell 14 did not complete the study, because it short-circuited during experimental set-up. All other conditions were tested. However, low SOC Cells 16 and 20 did not complete their second round-trip drive cycle, because the cell voltage dropped below 2.5 V, and the test was stopped.

The first cell (Cell 13) starts near 100% state of charge (SOC) and is closer to beginning of life, as it has experienced 300 cycles before this test. This cell also experiences loads predicted for Route 22, a short urban route that has many stops. This route is classified as the high-extreme, as it spends a significant amount of time in the upper and lower load limits. Figure 3a shows the experimentally measured current from the input load. In this case, a positive current denotes discharge and a negative current denotes charging from regenerative braking. This cell had a roughly 2.5% net decrease in state of charge, when completing the route twice in a row. Plot 3b shows the experimentally measured voltage over time, along with the estimated open-circuit potential estimates, and 3c shows the estimated resistance. The model parameters were optimized and fit every 240 seconds, for this case. The average resistance is 36 mOhm, which is appropriate for capturing the dynamics for a fresh Samsung cell operating at a high SOC.

We then use the estimated $V_{oc,eff}$ and R_{eff} parameters to calculate the voltage and current values. Figure 4 shows a parity plot of measured and modeled voltage that lets us evaluate the quality of the simple model. The plot shows that this model, with parameter estimation every four minutes, captures around 85% of the experimental variance, with a mean absolute error of 3.9 mV. Not shown, is that this model captures 99% of the experimental variance measured in current. Because of the narrow voltage window (both experimental and measured) and since applied power is known, it is unsurprising that there is little uncertainty with respect to current. Given the simplicity of the cell model and complexity of a drive cycle, we

deem this approach reasonable as a first-order approximation of the dynamic voltages a cell experiences in a bus drive cycle.

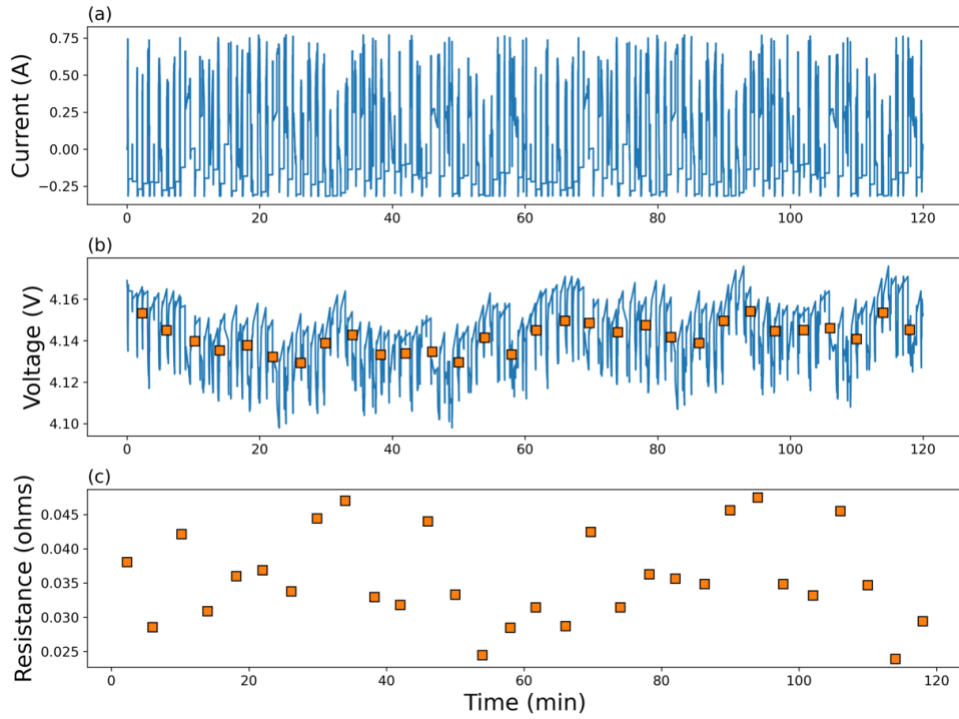


Figure 3.4: The measured current profile (a), measured voltage profile with open-circuit voltage estimates, and (c) resistance estimates for Cell 13, a fresh, high-SOC cell on a high extreme route

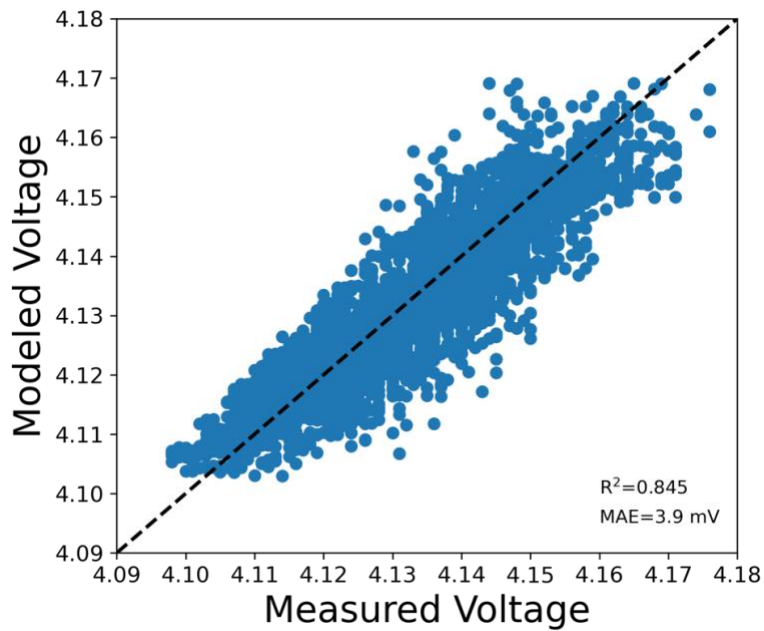


Figure 3.5: Parity plot for Cell 13, comparing the measured and modeled voltage values.

At the opposite extreme, we will show similar analysis for Cell 20, an aged cell at low SOC and experiencing loads associated with a rural route (Route 186) that has fewer stops and higher roadway speeds. The SOC dropped around 5% before reaching the safety cut-off voltage of 2.5 volts. Not only is this change in SOC twice as much as in Cell 13, but it occurs over one-sixth of the time. This is, in part, because this route had significantly fewer opportunities to charge from regenerative braking. Moreover, the higher cell voltage of a high SOC battery results in less charge extraction for a given route energy demand. This also causes the voltage window, measured and modeled, to be much wider. The average resistance for this cell was around 0.19 ohms. The parity plot shown in Figure 6 shows that the model captures experimental variance well until around 3 V. This is to be expected, since Figure 5b shows that the voltage starts to decrease quickly after 3 V. Because this cell had a much lower total experiment time, parameters were fit every two minutes.

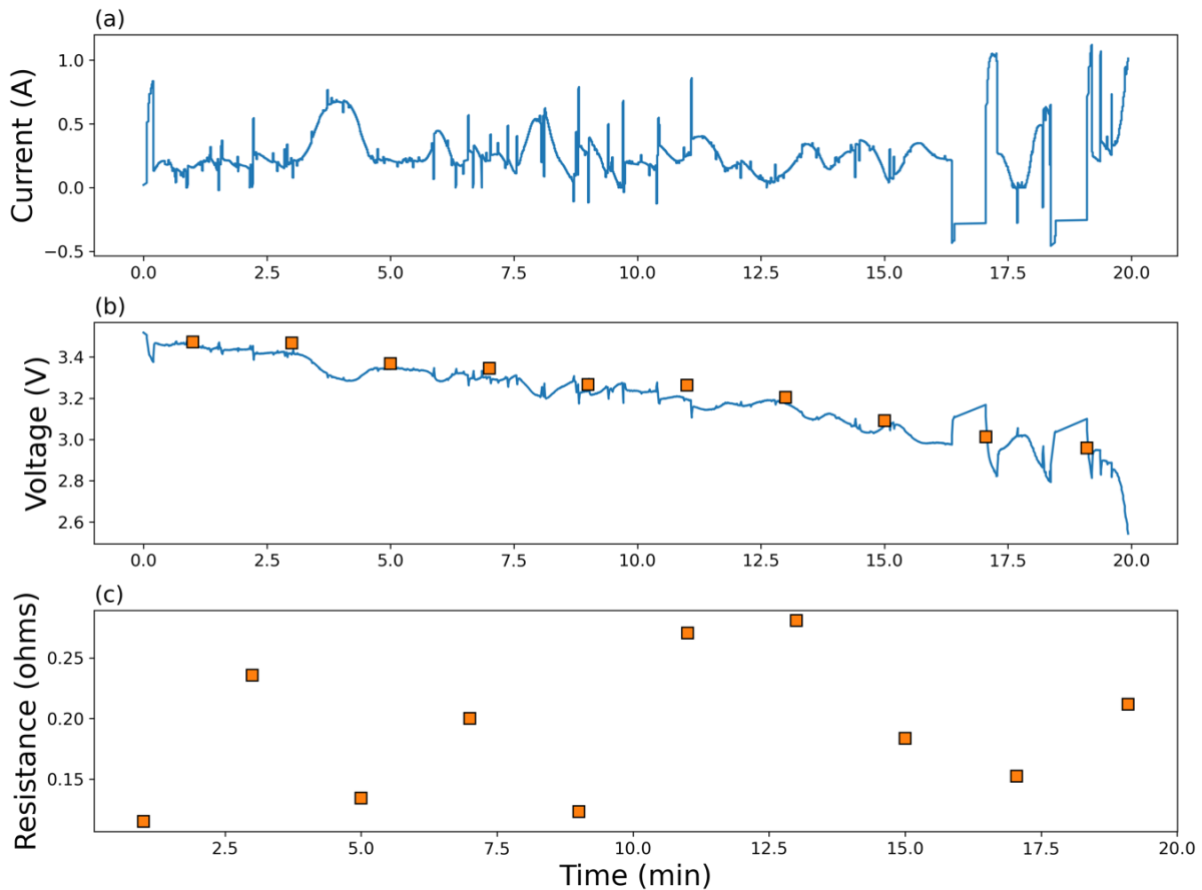


Figure 3.6: The measured current profile (a), measured voltage profile with open-circuit voltage estimates, and (c) resistance estimates for Cell 20, an aged, low-SOC cell on a high extreme route

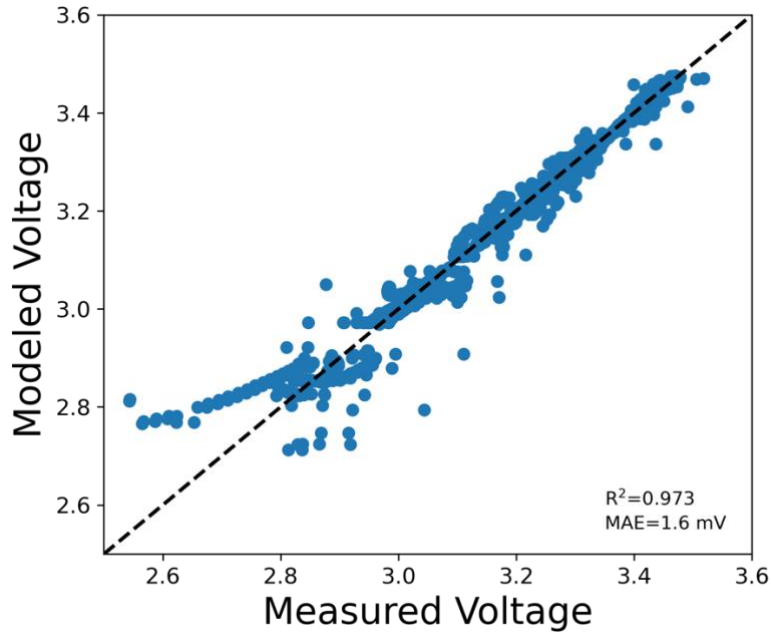


Figure 3.7: Parity plot for Cell 20, comparing the measured and modeled voltage values.

Because Cell 20 did not complete the first trip drive cycle, lets also compare the results for Cell 16, which also experienced route 186 at a low SOC, but as a fresh cell.

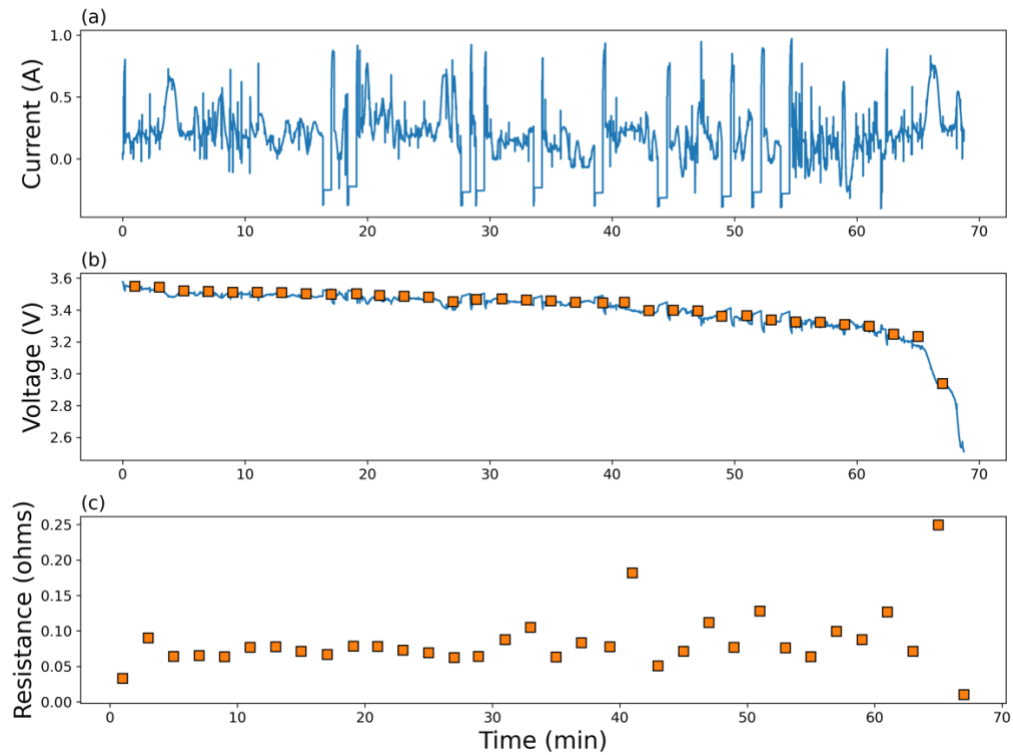


Figure 3.8: The measured current profile (a), measured voltage profile with open-circuit voltage estimates, and (c) resistance estimates for Cell 16, a fresh, low-SOC cell on a high extreme route

Similar to Cell 20, there is a significant decrease in measured voltage once the cell is discharged to approximately 3 V. In this case, a decrease in open-circuit voltage is also noticeable. The parity plot also shows that the model does not capture experimental variance well below 3 V.

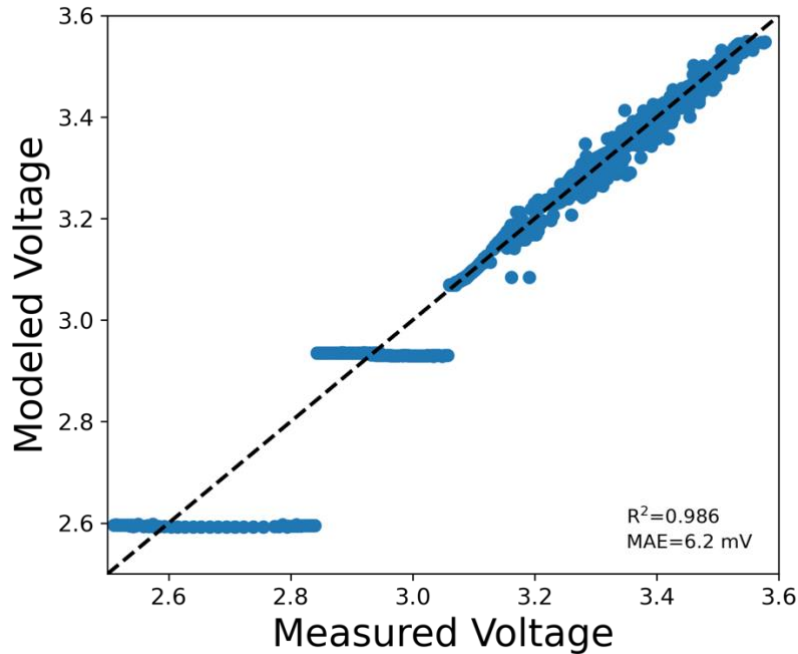


Figure 3.9: Parity plot for Cell 16, comparing the measured and modeled voltage values.

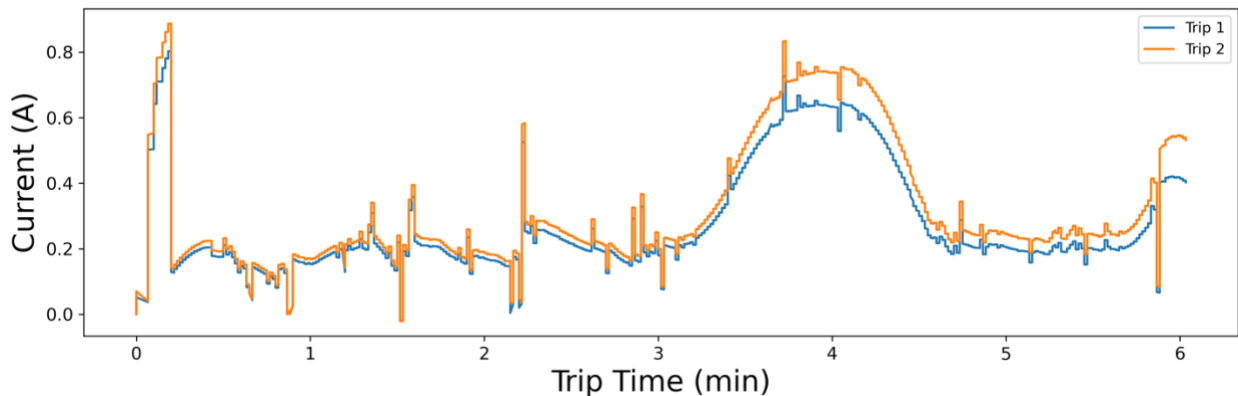


Figure 3.10: Comparison of current profile for a six minute segment of first and second trip for Cell 16.

When we compare the six minutes of the second trip that was completed to the first six minutes of the first trip, we see that a higher current is needed to maintain the same load demand. This is because the cell voltage is quickly dropping. On average, there is a 16% increase in current required at this lower voltage, and hence 16% more charge extracted to cover the same

portion of the route. In comparison, the first six minutes of the two trips for Cell 13, the fresh, high SOC cell had a less than 0.1% increase in average current and charge extraction because the cell voltage changed only modestly.

The current and voltage profiles, parameter estimation results and parity plots for the other cells can be found in the Appendix

Estimating Voltage and Current for a New Route

The estimated open-circuit voltage and resistance values from Cell 13 were then used to calculate the voltage and current profiles for a different route, with similar conditions. Cell 13 was chosen, because the change in parameters with respect to SOC was low, so for a similar route it would be a decent assumption that $V_{oc,eff}$ and R_{eff} are constant. We used Route 101 for this example, because it had similar time spent in the high and load limits, similar to Route 22. We assumed for this scenario that the cell also started fully charged at 100% SOC. Results from this calculation are shown below. This is meant to be an example of how calibrating the model with a sample dataset allows us to gain similar information as an on-board BMS.

Voltage and Current Profile for Route 101

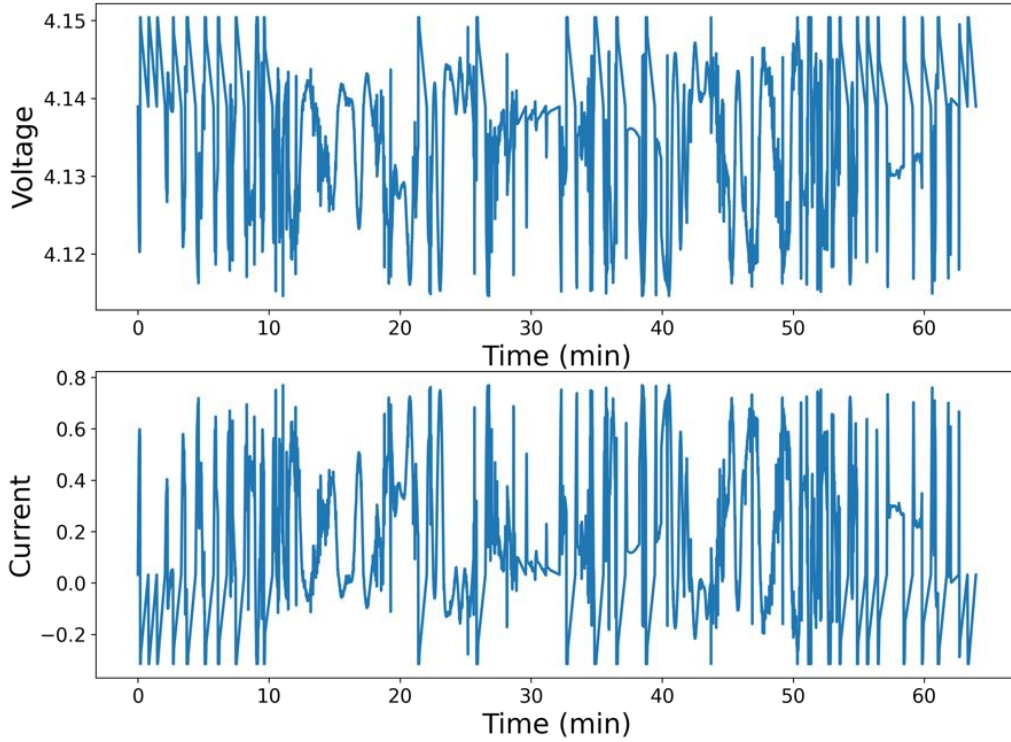


Figure 3.11: Voltage and current profile estimated for route 101, using the values for open-circuit voltage and resistance calibrated from Cell 13.

Voltage Distribution for Route 101

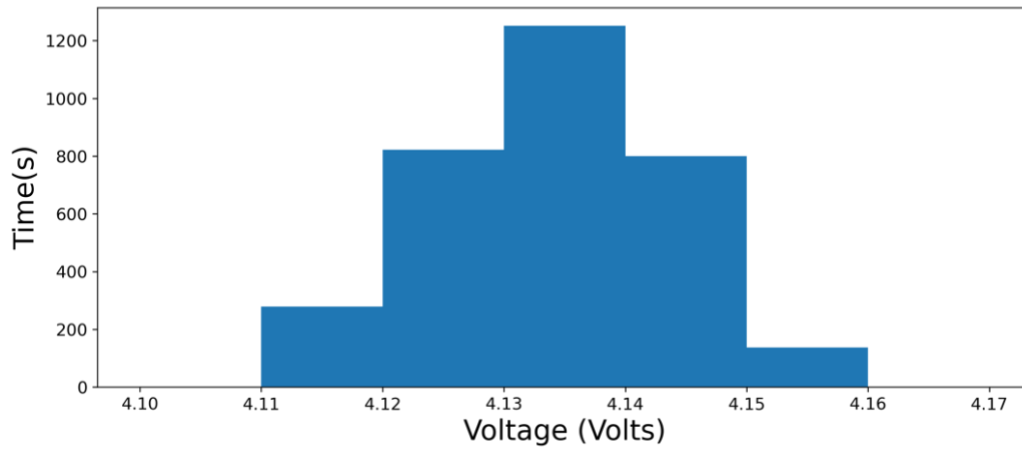


Figure 3.12: Voltage distribution for route 101, using the conditions from Cell 13.

Checking Resistance Estimation with EIS

Out of all of the cells tested, only Cell 15 had the least noise from the instrumentation. Therefore, we used this cell had our comparison between the simple model resistance estimate and the fit resistance values. The python package `impedance.py` was used to fit the Nyquist plot for Cell 15. The combined charge transfer and contact resistance for this fit was 0.06 ohms, which is close to the resistance estimate from the simple model of median value of 0.059 ohms.

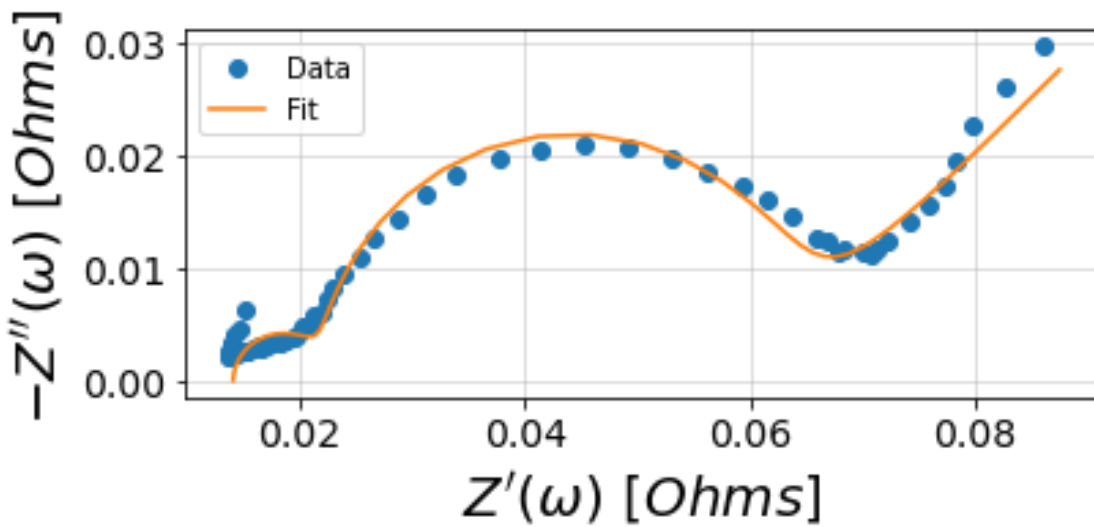


Figure 3.13: Nyquist plot for Cell 15 with a fit found using `impedance.py`.

3.4 Conclusions

In this study we were able to translate load profile results from the Route Dynamics software to create cell-level charge/discharge protocols. The experimental results then allowed us to fit a simple BMS-style battery model to find values for the open-circuit voltage and resistance parameters. By being able to replicate battery management system voltage bins off-line, we can predict which bus routes will reach voltage cut-offs sooner and the battery modules on-board would need to be replaced.

In aggregate, these studies show how route features, model-based BMS estimation, and R_{eff} and $V_{OC,eff}$ are linked to state of charge estimation and state of health estimation. In particular, high quality $V_{OC,eff}$ estimation is key for determining SOC in near real-time. With our simple BMS model, failure at low SOC leads to a common occurrence, namely, inaccurate estimates for remaining charge in the battery. In contrast, even our simple BMS model provides a strong signature for state of health. Specifically, estimates for R_{eff} are significantly higher for the more aged cell than the fresher cell, at every state of charge. Simple cell resistance metrics are well known predictors for remaining useable life in a Li-ion cell²⁷. So, despite the simplicity of the cell model, we were able to link route simulation, test, and BMS-type estimation to a wide range of physical processes at scales that range from the miles of a route and grade of a roadway, to the degradation of molecules in a battery that indicates end of a cell life.

3.5 Appendix

Cell 15: Fresh, Low SOC, Route 22 (High Extreme)

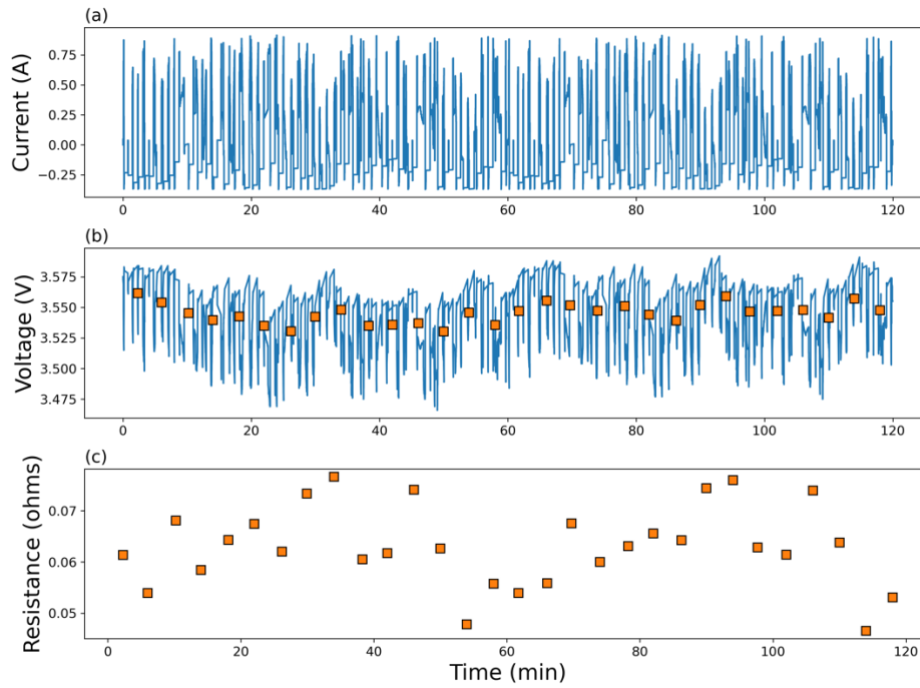


Figure 3.14: Measured voltage a current profiles for Cell 15, a fresh, low-SOC cell on a high-extreme route.

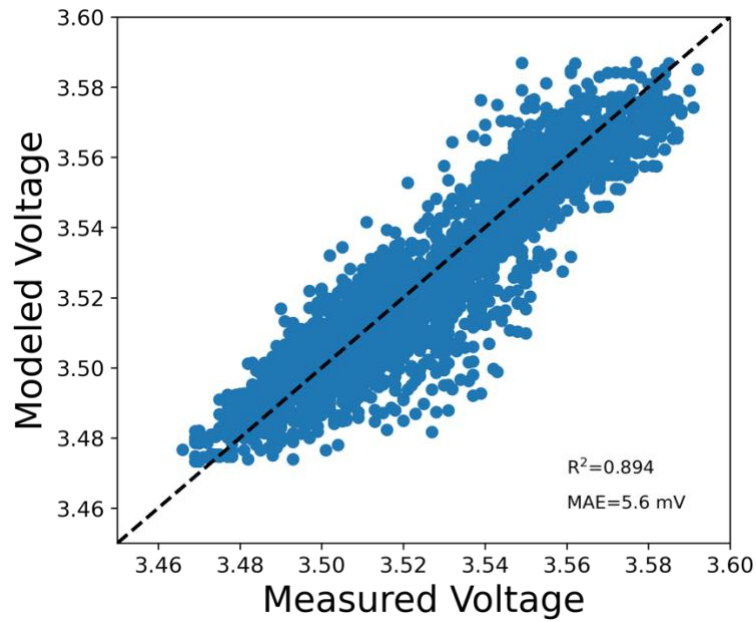


Figure 3.15: Parity plot for Cell 15, comparing measured and modeled voltage value

Cell 17: Aged, High SOC, Rt 22 (High Extreme)

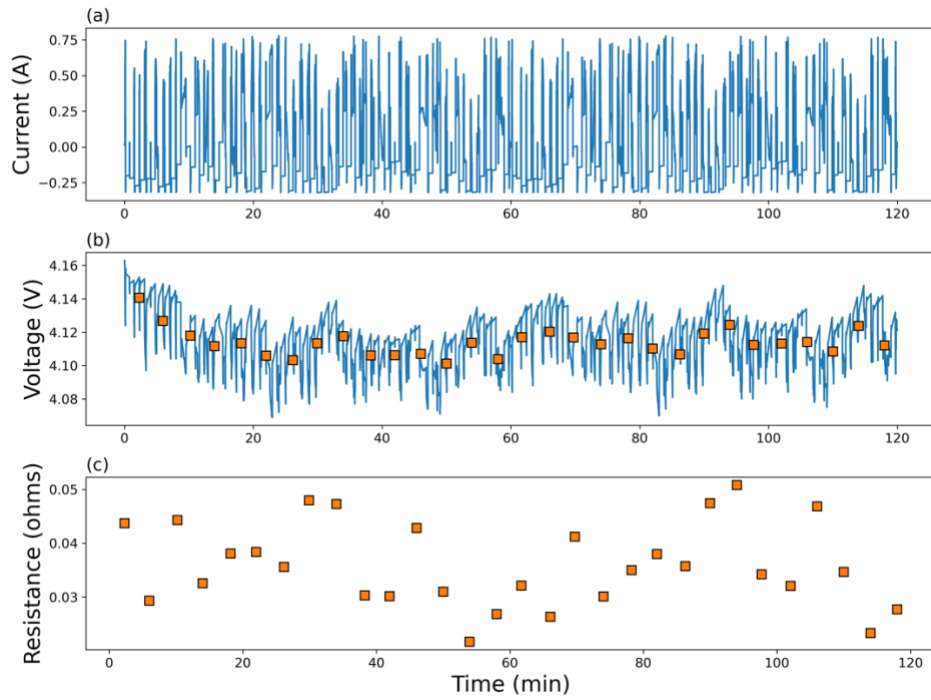


Figure 3.16: Experimentally measured voltage and current profiles for Cell 17, an aged, high-SOC cell on an high-extreme route.

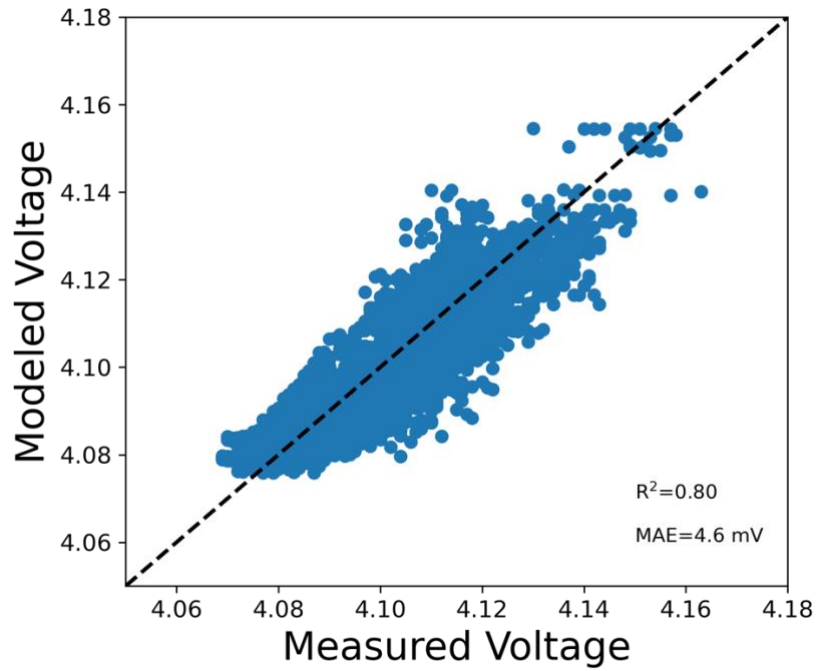


Figure 3.17: Parity plot for Cell 17, comparing measured and modeled voltage values.

Cell 18: Aged, High SOC, Rt 186 (Low Extreme)

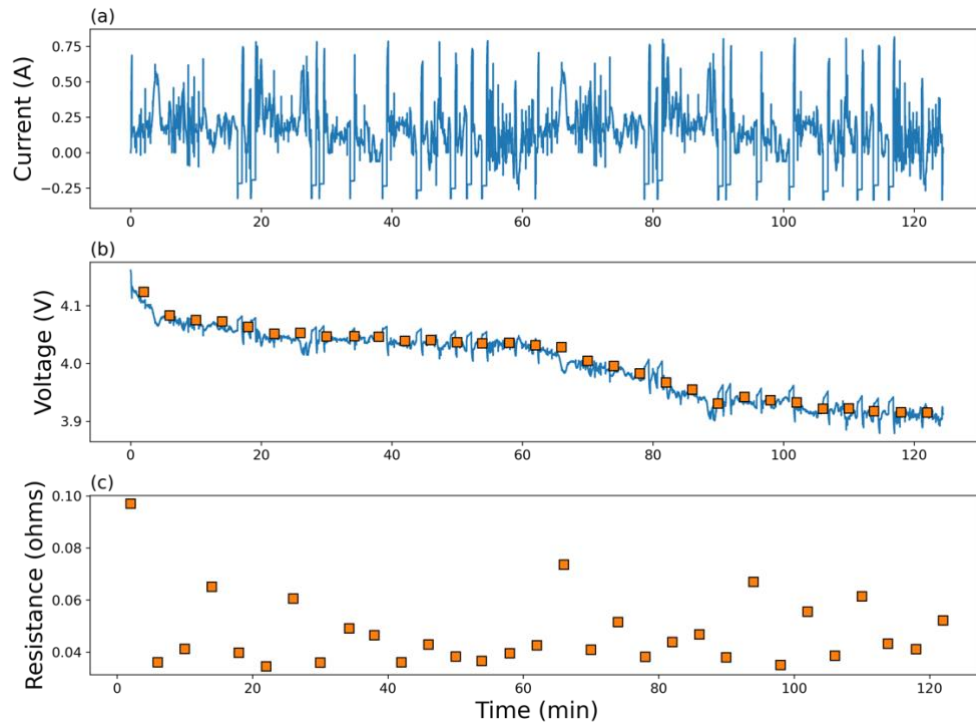


Figure 3.18: Experimentally measured voltage and current profiles for Cell 18, an aged, high-SOC cell on a low-extreme route.

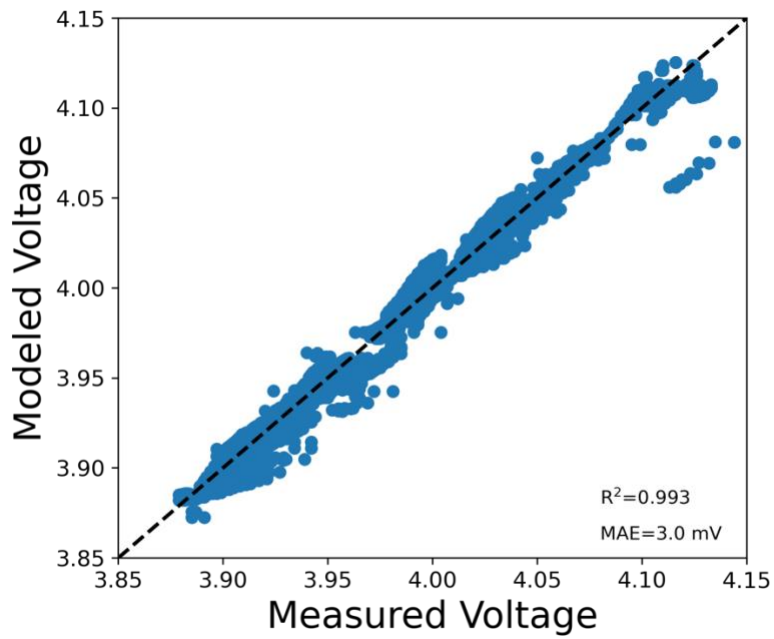


Figure 3.19: Parity plot for Cell 18, comparing modeled and measured voltage values.

Cell 19: Aged, Low SOC, Rt 22 (High Extreme)

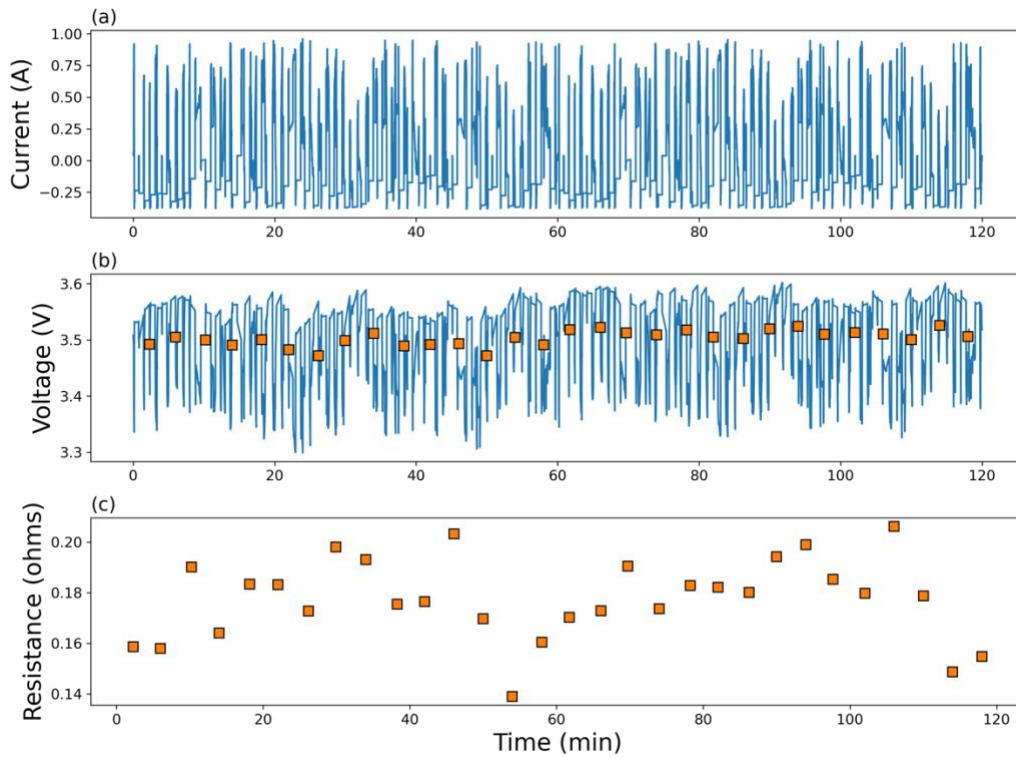


Figure 3.20: Experimentally measured voltage and current profiles for Cell 19, an aged, low-SOC cell with a high-extreme route.

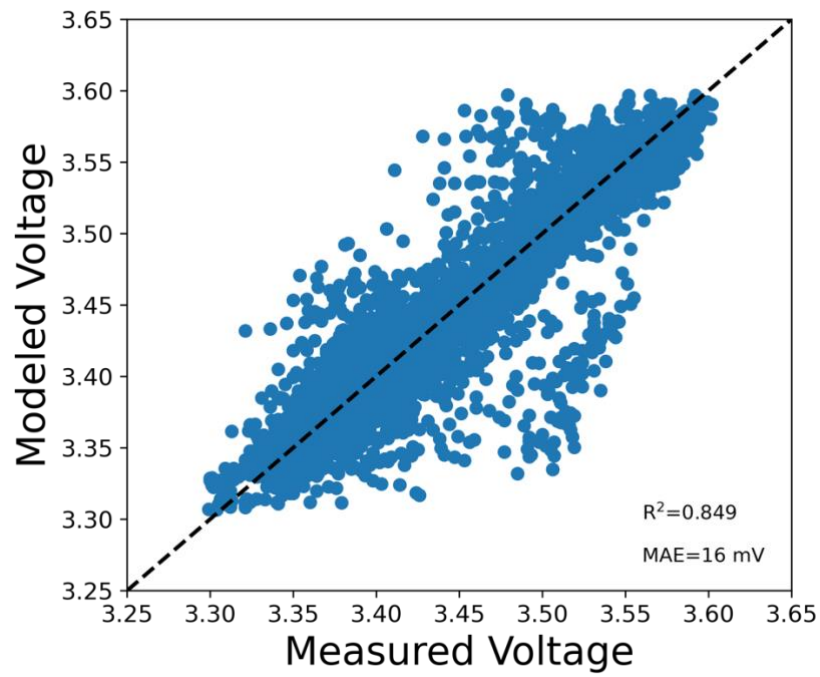


Figure 3.21: Parity plot for cell 19, comparing modeled and measured voltage values

Chapter 4 - Establishing a Framework for an Open-Source Battery Database

Note - This chapter contains content that is featured in one article on arXiv and one article in progress:

- Logan Ward, Susan Babinec, Eric J. Dufek, David A. Howey, Venkatasubramanian Viswanathan, Muratahan Aykol, David A.C. Beck, Ben Blaiszik, Bor-Rong Chen, George Crabtree, Valerio de Angelis, Philipp Dechent, Matthieu Dubarry, **Erica E. Eggleton**, Donal P. Finegan, Ian Foster, Chirranjeevi Gopal, Patrick Herring, Victor W. Hu, Noah H. Paulson, Yuliya Preger, Dirk Uwe Sauer, Kandler Smith, Seth Snyder, Shashank Sripad, Tanvir R. Tanim, Linnette Teo. Principles of the Battery Data Genome. *arXiv*, (2021), doi: <https://doi.org/10.48550/arXiv.2109.07278>
- **Erica E. Eggleton**[†], Victor W. Hu[†], Linnette Teo[†], Daniel T. Schwartz. Battery Corpus: An open-access dataset of commercially available lithium-ion NMC batteries exploring experimental variability in battery degradation. (in progress)

[†] *These authors contributed equally*

4.1 Motivation

There are numerous labs collecting battery cycling and experimental data, to try different materials, chemistries, configurations, and protocols.^{84–88} Some are also showing how field test data can be used.⁸⁹ However, this data is not often made public, besides as a figure in a publication or upon request, making it difficult for groups to try to reproduce, conduct their own analysis, or utilize for machine learning tools. Some groups, however, are realizing the value of publishing datasets from cell testing, and have started to do so using their own data formats and hosting techniques.^{39,90–93} This can make it difficult for other scientists to access data, especially depending on their skillset. Moreover, data quality metrics are rarely reported, nor are the metadata labels standardized for ease of reuse and reanalysis.

Open-source database tools, like Galvanalyzer, are being developed to manage battery data, but is not yet majorly adopted.³⁷ Commercial options include Voltaiq's battery data platform⁹⁴ and Astrolabe Analytics⁹⁵, but these systems focus on data management for specific projects, not necessarily community compilations. Meanwhile, in other fields, such as genomics, protein design, materials discovery, and remote sensing,⁹⁶⁻⁹⁹ exists meta data standards, repository structures, and open licensing that make data available, findable, and reusable. A team of experts in the battery community is making an effort to catch up to these other fields by creating a Battery Genome.⁴⁰

This work aims to contribute more cell cycling data to the community, focusing on commercial Samsung Li-NMC power cells. Nickel-Manganese-Cobalt (NMC) cathodes were chosen for this study because they have become more prominent due to their high energy density compared to Lithium-iron-phosphate, and increased chemical stability and reduced cobalt content compared to Lithium-cobalt-oxide.¹⁰⁰ Cobalt is a socially controversial and unsustainable element, due to inhumane mining practices. Therefore, there is an ongoing effort to minimize the use of cobalt in battery materials altogether.¹⁰¹

The dataset includes replicate cycling datasets and EIS measurements. Four replicates are tested, when possible, as opposed to the more common duplicate or triplicate study. Similar studies in the literature have shown that data replicates are crucial for credibility and reliability of experimental results and analysis.¹⁰²⁻¹⁰⁴ We propose some aggregated statistical metrics that can be used to understand the dataset quality and variability, while also identifying outlier cells and experiments that exist even in mass produced cells. The data is published using the Battery Genome Project proposed JSON metadata file structure and includes a supplementary Jupyter Notebook to demonstrate the analysis and figures presented here, and to allow further investigation and data visualization from the broader community. More information on metadata and schema structure can be found on the Battery Genome Project Github.

4.2 Example Dataset

4.2.1 Methods

4.2.1.1 Cycling Data

Commercially available Samsung 1.5 Ah Li NMC | C power cells (INR 18650-15M), all from the same manufacturers lot number, were used in all measurements. A total of 48 cells were used with a balance between replicate experiments and number of unique testing conditions, as summarized in the test matrix (Table 1). Two different charging C-rates (2.67C and 2.00C) and a common discharge rate were compared at two different environment temperatures (5°C and 25°C). The charging C-rates were chosen to accelerate testing and degradation, while staying within the 4A maximum charging rate recommended by the manufacture. The discharge rate for all cells was 3.00C. In short, all cells were subjected to fairly aggressive charge and discharge conditions. To glean information on the states-of-health (SOH) and reproducibility of cells operated under the four different conditions.

For each of the four unique test conditions, 12 cells were used, summing to 48 distinct cells that underwent cycling. To study the intermediate states-of-health (SOH) and probe the reproducibility of cells operated under each set of conditions, subsets of cells were cycled accordingly with the test matrix in Table 1. Diagnostics for cells cycled as shown in Table 1 included C/20 charge and discharge curves as well as electrochemical impedance spectroscopy (EIS) analysis at several different states-of-charge (SOC). An additional 4 fresh cells were used to collect open-circuit potential and impedance data at the beginning-of-life for this lot of cells. All of the 5°C experiments were completed using a Maccor 4000M 16-channel cycler in a Tenney TPS C-EVO Environment Testing Chamber and the 25°C were conducted with a Maccor 4000M 96-channel cycler in a Maccor MTC-020 environment chamber. Individual cell case temperature measurements were available only through the 96-channel cycler and thus these data are available on select cells for the 25°C datasets.

Before cycling, each cell was allowed to equilibrate to the controlled temperature for four hours. Then, they were subjected to five break-in cycles at C/2 charge and discharge rates over the

manufacturer recommended voltage range (2.5 V to 4.2 V). The cells were then cycled using one of the charging C-rate under study (2 or 2.67 C), and a 3C discharge rate, until they reached the target cycle number. The cells then underwent one more C/2 charge and discharge cycle for capacity comparisons with the beginning of life. The final measurement is the OCV estimation measurement, which is conducted with low constant-current (C/20) measurements on charge and discharge. Once cells reached their target cycle number and had OCV and EIS measurements (as detailed in next section), they were removed from further cycling experiments. Prior work from this same class of commercial cells showed that there was low cell-to-cell variability, but the extent of this variability has not been systematically characterized.¹⁰⁵

Table 4.1: Experimental matrix for JCDREAM dataset

C-Rate (charge)	Temp	300 Cycles	600 Cycles	900 Cycles	1000 cycles+
2.00 C	5°C	4	4		4
2.67 C	5°C	4	4		4
2.00 C	25°C	4		4	4
2.67 C	25°C	4	2	2	4

4.2.1.2 Electrochemical Impedance Spectroscopy (EIS)

Following the cycling experiments and the OCV measurements, EIS measurements were collected using an Autolab PG-STAT128N potentiostat/galvanostat with the frequency response analyzer module (Autolab FRA32). All measurements were collected at 25°C using a four-electrode configuration with voltage sensing at the cell terminals, regardless of the cell cycling temperature.

For each cell, a rest step of at least four hours helped ensure thermal equilibrium. EIS measurements were then collected at 3.5 V, 3.643 V, and 3.82 V, which correlate with 10%, 30%, and 50% state-of-charge (SOC) for fresh cells in this chemistry. Since all cells were fully discharged at the end of the cycling protocol, the cell under test was charged at a C/10 rate to the

desired voltage, where it would then enter a two-hour constant voltage charge step, before being allowed to rest for another two hours at open-circuit. Impedance measurements were made over a logarithmically spaced frequency range from 10 kHz to 5.01 mHz, with ten points per decade, using a minimum of five steady-periodic cycles, logged with 4096 data points.

4.2.1.3 Post-Processing, Validation, and Statistical Analysis

Due to inherent noise in the instrumentation, post-processing of the low-current (C/20) experiments was used to minimize noise in the differential information. We applied a third-order polynomial Savitzky-Golay filter with a window-length of 99 points across the entire dataset, where a center voltage is selected with 49 points before and 49 points after. The differential voltage (dV/dQ) is thus computed, where capacity, Q , is directly related to the charge/discharge current. The different capacity (dQ/dV) was calculated by taking the inverse.

An important validation technique for impedance measurements are the Kramers-Kronig relationships. Proper Kramers-Kronig relations ensure that the impedance measurement is stationary, time-invariant, and is representative of a causal system. Here, we use the validation toolkit from the open-source software `impedance.py`, which implements the Kramers-Kronig methodology by Schönleber et al ([link](#)). [Also reference the JOSS paper and LinKK paper]

To garner insight into experimental variability, statistical analysis was conducted for each measurement, at each condition for all replicate, following a common framework. First, the mean and the standard deviations are calculated at a consistent interval of the independent variable. Lower and upper limits of the envelopes of the 95% confidence intervals are calculated subtracting or adding two standard deviations to the mean value at that select interval, respectively. Relative standard deviations are also used in some of the later analysis and can be computed as the standard deviation/mean value times 100%.

4.2.2 Cycling Test Results

The 3C discharge capacity of all 48 cells cycled cells cycled between 4.2 V and 2.5V, under the four different experimental conditions, are shown in Figure 4.1 as a function of cycle number.

Cycles numbered 300, 600, and 900 are denoted by vertical dashed lines, since some cells were taken off-line at each of those cycle numbers for further EIS and low-rate C/20 testing. For each cycle number, the two standard deviations of true replicates (away from the mean capacity as shaded areas). The standard deviations are calculated based on the number of cells available at that cycle. The number of cells decreases as some cells are stopped at 300, 600, and 900 cycles according to our experimental matrix in Table 4.1. Note that some cells did not make it to 1500 cycles due to the experiments being stopped prematurely due to experiment time constraints. All of these cells were degraded well past 80% capacity, which is the standard definition of end-of-life.

For the two conditions at 25°C, the initial capacity for all cells are higher than that at 5°C. Also, at the higher temperature, the cells follow a linear degradative trend and the C-rate does not appear to have an effect on the capacity loss. For the cells cycled at the lower temperature, however, we see a steeper linear degradation trend initially, followed by nonlinear aging. There is also greater capacity loss at lower C-rates compared to at higher C-rates, probably due to heat generation at higher C-rates, and much larger cell-to-cell variability.

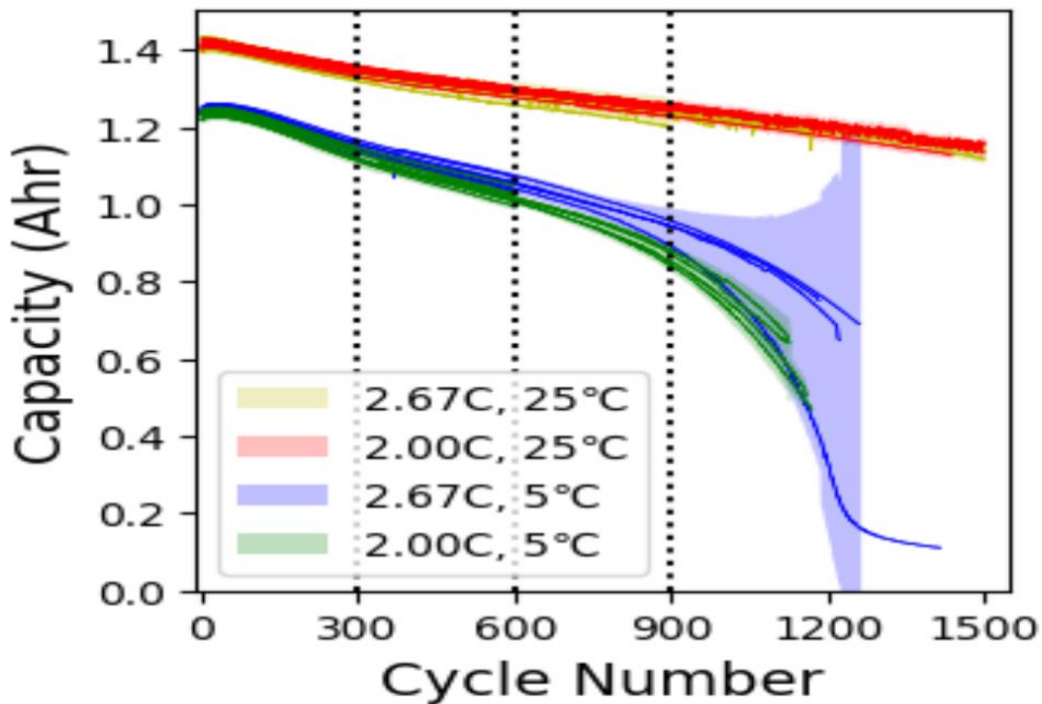


Figure 4.1: Capacity with cycles plot for all cycled cells under the four different experimental conditions Case 1: 2.67C, 25oC, Case 2: 2C, 25oC, Case 3: 2.67C, 5oC, and Case 4: 2C, 5oC. Shaded areas represent two standard deviations. For each condition, cells were cycled to either 300, 600, 900, or 1500 cycles, as noted by the dashed lines

For each experimental condition, we can examine the voltage curves at any cycle and also look at the variation within the replicate group of cells. For the experimental case, 2.67C and 25oC, there are eight cells that reach cycle 500. Figure 4.2 shows the mean of the charge and discharge voltages (normalized by capacity) of these eight cells at cycle 500. The two standard deviations calculated and shown as shaded areas are relatively small but there is still some variation in the voltage curves for these well manufactured commercial cells. This is an example of only one of the experimental conditions.

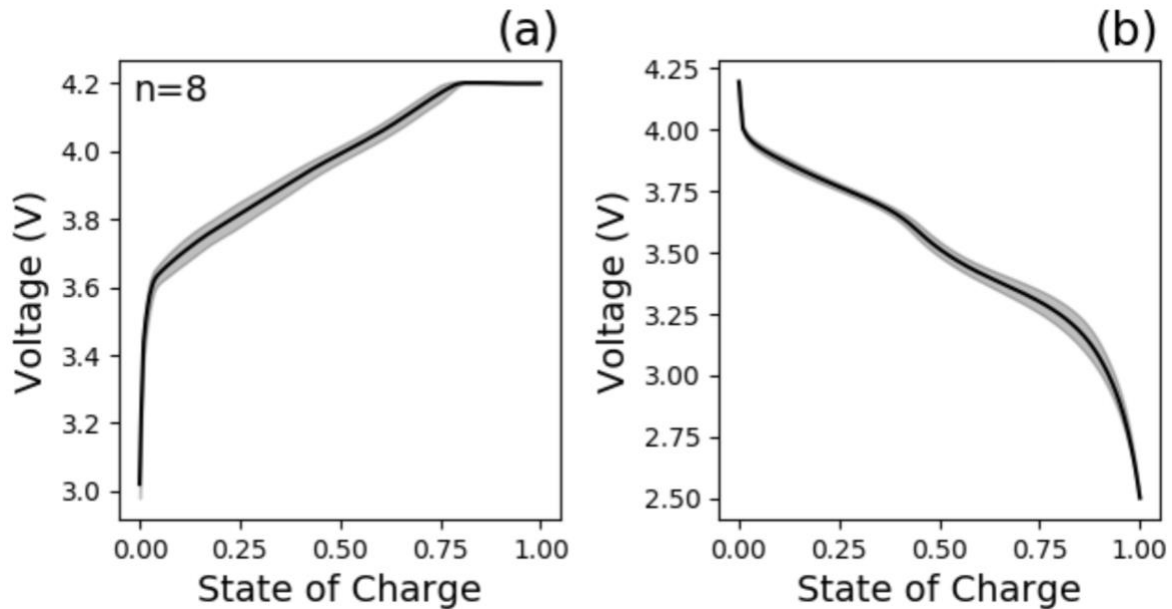


Figure 4.2: Mean values of (a) charge and (b) discharge voltage with SOC at cycle 500 for a replicate group of cells cycled under the 2.67C, 25oC condition. This replicate group consists of 8 cells and the shaded area represents two standard deviations.

A slow C/20 constant current charge and discharge was carried out at the end of cycling for each cell, and the resulting voltage curves can be taken to be the pseudo-OCV. Using the experimental case, 2C and 25oC, which has three replicate cells cycled to 1500 cycles, we show the mean values and two standard deviations for the charge and discharge curves of these three cells in Figure 4.3a and 4.3b. The corresponding differential capacity or dQ/dV plots can then be obtained using techniques described in the Methods section and similarly, the mean and standard deviations of the differential capacities for charge and discharge for these three cells are shown in Figure 4.3c and 4.3d. For the voltage curves, there is little variation in this replicate group of cells; however for the dQ/dV plots, we see larger standard deviations, especially in the regions around the peaks, which are highlighted by the vertical bands. This is because very small changes in the

voltages, when taking the derivative, can correspond to larger shifts in the peaks or changes in the width of the peaks. The peaks in the dQ/dV represent separate phase transitions and differences in materials composition, construction, and manufacturing can lead to slightly different peak heights and peak locations, leading to variability. Note that the second peak around 3.6V for the dQ/dV discharge in Figure 3d has especially noisy data with large variation, which we will explore later.

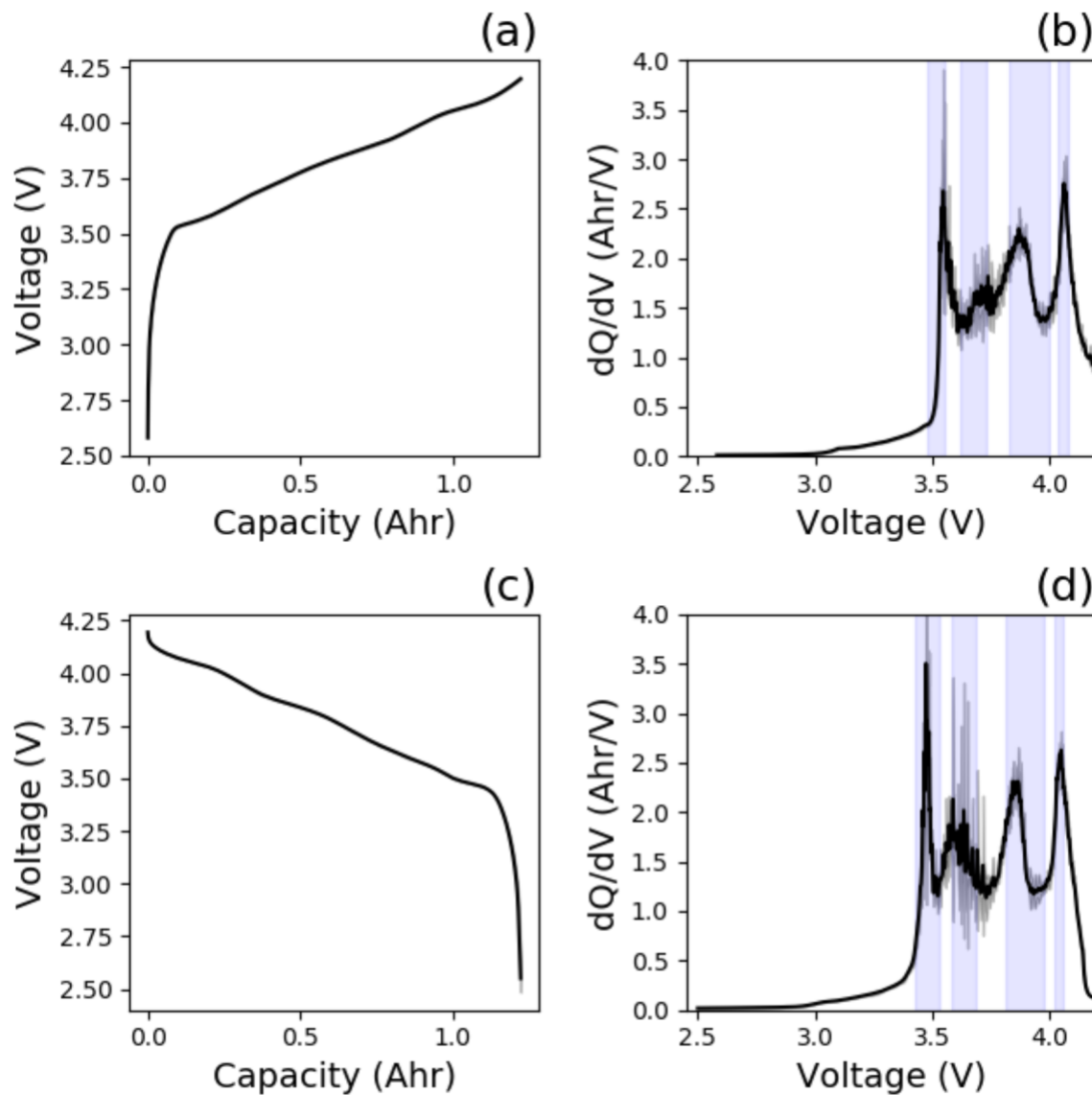


Figure 4.3: Mean values of end-of-testing C/20 constant current (a) charge and (b) discharge voltage curves with capacity for a replicate group of cells cycled under the 2C, 25°C condition. This group consists of cells 21, 22, and 23, which were all cycled for 1500 cycles. The corresponding mean values of dQ/dV for (c) charge and (d) discharge are calculated from data shown in (a) and (b). All four plots include shaded grey areas that represent two standard deviations. The standard deviations are not noticeable in the voltage curves ((a), (b)); but in the dQ/dV plots ((c),(d)), the standard deviations are large around the peaks, which are highlighted by the vertical bands

We can take the standard deviations calculated for each of the four plots in Figure 4.3 and obtain them for all replicate groups. In total, we have 9 replicate groups with sample sizes of three or greater. In fact, we have 13 replicate groups, two of those only have sample sizes of two cells, and two other groups had cells that did not all end at the same number of cycles and are hence not true replicates. Since OCV and dQ/dV are only measured at end-of-testing, a replicate group in this case consists of cells that have been cycled under the same conditions and have been cycled for the same number of total cycles. The standard deviations of the OCV for charge and discharge for all 11 replicate groups are shown in Figure 4.4a and 4.4b, while the relative standard deviations of dQ/dV are shown in Figure 4.4c and 4.4d.

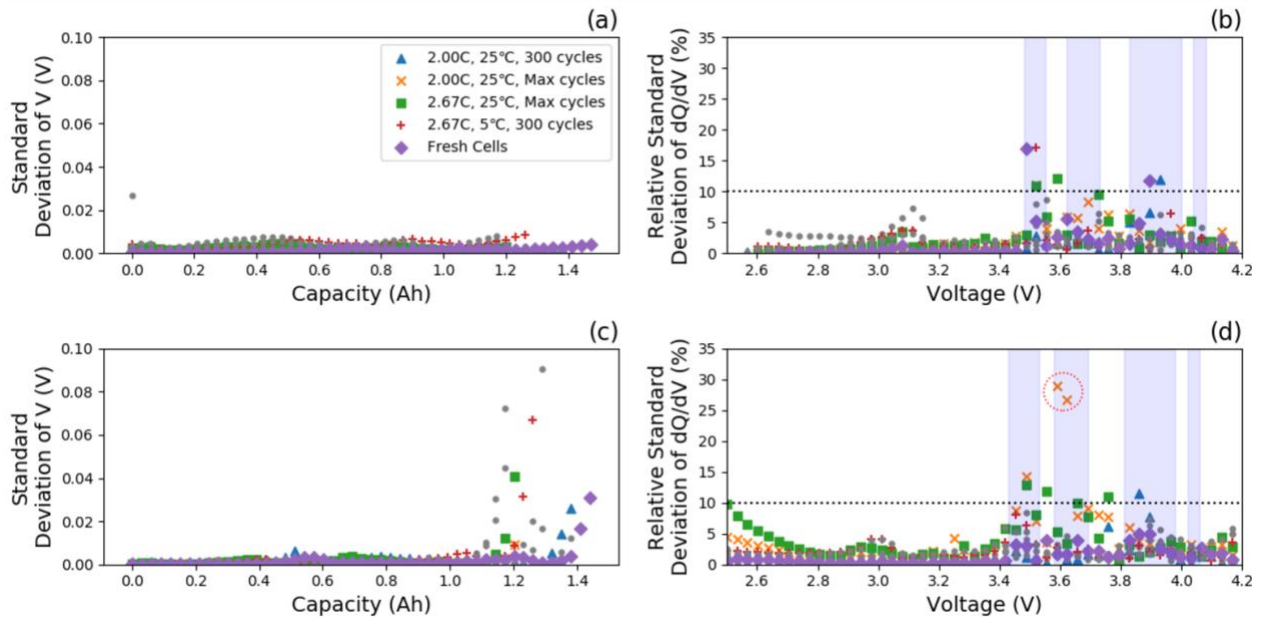


Figure 4.4: For each of the 10 replicate groups, the standard deviation of voltage for the end-of-testing C/20 (a) charge and (b) discharge, and the relative standard deviation for the corresponding dQ/dV during (c) charge and (d) discharge. Replicate groups with any value above a 10% relative standard deviation in (c) and (d) are labeled in the legend and represented by a different set of markers. All other replicate groups with smaller relative standard deviations are represented as grey circles. Vertical bands represent the voltage bands of peaks found in the dQ/dV plots in Figure 3(c),(d), where standard deviation is generally larger.

The standard deviation of the voltages are, for the most part, below 10mV. This is true with the exception of the end of discharge (Figure 4.3b), where there is large standard deviation up to ~90mV due to the steep dropoff in voltage at the end of discharge. For the dQ/dV , the relative standard deviations are high around the peaks, indicated by the blue vertical bands. We chose an arbitrary 10% for relative standard deviation as a measure of good data quality for the dQ/dV data.

All replicate groups that have any value of relative standard deviation for dQ/dV greater than 10% are labeled in the legend and represented by a different set of markers in Figure 4.4. The remaining replicate groups that have small relative standard deviations are represented as gray circles. We see that the replicate group at 2C, 25°C and cycled to the max number of cycles (1500 cycles, represented by orange crosses) have two points with high relative standard deviation in the discharge dQ/dV of ~25-30% (Figure 4.4d). We can take a deeper look at this replicate group in Figure 4.5.

In Figure 4.5, we show the voltage and dQ/dV data for each of the cells (as opposed to the mean values of the three cells as in Figure 4.3). We see that Cell 22 (orange line) has a large oscillatory behavior for the second peak around 3.6V for the discharge dQ/dV (Figure 4.5d). Upon further examination, this is due to the oscillatory behavior in the discharge voltage seen in the inset of Figure 4.5b, where we show a zoomed in plot of the voltage. The filtering window that we chose to obtain the dQ/dV (~0.0207 Ah) is of similar length scale as the voltage discrepancies, and thus does not filter out this behavior, instead, taking the derivative amplifies the noise. We could choose to use larger filtering windows to further remove the inherent noise in the data, but larger windows might also remove important features. Here, we show that the reason for the large relative standard deviation of the dQ/dV for this replicate group is due to the underlying voltage measurement that is probably caused by the test equipment. Thus, we have shown how aggregate statistical analysis can be used as a tool to examine specific outliers and as a measure of overall data quality.

For each cell, EIS measurements were carried out at 10%, 30%, and 50% SOC at the end of cycling. Again, we carry out the same statistical analysis on EIS data for replicate cells. Figure 4.6 is a Nyquist plot of the mean EIS measurement for cells 1-4 at 30% SOC, with the gray shaded area representing two standard deviations from the mean. These four cells have undergone cycling for 300 cycles under 2.67C and 25°C conditions. We observe that the EIS measurements for this replicate group of cells is relatively reproducible with low standard deviation at the high and middle frequencies, and slightly larger standard deviation at the lower frequency tail.

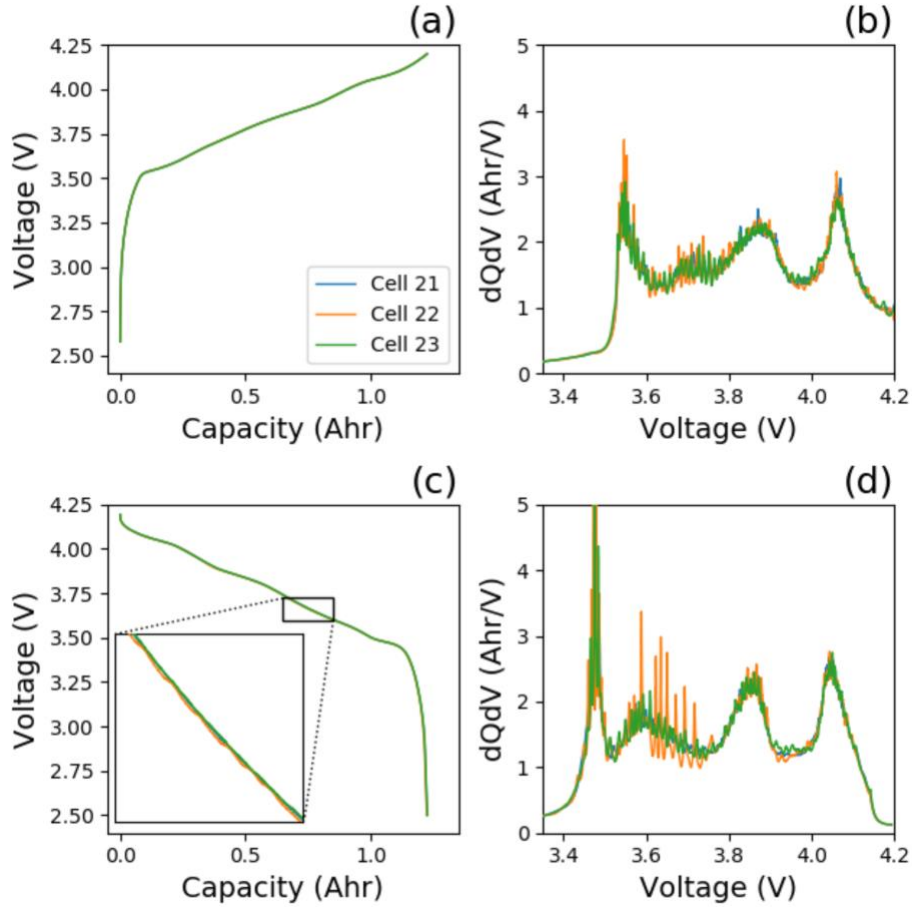


Figure 4.5: End-of-testing C/20 (a) charge and (b) discharge voltage curves for each of the three cells found in the replicate group cycled under the 2C, 25oC condition, and cycled for 1500 cycles. The inset of (b) shows a zoomed in plot of the voltage, where voltage measurements for cell 22 have an oscillating behavior. This can explain the oscillatory behavior of cell 22's dQ/dV plot for (c) charge and (d) discharge.

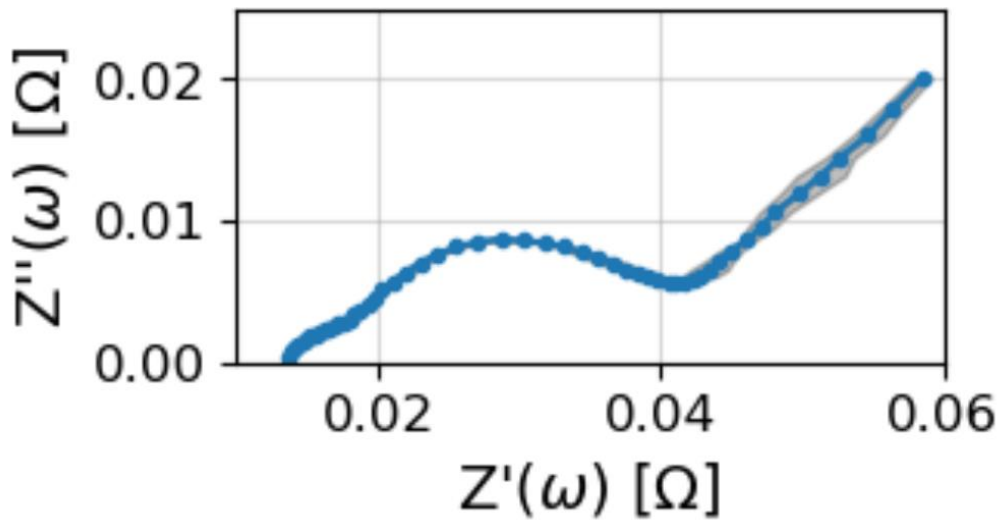


Figure 4.6: Nyquist plot of the mean value of EIS measurements at SOC=30% of cells 1,2,3,4. These cells have undergone cycling for 300 cycles, under 2.67C and 25degC conditions. The shaded grey area represents two standard deviations.

For each of the 9 replicate groups, we can calculate the relative standard deviation at each frequency for both the real and imaginary impedance. This is shown for the EIS measurements at 30% SOC in Figure 4.7. We observe that one replicate group has significantly higher relative standard deviation than all other replicate groups. This replicate group (2C, 25oC, 300 cycles, cells 13-16; plotted as blue squares in Figure 4.7) has higher relative standard deviation for real impedance in the low to middle frequencies, and higher relative standard deviation for imaginary impedance in the middle frequencies. Upon closer inspection, we see that the reason for this large deviation is due to a single cell being an outlier. Figure 8 is the Nyquist plot of the EIS of all four cells in the above replicate group at 30% SOC. The impedance for cell 13 is significantly different from cells 14, 15, and 16, hence translating to the large standard deviation of this replicate group. In this manner, aggregated statistical analysis of all EIS spectra collected allows us to easily point out cells that are outliers. Additionally, building a dataset with replicate cells allows us to have confidence in our measurements as the EIS of the other three cells demonstrate high quality reproducibility.

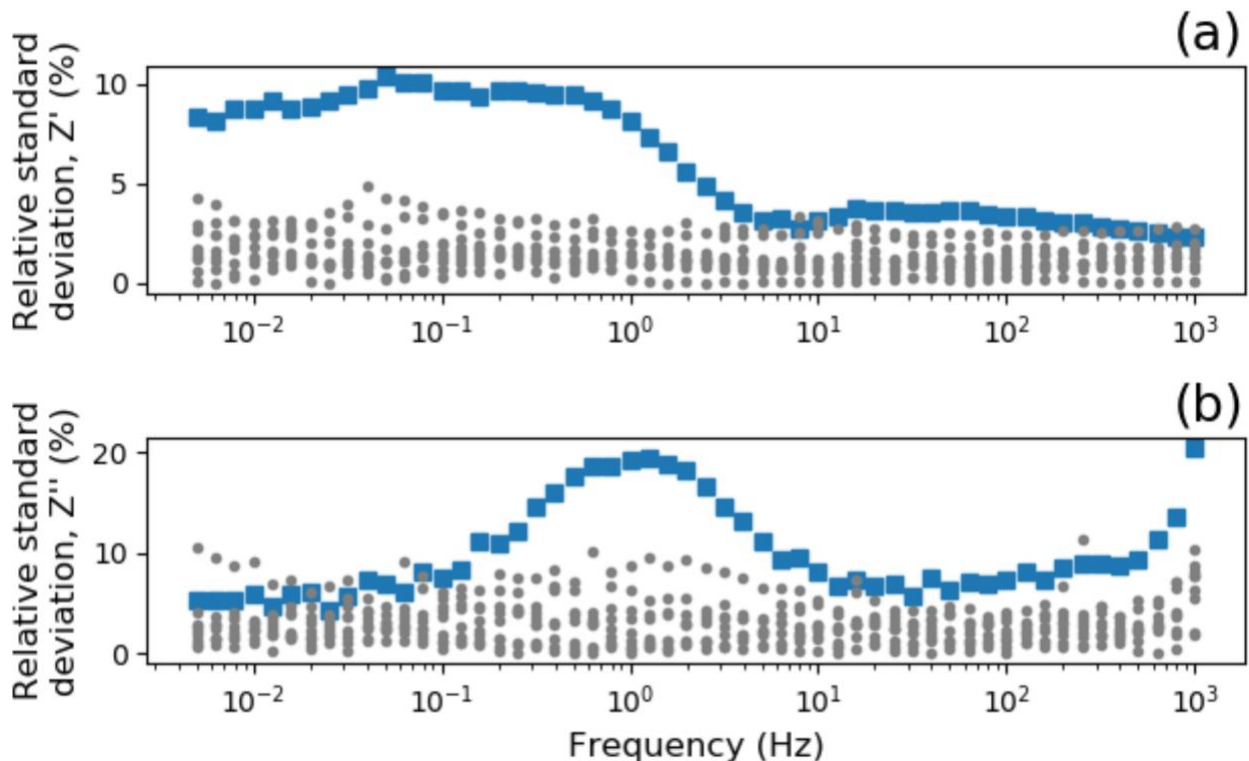


Figure 4.7: The relative standard deviation of the (a) real and (b) imaginary impedance as a function of frequency for each of the 12 replicate groups, for SOC=30%. The blue square markers represent a replicate group that has high relative standard deviation (2C, , 25degC, 300 cycles). All other replicate groups with smaller relative standard deviation are plotted as grey circles.

Figure 4.8 is the Nyquist plot of the EIS of all four cells in the above replicate group at 30% SOC. The impedance for cell 13 is significantly different from cells 14, 15, and 16, hence translating to the large standard deviation of this replicate group. In this manner, aggregated statistical analysis of all EIS spectra collected allows us to easily point out cells that are outliers. Additionally, building a dataset with replicate cells allows us to have confidence in our measurements as the EIS of the other three cells demonstrate high quality reproducibility.

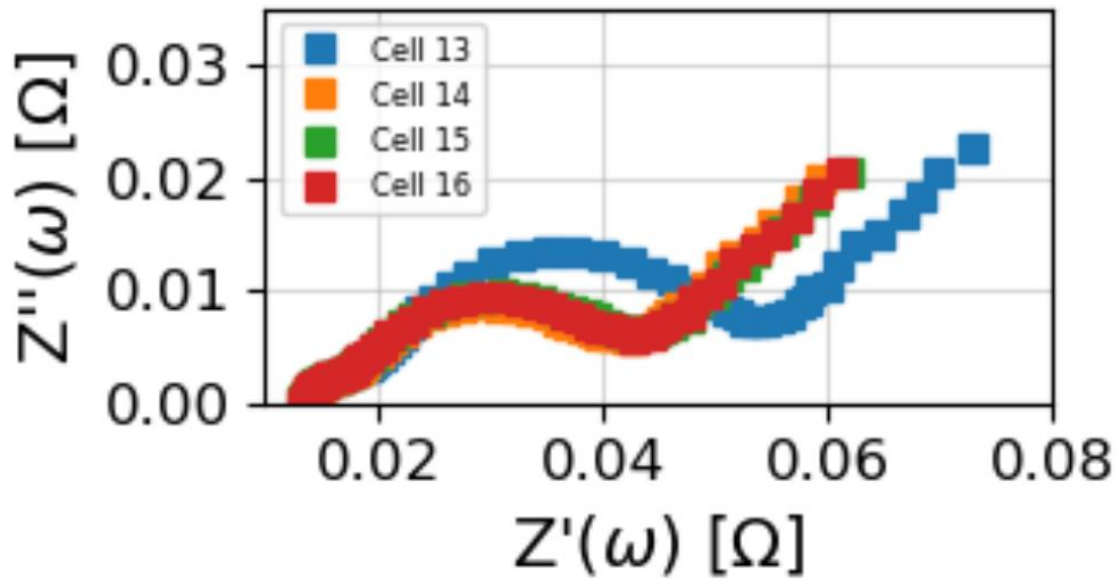


Figure 4.8: Nyquist plot of EIS measurements at SOC=30% for cells 13,14,15,16. This replicate group set (2C, 25degC, 300 cycles) is represented as having high relative standard deviation in Figure 4.7 as blue square markers.

Finally, validation of collected EIS spectra is also important as discussed in the Methods section. The real and imaginary residual percentage errors from carrying out the linear Kramers-Kronig analysis for all 141 EIS spectra are plotted in Figure 9a. Having residuals $<2\%$ is indicative of a valid EIS measurement¹⁰⁶. Here, we point out two cases with the highest maximum residual errors of 4.63% and 5.02%, which corresponds to the EIS spectra in Figure 4.9bi and 4.9ci respectively, and we can see the residual errors for each frequency in Figure 4.9bii and 4.9cii.

The spectrum in Figure 4.9bi is for cell 33 at 10% SOC which has been cycled for 300 cycles under the 2C, 5oC condition. We observe that there are two residuals of $\sim 2.5\%$ and $\sim 5\%$ at low frequencies (9bii) and this corresponds to the points in the low frequency tail that deviate the most from the smooth fitted line. This means that the measurements at those frequencies might not

be valid and violate the conditions required for EIS, but the rest of the spectrum at middle and high frequencies can still be considered as valid. The spectrum in Figure 4.9ci is for cell 10 at 30% SOC which has been cycled for 1500 cycles under the 2.67C, 25oC condition. In this case, there are a few residuals that are relatively high at middle frequencies (~100Hz) with the largest residual being 5.02%. It is more challenging to visualize where these points might deviate from the fitted curve in this scenario but we can assume, based on the larger residuals, that the measurement is not valid due to the cell being non-stationary for example.

Validation of EIS measurements is important to ensure that any further analysis or interpretation of the data is reliable. Having tools to look at the magnitude and frequencies of the residuals can give us a better idea of data quality and guide data processing. For example, in the case of cell 33 here (Figure 4.9bi), we might suggest removing the top two residuals while still keeping the data for the rest of the spectrum.

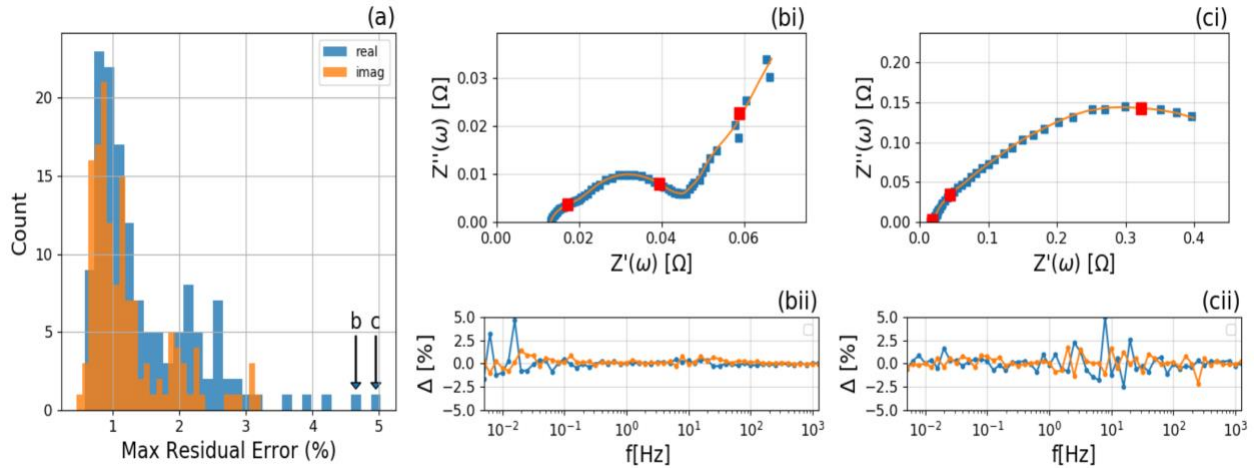


Figure 4.9: (a) Maximum residual percentage errors for real and imaginary values for all 141 collected EIS spectra is shown as a histogram. Nyquist plots of EIS spectra for (bi) cell 33 at SOC=10% and (ci) cell 10 and SOC=30%. Data is shown as blue square markers while the orange line is the fitted result from the Lin-KK model. The corresponding percentage residual error from the fit of real and imaginary data to the Link-KK model at all frequencies is plotted in (bii) and (cii). The highest real residual error shown in (bii) is 4.63%, and in (cii) is 5.02%, which are plotted and indicated by the arrows in (a).

4.3 Metadata

The Battery Data Genome group, created a framework for organizing, categorizing, and sharing battery data, whether from fundamental material and electrode design experiments, cell-level data, module/pack data, or field data. Organizing principles for this design included: creating uniform standards and protocols for experiments and sharing results, making metadata as important of a priority, ensuring data is cleaned and metadata is clear, and finally to include flexibility so not all data or metadata from a given experiment need to be shared. To encourage the most community participation as possible and because some data may be proprietary, the metadata is organized into primary, secondary and tertiary layers. Figure 4.X shows the suggested metadata and how they relate across scales.

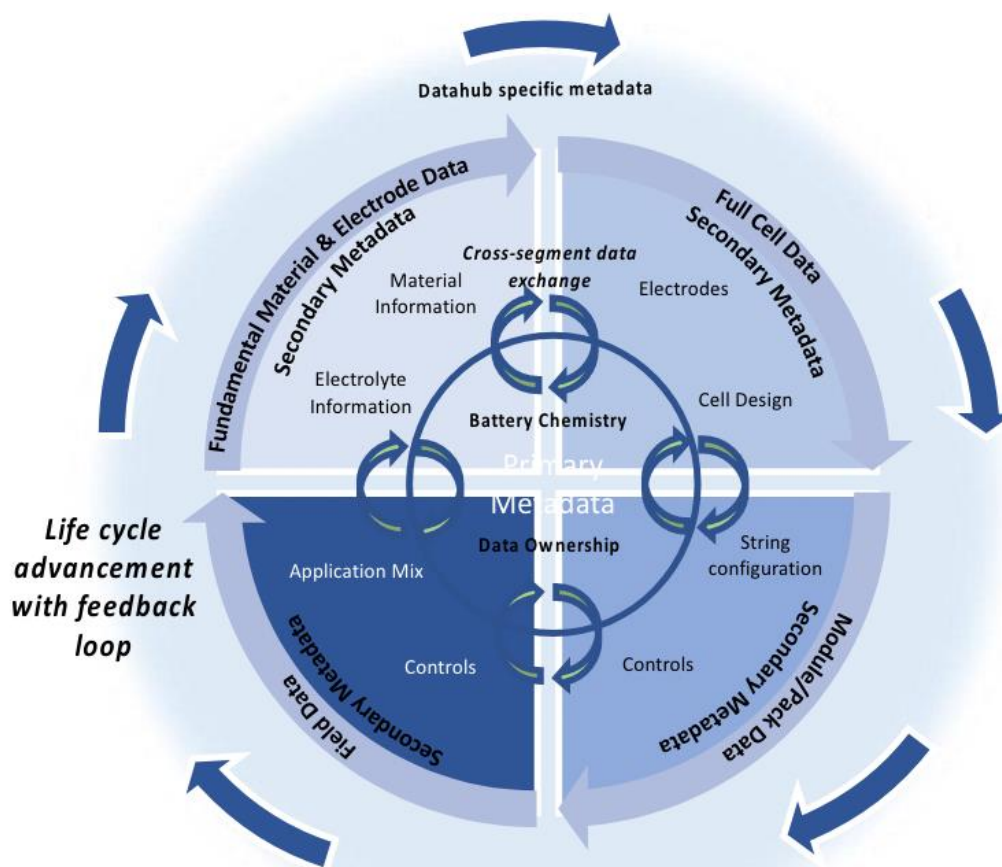


Figure 4.10: Organizing principles for primary, secondary, and tertiary metadata

In order to enable rapid searching and filtering of data, and to enable consistency of comparisons between data, the Battery Data Genome group suggests at least that the following minimum set of primary metadata relevant for all situations should be included when datasets are shared. (1) A globally unique identifier (UID) for each cell is required to enable cross referencing between databases, and to cell information. (2) To enable rapid data querying and filtering, we need to specify the objective of a test (e.g., calendar aging, fast charging optimization, EV drive cycles, square wave cycling), the cell chemistry of both electrodes, and nominal capacity. (3) Identification of test equipment used should be included to enable consistent comparisons. (4) Finally, contact details of the organization which published the data should be included. Standard formatting of primary metadata should be enforced to ensure interoperability. The Table below shows an example of a metadata checklist that should be filled out when publishing a dataset and was used for the JCDREAM dataset.

Table 4.2: Metadata checklist, following Battery Genome primary metadata suggestions

<u>Primary Metadata</u>	<u>Example</u>
Unique Identifier (UID)	6
Objective of Test	Calendar Aging
Anode Chemistry	Graphite
Cathode Chemistry	NMC
Nominal Capacity (Ah)	2.0
Test Equipment Used	Maccor96
Contact Details	abs@def.edu

Rather than dictating a rigid structure, the Battery Data Genome group suggests a number of areas that could be further developed by the community to become secondary metadata ‘lego bricks’ or building blocks, that can be slotted in as required:

- **Cell design:** Composition, additives, mass loading of each electrode
- **Experiment design:** Test protocols and techniques
- **Constituent materials:** Electrodes, electrolyte, binder, separator
- **Geometric data:** Electrode thicknesses, porosity, particle size and distribution
- **Commercial cell data:** Manufacturer, model name and number, link to datasheet
- **Test setup details:** Mechanical fixings, applied pressure, etc.
- **References:** Links to papers, reports, designs of experiments, protocols

The metadata is stored in JSON files, so they can be incorporated into a JSON schema. An example of one of these files looks like the following:

```
{
  "UID":"UWEMI_1",
  "cell_number":1,
  "objective":"cyclling",
  "C-rate":2.67,
  "cycles":300,
  "temp":25,
  "nominal_capacity";1500
  "anode_chemistry":"graphite",
  "cathode_chemistry":"NMC",
  "Manufacturer":"Samsung",
  "Model_ID":"INR18650-15M",
  "instrument":"Maccor96",
  "filename":"JCDREAM_BatteryCorpus_2-67C_300Cycles_Cell1 - 073.csv",
  "stats_filename":"JCDREAM_BatteryCorpus_2-67C_300Cycles_Cell1 - 073 [STATS].csv",
  "EIS":"../EIS_data/Autolab_EIS_Data/Cell1",
  "Owners":"UW_EMI_Lab",
  "Contact":"dts@uw.edu"}

```

4.4 Schema



Figure 4.11: Proposed schema from the Battery Genome Group. This includes primary, secondary, and tertiary metadata.

4.5 Conclusions

In this work, we present a dataset that includes cycling data and diagnostic measurements for Li-NMC commercial cells at various C-rates, temperatures, SOHs, and SOCs. The motivation of this dataset is to contribute to the battery open-data community, while also showing the importance of prioritizing replicates in cycling datasets to account for cell variation. Most of the measurements in this study have four replicates for each condition. We highlight the usefulness of using statistical tools to point out outliers and inconsistencies in data quality due to either equipment or experimental measurement error, or cell variability. This is only possible with the inclusion of replicate data and allows us to have more confidence in any trends or interpretations of results from this dataset. Furthermore, we also quantified the variance in these commercial cells for various measurements, and we believe the variance for in-house cells would be higher, which further emphasizes the importance of replicate data to have larger sample sizes for statistically significant conclusions.

Chapter 5 - Additional Projects

5.1 Motivation

Energy conversion devices create electricity through electrochemical reactions. Fuel cells are a common energy conversion device. They can be thought of as an “electrochemical combustor”, since a fuel, methane for this work, is oxidized, heat is released and electrons are exchanged. However, they are reacting in separate channels.¹⁰⁷ This configuration is much more efficient than the traditional combustion reaction, usually occurring by burning the methane as fuel and expanding in a gas turbine. The efficiency of generating electricity by burning methane is limited by the theoretical limits set by the Carnot Cycle.¹⁰⁸ Because SOFCs utilize reversible reactions and operate isothermally, the efficiency is not limited by the Carnot efficiency. Instead, the maximum work possible for a fuel cell is equal to the Gibbs Free Energy of the system.¹⁰⁹ For example, for a fuel cell using methane fuel at standard temperature and pressure, the maximum efficiency would be around 92%. For a Carnot heat engine to reach the same efficiency, it would have to have a heat source, or high temperature, of 3,725 K.

There are a myriad of fuel cell types, but this work will focus on solid oxide fuel cells (SOFCs). SOFCs operate at high temperatures, around 800-1000°C, have rapid electrode kinetics, slow start-up times, and significant thermal expansion.¹¹⁰ Due to these factors, they are ideal for powering large loads, such as buildings. SOFCs that use methane as the fuel belong to another subset of fuel cells, Natural Gas Fuel Cells (NGFCs). NGFCs are great candidates for transitional renewable energy technologies, as natural gas is a readily available resource in the United States.¹¹¹

Numerical models have been a growing field of research for SOFCs to optimize design for performance, stability, reliability, and fuel utilization¹¹². These tools allow designers to adjust parameters such as geometry, material properties, electrochemical performance, fuel inputs, stack power output limits, and temperature¹¹³. Some models also include the effects of including carbon capture to the system to reduce emissions¹¹⁴. Expanding the models to include system units for the entire plant are important, as some of the biggest set-backs for SOFCs are scale-up and cost of manufacturing¹¹⁵. Recently, machine learning techniques have been combined with these models

to improve performance predictions and computation efficiency for system-scale models ¹¹⁶. This work aims to compile published systems-level and physics-based models with software to create user-friendly and open-source tools that scientists and engineers can use to design more efficient SOFCs.

5.2 User-Friendly Jupyter Notebooks for Process Design and Modeling

We were a part of an ARPA-E funded collaboration effort between Pacific Northwest National Labs (PNNL) and the National Energy Technologies Lab (NETL) to develop an integrated software that will allow users to design system process flowsheets. Our task was to create a graphic user interface (GUI) using Jupyter Notebooks, to guide the user through the design process.

5.2.1 Methodology

This work utilizes the Institute for the Design of Advanced Energy Systems (IDAES) Process Systems Engineering (PSE) framework, created by NETL.¹¹⁷ The IDAES PSE framework created a Python package, `idaes-pse`, to bridge the gap between advanced simulation packages and algebraic modeling languages (AMLs). The `idaes-pse` package utilizes `Pyomo` (Python Optimization Modeling Objects), a python-based AML.¹¹⁸

This work proposes implementing the Solid Oxide Fuel Cell Multiphysics (SOFC-MP) model created at PNNL to create the simulation data. The data is then used to create a reduced order model (ROM), which will be the input for the IDAES optimization. The ROM is created by randomly samples input parameters, finds stack solutions, performs regression to determine stack performance and other metrics.¹¹⁹ Once the ROMs are generated, conceptual system designs can be formulated as a superstructure optimization (SO) problem.¹²⁰

5.2.2 Notebook Format

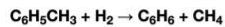
For each process system example, there will be a corresponding Jupyter Notebook. The purpose of the notebooks is to guide the user through the flow-sheet building protocol. The notebooks are divided into five sections:

1) Background and Imports

In the first section, the process (i.e. hydrodealkylation or methanol synthesis) is described. Packages needed for the notebook are also imported. First, the reinforcement learning function (RL_call) is imported from RL_CORE.py. Next, widgets.py is imported. This file contains all the ipywidget functions that the notebook uses to set variables from user inputs.

▼ IDAES-PSE and Reinforcement Learning (RL): HDA Example Notebook

The purpose of this notebook is to guide the user through the flow sheet design process. For this example, we will be designing a **hydrodealkylation (HDA)** process system, in which toluene reacts with hydrogen gas at high temperatures to form benzene.



```
In [1]: from RL_CORE import RL_call
import widgets
import ipywidgets
```

2) Select Units

In this section, the user selects the maximum number of units that will be included in the unit list. All possible units are shown, with a dropdown menu. The dropdown gives the option of 0, 1, or 2 units. These inputs are then used to create a list of units, a list of inlets, and a list of outlets, that are saved as the class *user_inputs* and passed to the reinforcement learning function.

▼ Select Units

```
In [2]: w = widgets.select_units()
```

Use the dropdowns to select number of units.

```
In [3]: display(w)
```

Heater	1	▼
Cooler	0	▼
Heat Exchanger	0	▼
Reactor	1	▼
Mixer	1	▼
Flash	1	▼
Splitter	1	▼
Compressor	1	▼
Expander	0	▼
Turbine	0	▼

Check that the resulting list matches your input.

3) RL Options

In this section, the user selects reinforcement learning parameters. They can either use the slider widgets and dropdowns to make their selections, or they can keep the default values. Currently, the notebook includes episodes, greedy, greedy increment, learning rate, and GNN enabled/disabled parameters. More can be added in the future as desired. The inputs are saved as a dictionary, *P*.

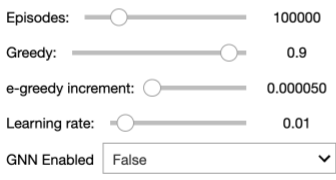
RL Options

Select desired reinforcement learning parameters

First, how many episodes or training steps? (Default: 300,000) Next, define the starting *e-greedy* value, or whether the model prioritizes **exploration** vs. **highest reward**. A value of 1 means the model only explores, whereas a value of 0 means the model only picks the highest reward. (Default: 0.8) Then, select the *e-greedy increment* and learning rate and GNN option.

```
In [8]: r = widgets.RL_options()
```

```
In [10]: display(r)
```



```
In [11]: P = {'model_restore':False,'model_save':False,'Episode_max_mode':'static','Episode_max':r.result[0],
'threshold_learn':-1,'model_index':1,'GNN_enable':eval(r.result[4]),'learning_rate':r.result[3],
'reward_decay':0.5,'e_greedy':r.result[1],'replace_target_iter':200,'memory_size':20000,
'e_greedy_increment_ref':r.result[2],'e_greedy_increment_type':'variable',
'batch_size':32,'e_greedy_increment_intervals':[0,0.4,0.6,0.7,0.8,0.9,1.0],
'e_greedy_increment_ratios':[1,1,1,1,1,1],'Additional_step':500}
```

4) Run RL

In this section, the reinforcement learning program is run. The resulting flowsheets and diagnostic plots are saved into a folder.

Run RL

```
In [12]: RL_call(user_inputs(),P)
```

```
Maximum episode : 100500
WARNING:tensorflow:From /Users/ericcaeggleton/miniconda3/envs/idaes/lib/python3.7/site-packages/tensorflow/python/training/rmsprop.py:119: calling Ones._init__ (from tensorflow.python.ops.init_ops) with dtype is deprecated and will be removed in a future version.
Instructions for updating:
Call initializer instance with the dtype argument instead of passing it to the constructor
Training RL model=====
Episode: 0/100500, percent: 0.0% , Reward: -1000
epsilon=== 0.0001 increment=== 5e-05
Episode: 1000/100500, percent: 1.0% , Reward: -1140
epsilon=== 0.0501 increment=== 5e-05
Episode: 2000/100500, percent: 1.99% , Reward: -700
epsilon=== 0.1 increment=== 5e-05
Episode: 3000/100500, percent: 2.99% , Reward: -740
epsilon=== 0.15 increment=== 5e-05
Episode: 4000/100500, percent: 3.98% , Reward: -2000
epsilon=== 0.2 increment=== 5e-05
Episode: 5000/100500, percent: 4.98% , Reward: -800
epsilon=== 0.25 increment=== 5e-05
```

5.3 Solid Oxide Fuel Cell Modeling and Parameter Estimations

Our other task was to improve the I-V relationship models used by the SOFC-MP. The original relationship is outdated for some fuel cell materials and configurations. The SOFC-MP model was designed to allow users to input their own model or subroutine for defining the current-voltage (I-V) relationship.¹¹² If a specific subroutine is not imported, the default method involves using the Nernst equation along with Butler-Volmer kinetics equations, as seen in fundamental fuel cell models.¹²¹ This relationship depends on fuel cell parameters, such as temperature, species concentrations, cell materials, thickness, and conductivity. We updated the default subroutines available by reviewing performance results published in the literature for various SOFC electrode materials and configurations.^{122–124} We used experimental data to fit our model parameters. Figures 5.1 and 5.2 show optimization results.

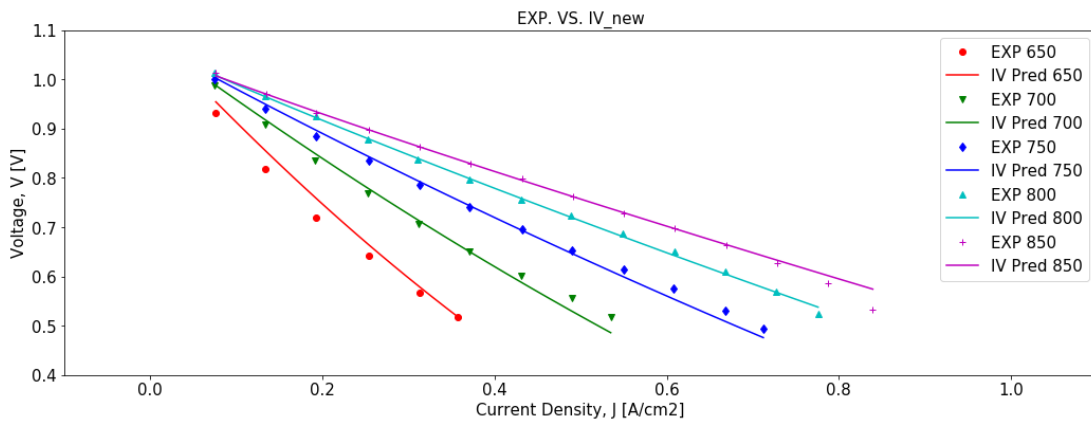


Figure 5.1: Parameter optimization results for first dataset.

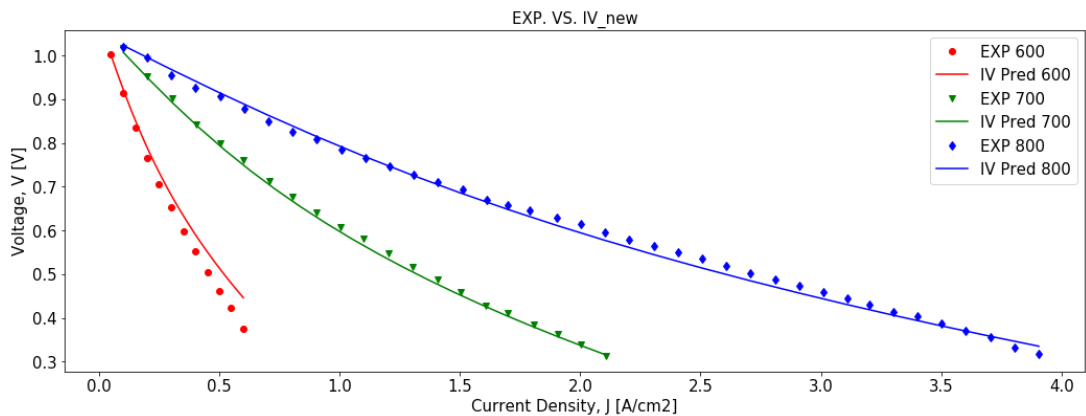


Figure 5.2: Optimization results from second dataset.

Chapter 6 - Conclusions and Future Work

6.1 Summary

In this work we demonstrated how multiscale models can provide insights into transportation electrification. By using the longitudinal vehicle dynamics model, routes were able to be compared based on battery efficiency and longevity. Next, we converted the load profiles from Route Dynamics to a cell-level profile. We introduced a simple cell-level battery model, and we used experimental data to calibrate the model parameters. These parameters were then used to estimate the voltage and current profiles for another route. Lastly, we analyzed a cycling dataset that included four replicates, so we could investigate variability in cell performance. The suggested metadata and schema for sharing similar datasets was also introduced.

6.2 Future Work

6.2.1 Systems-Level and Vehicle Dynamics

The Route_Dynamics software should be tested for accuracy by comparing the results to real on-board data from a battery-electric bus on a route that can be input into the model. These measurements would allow us to see how well the model is predicting load and energy demands and help us isolate areas of improvement. Then, once we have verified the model, more inputs could be included. Instead of randomly selecting which traffic lights the bus will stop at, a Monte Carlo simulation could be used, based on the popularity of the intersection and time of day. Next, it would be a great improvement to include temperature in the model. First, knowing the temperature can allow the auxiliary demand estimate to change based on predicted use. Second, temperature can cause certain degradation events to happen more readily. A temperature input could be used to weight the battery stress estimates. Lastly, this dissertation discussed ways that we can model at the cell-level as well. This type of model could be added to Route_Dynamics as an additional module.

6.2.2 Module-Level

The cell model introduced in Chapter 3 can be extended to the pack or module-level, given the cell configurations. Once this is done, it would be beneficial to simulate cell-balancing protocols. This will help understand which cell in a pack might degrade faster. Second, a thermal model could be added, and estimate temperature gradients across the module, which also helps to better understand possible degradation.

6.2.3 Cell-Level Modeling

The model proposed in Chapter 4 is the simplest approximation. The first improvement that can be made to the estimate is to experimentally determine apparent resistance. This can be determined experimentally by use a stair-step of currents across the total SOC window, for both charge and discharge. The resistance can then be calibrated if V_{OC} is known as a function of SOC. This can be determined by using slow-scan charge and discharge cycling protocols. This relationship is established for the cells used in this study as a result of slow-scan (C/20) charging and discharging. Also, if V_{OC} is known as a function of state of charge, then only equation 3 would be needed and with the current given at each point, the SOC could be calculated with the following:

$$SOC_i = SOC_{i-1} + (I_i + I_{i-1}) * (t_i - t_{i-1}) / (2 * \Delta Q_{cell})$$

Alternatively, physics-based battery models could give more detailed insights. Model parameters could be adjusted based off EIS data, to accommodate for degradation. Thermal models could also be added, to link to temperature-related degradation mechanisms.

Lastly, the cycling fitting would ideally be repeated for the exact cells or at least cell chemistry on-board the bus of interest. The Samsung cells used in this study are high power, however the ones in the vehicle may prioritize energy, which would lead to different charge and discharge characteristics.

Bibliography

1. S. Manabe and A. J. Broccoli, *Beyond Global Warming: How Numerical Models Revealed the Secrets of Climate Change*, Princeton University Press, Princeton, NJ, (2020).
2. V. Masson-Delmotte et al., *Global Warming of 1.5°C. An IPCC Special Report on the impacts of global warming of 1.5°C above pre-industrial levels and related global greenhouse gas emission pathways, in the context of strengthening the global response to the threat of clim*, (2019).
3. P.R. Shukla, J. Skea, R. Slade, A. Al Khourdajie, R. van Diemen, D. McCollum, and M. Pathak, S. Some, P. Vyas, R. Fradera, M. Belkacemi, A. Hasija, G. Lisboa, S. Luz, J. Malley, : *Climate Change 2022: Mitigation of Climate Change. Contribution of Working Group III to the Sixth Assessment Report of the Intergovernmental Panel on Climate Change*.
4. EPA, *Inventory of US Greenhouse Gas Emissions and Sinks*, (2022) <https://www.epa.gov/system/files/documents/2022-04/us-ghg-inventory-2022-main-text.pdf>.
5. Colin McKerracher et al., *Electric Vehicle Outlook 2021*, BloombergNEF, (2021) <https://about.bnef.com/electric-vehicle-outlook/>.
6. DOE, *The Bipartisan Infrastructure Deal Will Deliver For American Workers, Families and Usher in the Clean Energy Future* (2021) <https://www.energy.gov/sites/default/files/2022-04/BIL%20Factsheet.pdf>.
7. IEA, (2021) <https://www.iea.org/reports/tracking-transport-2021>.
8. K. County, 329 (2020).
9. G. E. Blomgren, *J. Electrochem. Soc.*, **164**, A5019–A5025 (2017).
10. A. Masias, J. Marcicki, and W. A. Paxton, *ACS Energy Lett.*, **6**, 621–630 (2021).
11. S. Bakker and R. Konings, *Transportation Research Part D: Transport and Environment*, **64**, 204–215 (2018).
12. New Flyer, 1–2 (2017).
13. New Flyer, (2020).
14. (2020) <https://www.xaltenergy.com/products/>.
15. A123, (2020) [a123systems.com/automotive/products/](https://www.a123systems.com/automotive/products/).
16. M. Armand and J.-M. Tarascon, *Nature*, **451**, 652–657 (2008).
17. D. B. Richardson, *Renewable and Sustainable Energy Reviews*, **19**, 247–254 (2013).
18. C. Angerer, S. Krapf, A. Buß, and M. Lienkamp, in *Volume 3: 20th International Conference on Advanced Vehicle Technologies; 15th International Conference on Design Education*, p. V003T01A024, American Society of Mechanical Engineers, Quebec City, Quebec, Canada (2018)

<https://asmedigitalcollection.asme.org/IDETC-CIE/proceedings/IDETC-CIE2018/51784/Quebec%20City,%20Quebec,%20Canada/276004>.

19. M. Gallet, T. Massier, and T. Hamacher, *Applied Energy*, **230**, 344–356 (2018).
20. J. Asamer, A. Graser, B. Heilmann, and M. Ruthmair, *Transportation Research Part D: Transport and Environment*, **46**, 182–199 (2016).
21. S. Ebbesen, P. Elbert, and L. Guzzella, *IEEE Trans. Veh. Technol.*, **61**, 2893–2900 (2012).
22. A. Franca, J. A. Fernandez, C. Crawford, and N. Djilali, in *2017 IEEE Transportation Electrification Conference and Expo (ITEC)*, p. 679–683, IEEE, Chicago, IL, USA (2017) <http://ieeexplore.ieee.org/document/7993351/>.
23. B. Varga, A. Sagoian, and F. Mariasiu, *Energies*, **12**, 946 (2019).
24. B. Borlaug et al., *Nat Energy*, **6**, 673–682 (2021).
25. J. D. Hunt et al., *Energy*, **248**, 123495 (2022).
26. G. Plett, *Battery Management Systems, Volume I: Battery Modeling*, Artech House, (2015).
27. B. Saha, S. Poll, K. Goebel, and J. Christophersen, in *2007 IEEE Autotestcon.*, p. 646–653, IEEE, Baltimore, MD, USA (2007) <http://ieeexplore.ieee.org/document/4374280/>.
28. J. Vetter et al., *Journal of Power Sources*, **147**, 269–281 (2005).
29. A. Barré et al., *Journal of Power Sources*, **241**, 680–689 (2013).
30. R. Deshpande, M. Verbrugge, Y.-T. Cheng, J. Wang, and P. Liu, *J. Electrochem. Soc.*, **159**, A1730–A1738 (2012).
31. K. Jalkanen et al., *Applied Energy*, **154**, 160–172 (2015).
32. S. M. Rezvanizani, Z. Liu, Y. Chen, and J. Lee, *Journal of Power Sources*, **256**, 110–124 (2014).
33. D. Beck, J. Carothers, V. Subramanian, and J. Pfaendtner, *AIChE*, **62**, 1402–1416 (2016).
34. V. Sulzer, S. G. Marquis, R. Timms, M. Robinson, and S. Jon, 9.
35. T. Tranter et al., *JOSS*, **7**, 4051 (2022).
36. M. Murbach, B. Gerwe, N. Dawson-Elli, and L. Tsui, *Journal of Open Source Software*, **5**, 2349 (2020).
37. A. Lewis-Douglas, L. Pitt, and D. A. Howey, *arXiv:2010.14959 [cs, eess]* (2020) <http://arxiv.org/abs/2010.14959>.
38. D. T. Schwartz, M. D. Murbach, and D. A. C. Beck, *ECS Interface*, **28**, 45–46 (2019).
39. Sandia, (2019) <https://www.sandia.gov/energystoragesafety-ssl/research-development/research-data-repository/>.

40. L. Ward et al., 45.
41. ZeEUS, *ZeEUS eBus Report*, (2016) <https://zeeus.eu/uploads/publications/documents/zeeus-ebus-report-internet.pdf>.
42. S. Pelletier, O. Jabali, J. E. Mendoza, and G. Laporte, *Transportation Research Part C: Emerging Technologies*, **109**, 174–193 (2019).
43. S. Bakker and R. Konings, *Transportation Research Part D: Transport and Environment*, **64**, 204–215 (2018).
44. O. Vilppo and J. Markkula, *WEVJ*, **7**, 357–365 (2015).
45. A. Lajunen and T. Lipman, *Energy*, **106**, 329–342 (2016).
46. New Flyer, (2017).
47. New Flyer, (2020).
48. XALT Energy Products, (2021) <https://www.xaltenergy.com/products/>.
49. A123, *A123 Products*, (2020) a123systems.com/automotive/products/.
50. T. Ly, D. Goehlich, and L. Heide, in *2016 IEEE Vehicle Power and Propulsion Conference (VPPC)*, p. 1–6 (2016).
51. C. P. Aiken et al., *J. Electrochem. Soc.*, **169**, 050512 (2022).
52. L. Eudy and M. Jeffers, *Foothill Transit Battery Electric Bus Demonstration Results: Second Report*, (2017), p. NREL/TP--5400-67698, 1369137 <http://www.osti.gov/servlets/purl/1369137/>.
53. S. Ebbesen, P. Elbert, and L. Guzzella, *IEEE Trans. Veh. Technol.*, **61**, 2893–2900 (2012).
54. G. De Filippo, V. Marano, and R. Sioshansi, *Applied Energy*, **113**, 1686–1691 (2014).
55. D. Göhlich, A. Kunitz, and T. Ly, in, p. 137–149, The Algarve, Portugal (2014) <http://library.witpress.com/viewpaper.asp?pcode=UT14-012-1>.
56. P. Sinhuber, W. Rohlf, and D. U. Sauer, in *2012 IEEE Vehicle Power and Propulsion Conference*, p. 315–320 (2012).
57. J. Vepsäläinen, A. Ritari, A. Lajunen, K. Kivekäs, and K. Tammi, *Energies*, **11**, 3267 (2018).
58. M. Rogge, E. van der Hurk, A. Larsen, and D. U. Sauer, *Applied Energy*, **211**, 282–295 (2018).
59. Ş. Yıldırım and B. Yıldız, *Transportation Research Part C: Emerging Technologies*, **129**, 103197 (2021).
60. Y. Wang, Y. Huang, J. Xu, and N. Barclay, *Transportation Research Part E: Logistics and Transportation Review*, **100**, 115–132 (2017).
61. B.-R. Ke, C.-Y. Chung, and Y.-C. Chen, *Applied Energy*, **177**, 649–660 (2016).

62. C. Fiori, K. Ahn, and H. A. Rakha, *Applied Energy*, **168**, 257–268 (2016).
63. J. Vepsäläinen, K. Otto, A. Lajunen, and K. Tammi, *Energy*, **169**, 433–443 (2019).
64. O. A. Hjelkrem, K. Y. Lervåg, S. Babri, C. Lu, and C.-J. Södersten, *Transportation Research Part D: Transport and Environment*, **94**, 102804 (2021).
65. C. De Cauwer, W. Verbeke, T. Coosemans, S. Faid, and J. Van Mierlo, *Energies*, **10**, 608 (2017).
66. C. R. Birkl, M. R. Roberts, E. McTurk, P. G. Bruce, and D. A. Howey, *Journal of Power Sources*, **341**, 373–386 (2017).
67. King County Metro, (2017).
68. M. Ehsani, Y. Gao, S. Longo, and K. M. Ebrahimi, *Modern Electric, Hybrid Electric, and Fuel Cell Vehicles*, CRC Press, (2018).
69. M. Meywerk, *Vehicle Dynamics*, Wiley, (2015).
70. Z. Gao et al., *Energy*, **122**, 588–600 (2017).
71. FTA, (2015) <https://www.altoonabustest.psu.edu/bus-details.aspx?BN=1405>.
72. H. Abdelaty and M. Mohamed, *Energies*, **14**, 2824 (2021).
73. Washington Department of Natural Resources, (2016) <http://lidarportal.dnr.wa.gov/>.
74. King County GIS Center, (2017) <https://www5.kingcounty.gov/gisdataportal/>.
75. SciPy, (2015) https://docs.scipy.org/doc/scipy-0.16.1/reference/generated/scipy.signal.savgol_filter.html.
76. B. Y. Boroujeni, H. C. Frey, and G. S. Sandhu, *Journal of Transportation Engineering*, **139**, 605–611 (2013).
77. R. A. Brater, (2016).
78. P. Shen, Z. Zhao, J. Li, and X. Zhan, *Transportation Research Part D: Transport and Environment*, **59**, 346–360 (2018).
79. P. Keil and A. Jossen, *J. Electrochem. Soc.*, **164**, A3081–A3092 (2017).
80. B. Zhou et al., *Energy*, **96**, 603–613 (2016).
81. V. W. Hu and D. T. Schwartz, *J. Electrochem. Soc.*, **169**, 030539 (2022).
82. V. Ramadesigan et al., *J. Electrochem. Soc.*, **159**, R31–R45 (2012).
83. G. Plett, *Battery Management Systems, Volume II: Equivalent-Circuit Methods*, Artech House, (2015).
84. S. Buteau and J. R. Dahn, *Journal of The Electrochemical Society*, **166**, A1611–A1622 (2019).

85. J. E. Harlow et al., *Journal of the Electrochemical Society*, **166**, A3031–A3044 (2019).
86. J. Wang et al., *Journal of Power Sources*, **196**, 3942–3948 (2011).
87. M. Naumann, F. Spingler, and A. Jossen, *Journal of Power Sources*, **451**, 227666 (2020).
88. H. M. Barkholtz, A. Fresquez, B. R. Chalamala, and S. R. Ferreira, *J. Electrochem. Soc.*, **164**, A2697–A2706 (2017).
89. V. Sulzer et al., *Joule*, **5**, 1934–1955 (2021).
90. K. A. Severson et al., *Nature Energy*, 1–31 (2019).
91. D. McIntosh, (2020) <https://data.nasa.gov/dataset/Li-ion-Battery-Aging-Datasets/uj5r-zjdb>.
92. B. I. Lab, (2020) <http://howey.eng.ox.ac.uk/data-and-code/>.
93. M. Pecht, *CALCE Battery Resesarch Group* <https://web.calce.umd.edu/batteries/data.htm>.
94. <https://www.voltaiq.com/>.
95. <https://www.astrolabe-analytics.com/>.
96. wwPDB consortium et al., *Nucleic Acids Research*, **47**, D520–D528 (2019).
97. E. S. Lander, *Nature*, **470**, 187–197 (2011).
98. J. J. de Pablo et al., *npj Comput Mater*, **5**, 41 (2019).
99. M. A. Wulder et al., *Remote Sensing of Environment*, **225**, 127–147 (2019).
100. A. Manthiram, *Nat Commun*, **11**, 1550 (2020).
101. H. Li et al., *Journal of the Electrochemical Society*, **166**, A429–A439 (2019).
102. M. Dubarry and D. Beck, *Journal of Power Sources*, **479**, 228806 (2020).
103. K. Rumpf, *Journal of Energy Storage*, 20 (2017).
104. A. Abdellahi, S. Atalay, and A. Rajan, *Journal of Power Sources*, **508**, 230246 (2021).
105. M. D. Murbach, V. W. Hu, and D. T. Schwartz, *J. Electrochem. Soc.*, **165**, A2758–A2765 (2018).
106. M. Schönleber, D. Klotz, and E. Ivers-Tiffée, *Electrochimica Acta*, **131**, 20–27 (2014).
107. J. W. Tester, E. M. Drake, M. J. Driscoll, M. W. Golay, and W. A. Peters, in *Sustainable Energy: Choosing Among Options*, MIT Press, Cambridge, MA (2012).
108. Y. A. Cengel, J. M. Cimbala, and R. H. Turner, *Fundamentals of Thermal-Fluid Sciences*, 3rd ed., McGraw Hill, (2012).
109. A. Dicks, *Fuel Cell Systems Explained*, Wiley, (2018).

110. M. L. Perry and T. F. Fuller, *Journal of The Electrochemical Society*, **149**, S59 (2002).
111. U.S. Energy Information Administration (EIA), *US EIA - Short-Term Energy Outlook*, 1–48 (2020).
112. K. Lai et al., *Journal of Power Sources*, **196**, 3204–3222 (2011).
113. B. J. Koepfel, K. Lai, and M. A. Khaleel, *ASME 2011 9th International Conference on Fuel Cell Science, Engineering and Technology. Collocated with ASME 2011 5th International Conference on Energy Sustainability, FUELCELL 2011*, 475–484 (2011).
114. A. K. S. Iyengar et al., *ASME 2019 13th International Conference on Energy Sustainability, ES 2019, collocated with the ASME 2019 Heat Transfer Summer Conference*, 1–10 (2019).
115. T. A. Adams, J. Nease, D. Tucker, and P. I. Barton, *Industrial and Engineering Chemistry Research*, **52**, 3089–3111 (2013).
116. B. J. Koepfel, (2019).
117. A. Lee et al., *Jnl Adv Manuf & Process*, **3** (2021)
<https://onlinelibrary.wiley.com/doi/10.1002/amp2.10095>.
118. W. E. Hart, J. P. Watson, and D. L. Woodruff, *Mathematical Programming Computation*, **3**, 219–260 (2011).
119. B. J. Koepfel et al., *ECS Transactions*, **78**, 2595–2605 (2017).
120. J. Bao, *MACHINE LEARNING FOR NATURAL GAS TO ELECTRIC POWER SYSTEM*, p. 1–45, (2019).
121. P. Aguiar, D. Chadwick, and L. Kershenbaum, *Chemical Engineering Science*, **57**, 1665–1677 (2002).
122. M. Lang et al., *Journal of The Electrochemical Society*, **164**, F1460–F1470 (2017).
123. W. G. Bessler, S. Gewies, and M. Vogler, *Electrochimica Acta*, **53**, 1782–1800 (2007).
124. K. P. Recknagle, R. E. Williford, L. A. Chick, D. R. Rector, and M. A. Khaleel, *Journal of Power Sources*, **113**, 109–114 (2003).

Curriculum Vitae

Erica Eggleton

Seattle WA 98125 | (406) 570-3926 | erica.eggleton@gmail.com

Education:

- Ph.D. in Chemical Engineering **January 2020 – present**
- M.S. in Chemical Engineering (Data Science Option) **September 2017 – Dec. 2019**
GPA: 3.65/4.00
University of Washington, Seattle, WA
- B.S. in Chemical Engineering **August 2013 - May 2017**
University Honors College: Honors Baccalaureate Degree
GPA: 3.83/4.00
Montana State University, Bozeman, MT

Honors and Awards:

- Best Oral Presentation - Graduate Student Symposium **September 2021**
- Torrance Foundation Policy Analysis Program **August 2020**
 - Contributed 20 hours of research and coordination efforts to a project with the Washington State Academy of Sciences
- Clean Energy Institute Student Achievement Award: Outreach & Service **May 2020**
 - For dedication and creativity in communicating STEM to a variety of audiences through volunteer work in local schools and the UW community
- Ewha-Luce International Seminar: Expanding Horizons Participant **June-July 2019**
 - Nominated and selected to participate in an 18-day intensive seminar focused on developing leadership skills, empowering women, creating international networks, and establishing a future vision for women in STEM careers. Participants included women from across the US and Asia.
 - Hosted at Ewha Womans University, Seoul, Korea
- Clean Energy Institute Fellow **September 2018 – present**
- Data Intensive Research Enabling Clean Technologies trainee **September 2018 - present**
 - A NSF research traineeship for data science
- Montana Society of Engineers Gold Award Finalist **April 2017**
 - Nominated by the MSU Chemical & Biological Engineering (C&BE) Department faculty for the award of most outstanding senior engineering student

Research Experience:

Research Assistant-Chemical Engineering Department: **January 2018 - present**

- Employer: University of Washington (UW), Seattle WA
- Studying multi-scale models and developing data analysis tools for electrochemical energy storage and conversion technologies
- Participated in NSF i-Corps program at UW to learn how to bring create a start-up based on my PhD research
- Mentored three undergraduate students
- EH&S Chemical Hygiene Officer for lab group
- Supervisor: Dr. Daniel Schwartz, University of Washington/Clean Energy Institute

Research Assistant-Chemical Engineering Department: **May 2014 – May 2017**

- Employer: Montana State University (MSU), Bozeman MT
- Worked in a lab that studies water transport within proton exchange membrane fuel cells, an important factor in making fuel cells more efficient for vehicle use
- Ran fluid-flow experiments using lab-bench scale fuel cell and analyzed results using MATLAB scripts
- Collected X-ray image data at the Canadian Light Source Synchrotron facility in Saskatoon, Canada
- Supervisor: Dr. Ryan Anderson, Montana State University

Research Experience for Undergraduates Participant (MIT): **June 2016 – August 2016**

- Employer: Center for Materials Science and Engineering/ Materials Processing Center, Massachusetts Institute of Technology (MIT), Cambridge MA
- Conducted NSF funded research on fabrication methods for lithium ion battery cathodes and material properties of $\text{Li}_2\text{S}-\text{P}_2\text{S}_5$ Li-Ion conducting solid electrolyte to make safer, longer-lasting batteries
- Supervisor: Dr. Krystyn J. Van Vliet, Massachusetts Institute of Technology

Research Experience for Undergraduates Participant (ISU/UVA): **May 2015 – August 2015**

- Employer: Center for Biorenewable Chemicals (CBiRC), Iowa State University (ISU), Ames IA
- Conducted NSF funded research on the oxidation of butanol over Pt/C catalysts to determine the effects of reaction products on kinetics, leading to a better understanding of reactions for bio-plastic production
- Supervisor: Dr. Robert Davis, University of Virginia (UVA)

Teaching Experience

Teaching Assistant

- CHEME 330 - Chemical Engineering Fluid Mechanics (1 quarter)
- CHEME 498 – Quantum Mechanics for Chemical Engineers (2 quarters)
 - Held in person office hours to go over important concepts and help with class assignments
 - Taught in-class transport COMSOL tutorial and homework review sessions
 - Graded assignments and created detailed solutions documents

Electrochemical Society (ECS) Hack Week Instructor

- Part of the Electrochemical Society Spring Meeting, Dallas, TX (May 2019)
- Created and led an introductory tutorial for the Python package, Pandas, for ECS Hack Week participants of various skill levels.

Professional Organizations and Service:

- Electrochemical Society (ECS) **August 2016 - present**
 - **2018 – 2020:** UW student chapter **outreach chair**
 - Organize and attend outreach activities including: presenting scientific demos at local STEM fairs, inviting guest speakers with electrochemistry backgrounds to give seminars, and giving lessons to K-12 classes
 - **2016 – 2017: President** of MSU student chapter
- UW Women in Chemical Engineering (WChE) **September 2017 - present**
 - **2020-2022: media director** (website and social media)
 - Active member of group dedicated to educating, empowering, and advocating for women in chemical engineering
 - Participate in group-sponsored outreach activities including: presenting a demo at the “Introduce a Girl to Nano” event; leading a workshop at the Expanding Your Horizons Conference, an event for young girls interested in STEM, and volunteering for the 2nd and 3rd annual WChE Industry Panel.
- Graduate and Professional Student Senate (GPSS) **September 2018 - present**
 - **2018 – 2022:** University Transportation Committee graduate student liaison
 - **2019 – 2021:** Chemical Engineering Department **senator**
 - **2020 – 2021:** GPSS Judicial Committee
 - **2018 – 2020:** Science and Policy Committee
 - White Paper Workshop planning committee
 - Assisted in the creation of the CEI/Earth Lab/GPSS Science Policy Analyst in Residence Program
- Journal of Open-Source Software (JOSS) Reviewer **December 2020 - present**
 - Reviewed three python packages and corresponding articles
- Unite Nations Youth Hackathon **Sept 2021 – Dec 2021**
 - Helped plan programming and logistics for hackathon
 - Found datasets that matched hackathon theme: effects of COVID-19 on Sustainable Development Goals
- Model COP26 **April 2021**
 - Participated in a model COP26, organized by the Atlantic Council, British Embassy, and University of Kansas, as a negotiator for Poland.
- Clean Energy Ambassador Volunteer **Sept. 2017 – Jan 2020**
 - **2017 – 2020:** Volunteer with the Clean Energy Institute (CEI) for local outreach events.
 - Presented demos and presentations to K-12 students at local schools, libraries, and science fairs.
- Association of Chemical Engineering Graduate Students (ACES) **October 2018 - Sept. 2019**
 - **2019: Co-Chair** of the planning committee for the Graduate Student Symposium, a professional development event consisting of student research talks, student poster presentations, and invited guest speakers that apply a chemical engineering degree to various fields

Publications:

Battrell, L., Trunkle, A., **Eggleton, E.**, Zhang, L., & Anderson, R. Quantifying Cathode Water Transport via Anode Relative Humidity Measurements in a Polymer Electrolyte Membrane Fuel Cell. *Energies* **2017**, 10, 1222

McGrogan, F. P., Swamy, T., Bishop, S. R., **Eggleton, E.**, Porz, L., Chen, X., Chiang, Y., Van Vliet, K. J., Compliant yet Brittle Mechanical Behavior of $\text{Li}_2\text{S-P}_2\text{S}_5$ Lithium-ion Conducting Solid Electrolyte. *Advanced Energy Materials* **2017**, 7, 1602011

Anderson, R., **Eggleton, E.**, and Zhang L., Development of two-phase flow regime specific pressure drop models for proton exchange membrane fuel cells. *International Journal of Hydrogen Energy* **2015**, 40, 1173.

Presentations:

Eggleton, E., Schwartz, D. T., Route-Specific Energy Requirements for Battery-Electric Buses, an Open-Software, Physics-Based Approach. In: *Electrochemical Society Spring Meeting*. Vancouver, BC. June 2, 2022.

Eggleton, E., Schwartz, D. T., Route-Specific Energy Requirements for Battery-Electric Buses, an Open-Software, Physics-Based Approach. In: *UW Chemical Engineering Graduate Student Symposium*. Seattle, WA. September 23, 2021.

Eggleton, E., Schwartz, D. T., route_dynamics: An Open-Source Python Package for Estimating Electrified Vehicle Load. In: *Electrochemical Society Fall Meeting*. Atlanta, GA. October 14, 2019.

Eggleton, E., Schwartz, D. T., Incorporating GIS Data into a Battery Maintenance Model for Electrified Buses. In: *Ewha-Luce International Seminar Science Talk Concert*. Seoul, Korea. July 4, 2019.

Eggleton, E., Schwartz, D. T., Incorporating GIS Data into a Battery Performance Model for Electric and Hybrid-Electric Buses. In: *Electrochemical Society Spring Meeting*. Dallas, TX. May 30, 2019.

Eggleton, E., Schwartz, D. T., Incorporating GIS Data into a Predictive Maintenance Model for Hybrid-Electric Buses. In: *Orcas International Conference on Energy Conversion & Storage*. Friday Harbor, WA. September 6, 2018.

Eggleton, E., Battrell, L., English, M., Anderson, R., Diffusion Layer Saturation Analysis of PEM Fuel Cells. In: *National Conference on Undergraduate Research (NCUR)*. Memphis, TN. April 6, 2017.

Eggleton, E., McGrogan, F. P., Van Vliet, K. J. Cathode Fabrication Methods for $\text{Li}_x\text{Mn}_2\text{O}_4$ and Its Doped Derivatives. In: *CMSE/MPC Summer Research Internship Program Poster Session*. Cambridge, MA. August 4, 2016.

Eggleton, E., Battrell, L., Anderson, R. PEM Fuel Cell Water Saturation Modeling and Imaging. In: *Montana State University Student Research Celebration*. Bozeman, MT. April 15, 2016.